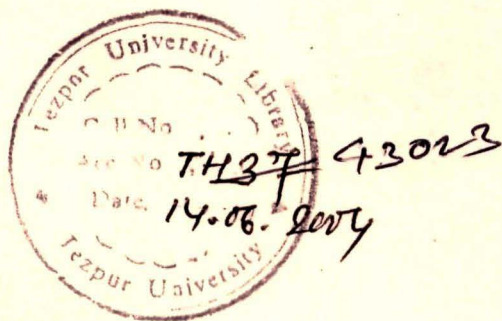


TH 37 43023



CENTRAL LIBRARY
TEZPUR UNIVERSIT

Accession No. T 41

Date _____

REFERENCE BOOK
NOT TO BE ISSUED
TEZPUR UNIVERSITY LIBRARY

**SYNTHESIS OF SEMICONDUCTOR QUANTUM
DOTS ON POLYMER MATRIX AND APPLICATION IN
NONLINEAR OPTICS / ELECTRONICS**

A THESIS SUBMITTED TO

TEZPUR UNIVERSITY

IN FULFILLMENT OF THE REQUIREMENTS
FOR THE DEGREE OF

DOCTOR OF PHILOSOPHY

TH 37

BY

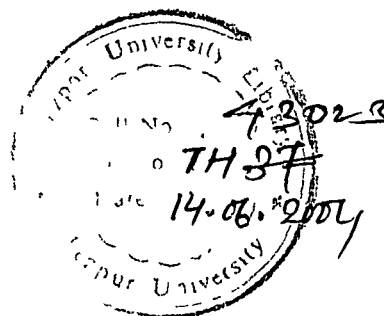
DAMBARUDHAR MOHANTA

DEPARTMENT OF PHYSICS,
SCHOOL OF SCIENCE AND TECHNOLOGY

TEZPUR UNIVERSITY
NAPAAM, TEZPUR-784 028

ASSAM, INDIA.

MARCH, 2003



Dedicated to
The Almighty & my beloved parents

DECLARATION

I hereby declare that the thesis entitled "**Synthesis of semiconductor quantum dots on polymer matrix and application in nonlinear optics / electronics**" being submitted to the Department of Physics, Tezpur University, Tezpur, Assam in fulfillment of the requirements for the award of the degree of Doctor of Philosophy, has previously not formed the basis for the award of any degree, diploma, associateship, fellowship or any other similar title or recognition.



The Holi day of March 18, 2003

(***Dambarudhar Mohanta***)

Department of Physics,
Tezpur University,
Tezpur-784 028 (Assam).

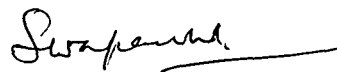
CERTIFICATE

This is to certify that the thesis entitled "**Synthesis of semiconductor quantum dots on polymer matrix and application in electronics / nonlinear optics**" being submitted by **Dambarudhar Mohanta** to Tezpur University, Tezpur, Assam in fulfillment of the requirements for the award of the degree of Doctor of Philosophy, is a record of original bonafide research work carried out by him. He has worked under our joint guidance and supervision and has fulfilled the requirements for the submission of this thesis. The results contained in the thesis have not been submitted in part or full to any other university or institute for award of any degree or diploma.



(Amarjyoti Choudhury)

Professor,
Department of Physics,
Tezpur University,
Assam-784 028



(Swapan Ku. Dolui)

Professor,
Department of Chem.Sc.,
Tezpur University,
Assam-784 028

ACKNOWLEDGEMENTS

It is a matter of immense pleasure and fortune for me to express deep sense of gratitude to Prof. A. Choudhury for his dynamic guidance, constant encouragement, meticulous supervision and moral support that I have received all through my research work. His valuable suggestions and lively discussions were inspiring enough to put my best efforts into my work. Needless to say, I shall be highly obliged to him for all the time.

I am highly grateful to Prof. S. K. Dolui for his keen interest and inspiring supervision for synthesizing and characterizing the samples. His constructive comments, immense help and assistance at every stage of my work shall remain noteworthy.

I extend my sincere and hearty gratitude to Prof. N. C. Mishra who has initiated my research career in due course of time. His personal involvement, timely help, stimulating discussions to carry out irradiation experiments put myself into the depth of the research, for which I shall always remain grateful to him.

I am extremely grateful to the Pelletron as well as Materials Science group of Nuclear Science Centre (NSC), New Delhi for lending their support and sincere help for doing irradiation experiments.

I would like to take this opportunity to thank Indian Space Research Organization (ISRO) for assistance and associating me with the "Quantum dot project" in the department.

I would like to thank USIC, Guwahati; USIC, Jadavpur University; RSIC and Physics Department, NEHU, Shillong; Chemistry Department, GU, Guwahati; Physics Department, CU, Hyderabad and Department of Chemical Sciences, Department of MBBT, Department of Electronics, TU, Tezpur for cooperation and concerns to characterize the samples on various aspects.

I extend sincere appreciation to my colleagues and seniors Dr G A Ahmed, Dr K Baruah, Dr N Karak, Dr D Nath, Dr N Das, Dr N S Bhattacharyya, Dr J K Sarma and Dr A Kumar for willing support suggestions and help.

I thank Mr S S Nath, Mr D Saikia, Mr P Choudhury, Mr D Gohain Ms S Choudhury and Mr A Bordoloi for help and assistance.

My special thanks are due to Prof. George Stanciu of Universitat "Polytechnitat" of Bucharest, Romania who took special interest in providing AFM images. Thanks to Adelaide Convention Centre, Australia for Syncroscopy.

I am indebted to my parents Mr R K Mohanta and Mrs P Mohanta for their continuous encouragement, moral support and good will.

Last but not least, I thank multimillion times to the Almighty for his subtle guidance, inspiration and eternal love & blessings.

Dambarudhar Mohanta

PREFACE

This thesis is a description of a number of experiments in the young field of *low dimensional semiconductors* in general and *semiconductor quantum dots* in particular. Quantum dots are small conductive regions in space of a few nanometer dimensions that contain a tunable number of electrons. They are often named as '*artificial atoms*', because the electrons are confined to an artificially made puddle, in much the same way as electrons are confined to the region around the nucleus of an atom. Again, although the shape of the confinement potential in artificial atoms is different from that of the atoms they display much of the same physics.

This thesis is a result of my investigations related to embedding semiconductor quantum dots on polymer matrix, optical absorption, surface optic phonon modes, luminescence, 100 MeV chlorine ion induced modified characteristics and possible application in nonlinear optics and electronics.

The thesis is broadly divided into seven chapters, each of which again split into sub-sections. The very first chapter is introductory in nature and it discusses background of low dimensional systems (3D to 0D), density of states, energy level alongwith fabrication methods etc. Chapter-2 includes fabrication details and outlines proof of quantum dot formation interms of size determination by XRD, SEM, TEM etc. followed by theoretical illustrations. Chapter-3 deals with thermo luminescence study of surface states alongwith fluorescence emission and exciton absorptions. Study of phonons in nanoparticle systems is highlighted in chapter-4. The vibrational features include characteristic longitudinal optic (LO) and surface optic (SO) modes and are discussed through analysis of resonant Raman spectra for CdS quantum dots in different dielectric media. Swift heavy ion irradiation experiment and ion induced modified properties of quantum dots are explained in chapter-5. Physical

phenomena that encourage possible applications in relevant areas like nonlinear optics and electronics are elaborated in chapter-6. The same chapter describes presence of significant amount of third order nonlinearity in CdS/PVOH quantum dots. Moreover, photon induced single electron effect in quasi-arrayed ZnS/PVOH quantum dot system is illustrated in the said chapter. Conclusions and future directions are highlighted in chapter-7.

Dambarudhar Mohanta

CONTENTS

DECLARATION	iii
CERTIFICATE	iv
ACKNOWLEDGEMENT	v
PREFACE	vii

CHAPTER-1

INTRODUCTION

Page No.

1.1	Low dimensional quantum structures	2
1.2	Energy levels and density of states	5
1.3	Quantum dots : quasi-zero dimensional structures	9
1.4	Quantum confinement regimes	11
	1.4.1 Exciton formation	11
	1.4.2 Exciton confinement regime	12
	1.4.3 Individual particle confinement regime	13
	1.4.4 Blue-shift and size quantization	15
	1.4.5 Theoretical support	18
1.5	Fabrication techniques	23
	1.5.1 Chemical routes	23
1.6	Objectives of the present study	25

CHAPTER-2

FABRICATION AND SIZE CONTROL OF II-VI SEMICONDUCTOR QUANTUM DOTS

2.1	Properties of used polymer matrices	28
2.2	Experimental details	32
2.3	Principles of size determination	36
	2.3.1 X-ray diffraction method	36
	2.3.2 Theoretical models based on blue shift	40
	2.3.3 Size confirmation through electron microscopy	44

CHAPTER-3

CARRIER TRAPPING MECHANISM AND THE ROLE OF SURFACE STATES

3.1	Thermoluminescence study of surface states	47
3.2	Optically stimulated luminescence phenomena	56
3.3	Excitonic absorption and surface states	58
3.4	Fluorescence emission of quantum dots	64

CHAPTER-4

VIBRATIONAL FEATURES OF EMBEDDED QUANTUM DOTS

4.1	Electron-phonon coupling	70
4.2	Raman spectroscopy and surface optic phonons	75
4.3	Macroscopic model of surface phonons	82

CHAPTER-5

ION IRRADIATION EXPERIMENT AND MODIFIED BEHAVIOUR OF EMBEDDED QUANTUM DOTS

5.1	Ion-matter Interaction	93
5.2	Our quantum dot systems	94
5.3	The irradiation experiment	96
5.3.1	Ion induced effect of hydroxyl-free ZnO quantum dots	98
5.3.2	Grain growth and grain fragmentation effects	105
5.3.3	Irradiation induced surface emission enhancement in ZnS:Mn quantum dot system	118

CHAPTER-6

APPLICATIONS IN NONLINEAR OPTICS / ELECTRONICS

6.1	Third order nonlinearity in the fluorescence activation of ion irradiated CdS/PVOH quantum dots	128
6.2	Nonlinear optical phenomena and third order susceptibility of quantum dots	136
6.2.1	Non-resonant transmission response of CdS quantum dots	142
6.2.2	Non-resonant non-degenerate four wave mixing phenomena of CdS/PVOH quantum dots	146
6.3	Frequency dependent current density and capacitance response of CdS/PVOH quantum dots	151
6.3.1	Current-Voltage ($I-V$) characteristics	152
6.3.2	Capacitance-Voltage ($C-V$) analysis	156
6.4	Photon induced electron transport in quasi-arrayed ZnS quantum dots	161
6.4.1	Test bed to observe single electron effects	161
6.4.2	Photocurrent generation due to carrier transport	163

CHAPTER-7

CONCLUSION AND FUTURE DIRECTIONS 170

APPENDIX

REFERENCES

PUBLICATIONS

ADDENDA

CHAPTER-1

INTRODUCTION

CHAPTER-1

INTRODUCTION

According to Eric K. Drexler [1] *"In spite of large predictions about future technology, it is certain that what we can do depends on what we can build. We could manufacture assembly of machines much smaller than living cells and make materials stronger and lighter than available today. Hence, better space craft, tiny devices that can travel along capillaries to enter and repair living cells and the ability to heal disease, reverse the ravages of age, or make our bodies speedier or stronger than ever before. And we could make machines down to the size of viruses that would work at speeds which none of us can yet appreciate. Once we learned how to do it, it would have the option of assembling these myriads of tiny parts into intelligent machines, perhaps based on the use of trillions of nanoscopic parallel processing devices which make descriptions, compare them to recorded patterns and then exploit the memories of previous experiments. The very often applicability of the words like nanode, nanograph, nanoscopy, nanosurgery will be the issues of nanoscience and technology which are not far reaching as far as theory and experiment is concerned*

1.1 Low dimensional quantum structures

In crystalline solids, where atoms form a regular lattice, certain number of electrons can move as if in free space. When the number of free electrons is zero, the material becomes an insulator for electrical current conduction as in case of quartz. In metals, e.g. Cu each atom contributes one or two free electrons. So, a metal cube of 100 nm will contain about a 1000 million free electrons. The presence of extremely large number of electrons in a metal, very often, require classical treatments to describe electron motion (electrons move and bounce like rigid balls). In contrast to metals and insulators, semiconductor materials have a small number of free electrons which can be varied by means of doping of suitable impurity etc. which typically varies from 0 to 1000 in a cube of 100 nm. The small number of electrons in the tiny structure makes it much easier to observe quantum mechanical behaviour and therefore, while discussing low dimensional structures we shall confine our attention to semiconductor nanostructures only.

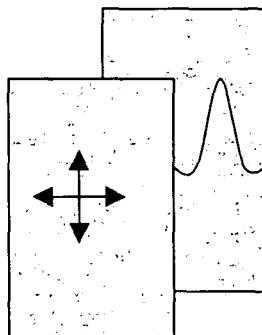
Low dimensional / Quantum / Nanostructures represent a state of matter in the transition region between bulk solids and molecular structures [2-9]. Consequently, nanoparticles have chemical and physical properties different from those of the bulk and isolated atoms or molecules with the same chemical composition. The properties gradually change from molecular to solidstate behaviour with increasing particle size. The quantum structures exhibit unique size dependent electronic, magnetic,

optical and catalytic properties due to extremely large surface-to-volume ratio ($s/v > 1$) [10-17]. Their potential applications are expected in the areas namely; microelectronics, electrooptics, nonlinear optics, catalysis, photography and electrochemistry.

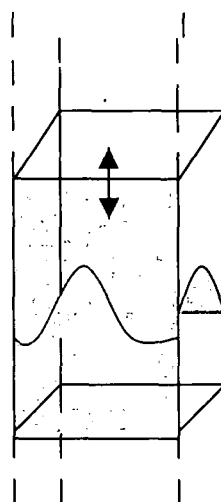
To understand quantum confinement effect in these systems, let us have a glance into various types of quantum systems and their physical basis to define the nature of electron motion within them.

As shown in figure-1, the free electrons in these solids behave as waves with a wavelength depending on the density of free electrons in the solid. A smaller density of electrons yields a longer wavelength, which in semiconductors can greatly exceed the interatomic distances. The electron wave nature becomes important when its wavelength (λ) is comparable to the size of the host solid. When the electron wavelength is comparable to the thickness of the material it is the case of 1-dimensional confinement, which results into 2D-slice/quantum well structure. In other words, electron movement has been restricted in a specific direction (here along thickness) and electron movement is allowed only in two other perpendicular directions (length and breadth). So, essentially, the electrons live in a 2D world where they have to obey specific rules. These rules can lead to phenomena which have no analogue to day to day 3D-bulk world [18]. In the 1D-pillar or quantum wire, electrons can move only in one direction (along length) and there is no motion in the other two confined directions (breadth and thickness). Complete confinement is

2D Quantum Well



1D Quantum Wire



0D Quantum Dot

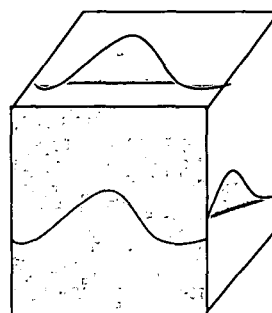


Figure 1. Carrier confinement in low dimensional systems

reached in the zero dimensional quantum boxes, where the electron's wavelength is comparable to the three sides of the box. Such a reduced dimensional box is termed as a *quantum dot*. The physical rules belonging to the dimensionality of a system yield distinct electronic behaviour. The experimental observations resulting from reduced dimensionality have been one of the major subjects of low dimensional physics.

1.2 Energy levels and density of states

In order to understand splitting of energy levels and density of states of reduced dimensional structures, first consider the case of a heterostructure made of narrow band gap and wide band gap materials.

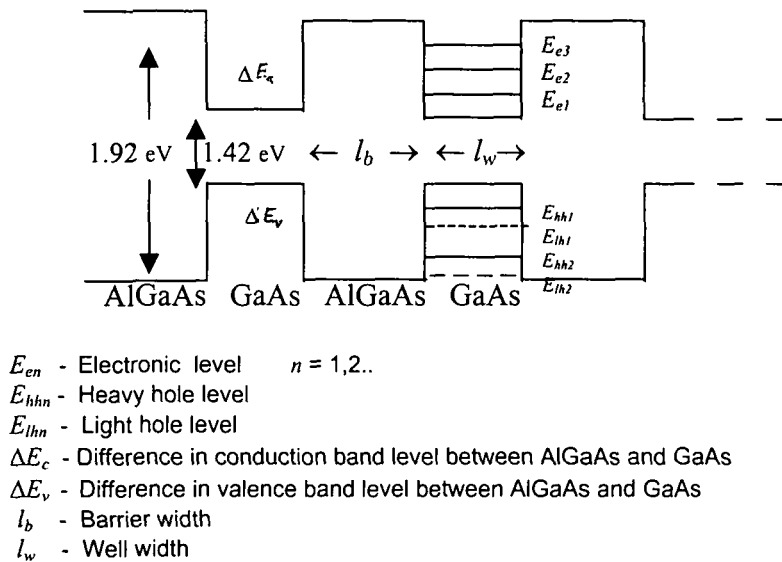


Figure 2. Example of a multiple quantum well (MQW) / heterostructure

Figure-2 represents schematic energy diagram of an AlGaAs / GaAs quantum well heterostructure. Because, the energy gap of AlGaAs (~ 1.92 eV) is larger than that of GaAs (~ 1.42 eV), there is an energy offset in the conduction band E_c at the interfaces between the two materials. Therefore, in the thin layer, carrier motion perpendicular to the layer is restricted and the kinetic energy is quantized into discrete energy levels. Structures consisting of such extremely thin layers having quantized energy levels are called *Quantum well* structures. The thin layer is called a potential well, and one of the neighbouring layers with wide band gap energy is called a potential barrier. Usually, the well thickness is < 10 nm. A structure with one well, is called as a *single quantum well* (SQW) structure and one with several wells is called a *multi quantum well* (MQW) structure [19]. It follows from quantum mechanics [20] that the bound states exist in the quantum well and let the corresponding lowest energy level be denoted by E_{nx} . The propagation of the electron is still possible in the remaining two (y- and z-) directions and therefore, the energy E_x represents the bottom of a two dimensional conduction (sub-) band characterized by Bloch vectors k_y & k_z . Depending upon the width and depth of the quantum well, several bound levels may exist, corresponding to a number of 2D-subbands. In the same fashion, the energy levels in a quantum wire form 1D-subbands with Bloch vector k_z .

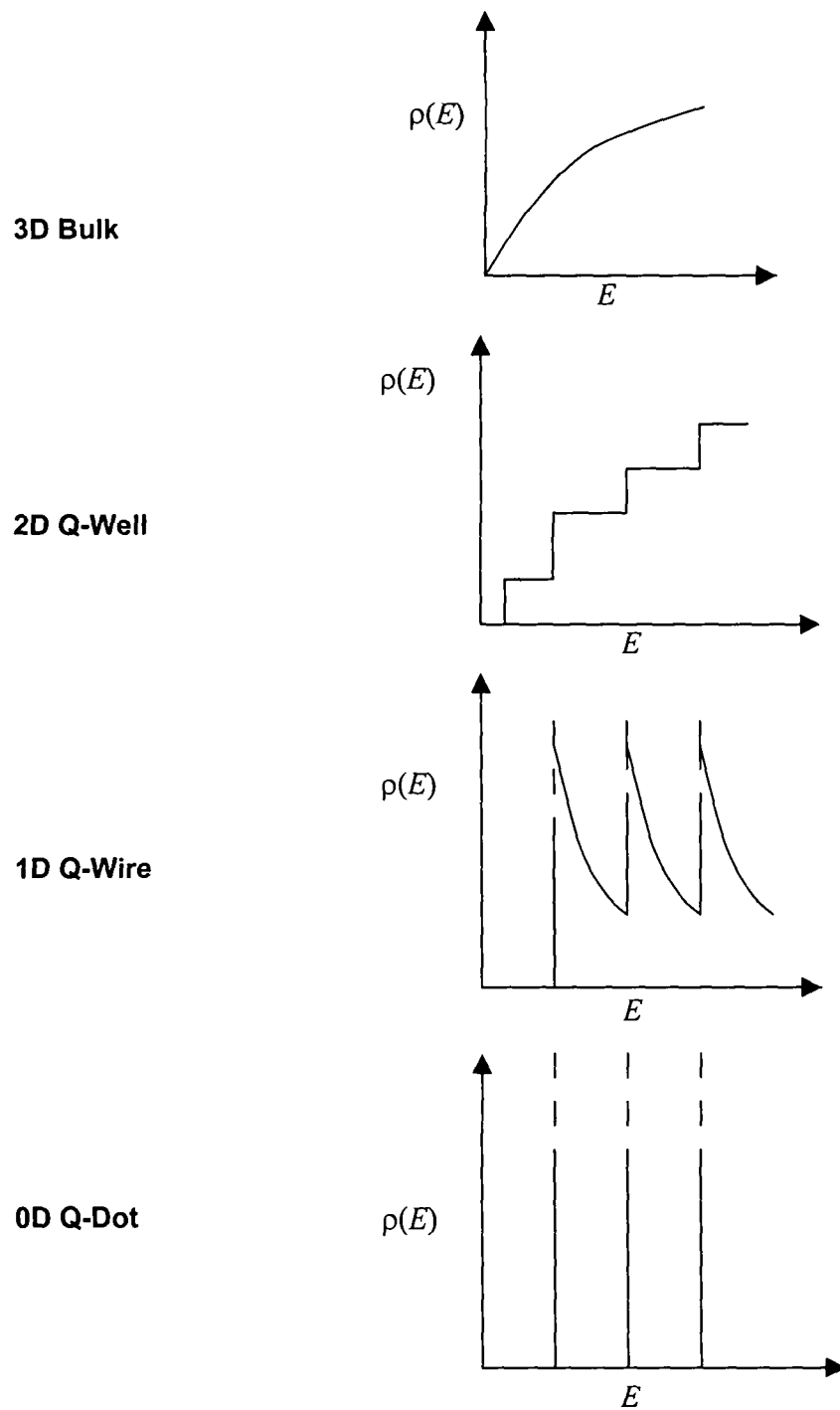


Figure 3. Density of states of 3D-bulk and reduced dimensional systems

The electrical, optical and magnetic properties of the quantum structures are greatly modified with respect to the bulk material. The density of states generally becomes sharper with decreasing dimensionality (figure-3) and hence the optical and electrooptical properties are supposed to be altered. The dimensionality of the single electron states is determined by a length scale of an electron wave function (λ). The dimensionality in the density of states (DOS), which is defined as the number of occupied states per unit energy spectrum of the Bloch electrons is one of the familiar properties. The number of the quantum states of an electron whose energy lies between E and $E + dE$ is given as $\rho^{(d)}(E) dE$ per unit volume in d -dimension, where ρ is the density of states. The DOS in a dD ($d = 0,1,2,3$) crystal can be represented explicitly by the following expressions [20,21]:

$$\text{3D-Bulk: } \rho^{(3)}(E) = \frac{1}{2\pi^2} \left(\frac{2m^*}{\hbar^2} \right)^{3/2} E^{1/2} \quad (1)$$

$$\text{2D-Quantum well: } \rho^{(2)}(E) = \frac{m^*}{\pi\hbar^2} \sum_{n_z} \Theta(E - E_{n_z}) \quad (2)$$

$$\text{1D-Quantum wire: } \rho^{(1)}(E) = \frac{1}{\pi} \left(\frac{2m^*}{\hbar^2} \right)^{1/2} \sum_{n_y} \sum_{n_z} \Theta(E - E_{n_y} - E_{n_z})^{1/2} \quad (3)$$

$$\text{0D-Quantum dot: } \rho^{(0)}(E) = 2 \sum_{n_x} \sum_{n_y} \sum_{n_z} \delta(E - E_{n_x} - E_{n_y} - E_{n_z}) \quad (4)$$

where m^* is the effective mass of the band and the parabolic approximation is used. Here $\Theta(x)$ is the Heaviside step function and E_{n_i} ($i = x, y, z$) is an energy of the sublevel along the i^{th} confinement direction labeled by the quantum number $n_i = 1, 2, 3, \dots$

Referring to figure-3, one finds that the DOS in 3D crystals increases by $E^{1/2}$ as a function of the energy E . In the 2D case, step like DOS appears. The DOS diverges at the band edge energy ($E = E_{n_x} + E_{n_z}$) in the 1D case, and decreases in proportion with $E^{-1/2}$. However, in the 0D case, the spectrum is completely discrete and the density of states becomes a series of delta peaks. Moreover, it is important to state that the DOS remains finite at the bottom of the 2D Q-Well, whereas it tends towards zero in the 3D system. More drastically, it diverges to infinity at the bottom of the 1D level. Now onwards, we shall restrict our attention to explore novel and inherent properties exhibited by 0D quantum dot structures.

1.3 Quantum dots : quasi-zero dimensional structures

Quantum dots are small conductive regions in a semiconductor, containing a variable number of electrons ($N = 1$ to 1000) that occupy well defined discrete quantum states. They are often referred to as artificial atoms [22] with unique property that they can be connected to current and

voltage contacts. This allows one to use transport measurements to probe the discrete energy spectra. In fact, quantum dots are recognised as *artificial atoms* because they are man made "droplets" of charge that can contain anything from a single electron to a collection of several thousand [23]. The dimensions typically range from nm to a few μm , and their size, shape and interactions can be precisely controlled through the use of advanced nano-fabrication technology.

To continue the analogy with the artificial atoms, two quantum dots can be connected to form an "*artificial molecule*". Depending on the strength of the interdot coupling, the two dots can have an ionic bonding [24-29] (i.e., electrons are localized on the individual dots) or a covalent bonding (i.e., electrons are delocalized over both the dots). The covalent bonding leads to a bonding and anti-bonding state with an energy splitting proportional to the tunnel coupling. The physics of quantum dots shows many parallels with the behaviour of naturally occurring quantum systems in atomic and nuclear physics. As in case of an atom, the energy levels in a quantum dot becomes quantized due to the confinement of the electrons. Thus, with quantum dots, an experimentalist can substantially perform atomic experiments by scanning through the entire periodic table by simply changing a bias voltage [23].

1.4 Quantum confinement regimes

The carriers are supposed to be confined when the material system approaches de-Broglie wavelength. We shall first outline the exciton formation and then we shall directly proceed to the nature of confinement in semiconductor quantum dots.

1.4.1 Exciton formation

An electron-hole (e^-h^+) pair is produced when a photon of energy comparable or more than the energy gap E_g is absorbed in a semiconducting crystal. The electron and hole produced in this way are free and can move independently through the crystal. But it is the attractive coulombic interaction which results stable bound states of the two particles which behaves now as a single entity. It moves through the crystal transporting energy but not charge. The bound electron-hole pair in a crystal is termed as an *exciton*, which is analogous to the electron and proton of a H-atom. So, an *exciton* is a quantum of electronic excitation produced in a periodic structure such as an insulating or semiconducting solid. Frenkel type exciton is small and tightly bound where as Mott-Wannier exciton is weakly bound with the electron-hole separation large in comparison with the lattice constant. In our quantum dot / nanoparticle descriptions, by exciton we shall confine our attention to Wannier excitons only. Schematic representation in a spherical quantum particle is shown in figure-4. In very fine particle systems [30], there are two limiting

situations according to the ratio of the characteristic length R representing the system size to the effective Bohr radius $a_B^{(3)}$ of the exciton in the bulk material [31]. According to the numerical calculations, cross over between the two regimes occur around $2 < R / a_B^{(3)} < 4$ [31, 32].

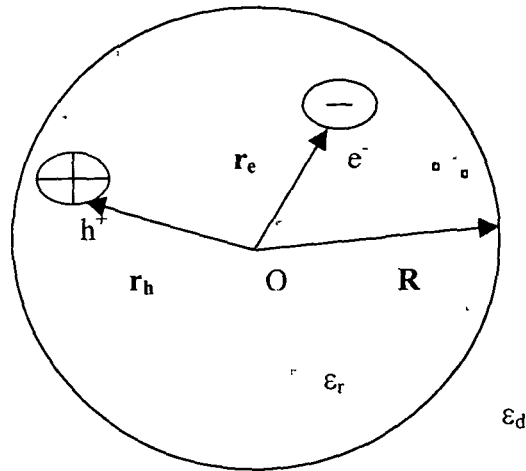


Figure 4 Exciton formation in a spherical quantum dot having dielectric constant ϵ_r embedded in a matrix of dielectric constant ϵ_d

1.4.2 Exciton confinement regime: $R/a_B^{(3)} \gg 1$

This is a case of weak confinement regime. In this regime, the character of the exciton as a quasiparticle is conserved and the relative motion of the exciton is less restricted by the boundary condition. On the other hand, the center-of-mass motion suffers from the quantum confinement and its kinetic energy increases only slightly. Taking into

account the spatial extent of the e^-h^+ relative motion, total energy of the lowest excitonic state is given by

$$E_{tot}^{(0)} \sim -E_{Ry}^* + \frac{\pi^2}{2(m_e^* + m_h^*)[R - \eta(\sigma)a_B^{(3)}]^2} \quad (5)$$

where $\sigma = m_h^* / m_e^*$ and $\eta(\sigma) \sim 1$ is an increasing function of σ of order of unity. The term $\eta(\sigma) a_B^{(3)}$ corresponds to the dead layer: The center-of-mass of the exciton cannot reach the surface because it requires a strong deformation in the e^-h^+ relative motion. If the exciton Bohr radius is sufficiently small (e.g. Frankel exciton), this dead layer correction is unnecessary.

1.4.3 Individual particle confinement regime: $R / a_B^{(3)} \ll 1$

This is a situation of strong quantum confinement. In this limit, an electron and a hole occupy primarily an individual lowest eigen state in a confinement potential with relatively little spatial correlation. The wave function of the e^-h^+ relative motion may be squeezed due to the strong confinement. Because the kinetic energy of each particle becomes very large in comparison with the coulomb energy, no bound state (exciton) is formed. An asymptotic wave function of the ground state in a sphere structure is given by

$$\Psi^{(0)}(\vec{r}_e, \vec{r}_h) \sim N^{(0)} \left(1 - \alpha \left| \vec{r}_e - \vec{r}_h \right| \right) j_0 \left(\frac{\pi r_e}{R} \right) j_0 \left(\frac{\pi r_h}{R} \right) \quad (6)$$

where $N^{(0)}$ being the normalisation constant, $j_0(x)$ is a spherical Bessel function of the zeroth order and $\alpha = 0.498 / a^{(3)}$. Its total energy is given by

$$E_{tot}^{(0)} \sim \frac{1}{2\mu} \left(\frac{\pi^2}{R^2} \right) - 1.786 \left(\frac{e^2}{\epsilon R} \right) - 0.248 E_{Ry}^* \quad (7)$$

where first, second and third terms on the right hand side representing contribution arising from quantum confinement, coulomb interaction and the remnant of the exciton effect. In the exciton confinement regime there are two types of excited states of the exciton. In the first type of excited states, the $e-h$ relative motion is in the 1s (lowest) state and the center-of-mass motion is excited (characterized by a quantum number N) in a confinement potential. In the other, the e^-h^+ relative motion is excited to the 2s, 3s...states. In the $d = 0$ spherical systems with a finite size, all the s-like states is one photon allowed in principle because of the breakdown of the translational invariance. For example, the 1s exciton with the N^{th} excited state of the center-of-mass motion has the oscillator strength per unit volume as

$$f_{1s;N}^{(0)} = f_{1s}^{(3)} \left[1 - \eta(r) \frac{a_B^{(3)}}{R} \right] \left(\frac{\sigma}{\pi^2 N^2} \right) \quad (8)$$

where $N = 1,2,3...&$ $f_{1s}^{(3)}$ is the oscillator strength per unit volume of the 1s exciton in bulk material [31]. In the individual particle confinement regime an electron (a hole) forms sub-bands in all the confinement directions. Then, the one photon absorption (OPA) spectra would consist of discrete

lines, each corresponding to a pair of sub-bands which satisfy the selection rules: $\alpha_i - \beta_i \equiv \text{even} \approx 0$ with x, y, z in a cubic geometry.

1.4.4 Blue-shift and size quantization

When the size of a crystallite decreases, band gap increases appreciably followed by discretization of the energy levels (figure-5). In other words, a nanosized crystallite or a quantum dot is believed to absorb light at relatively smaller wavelength with respect to bulk. The feature is well observable in UV-visible optical absorption spectra (figure-5).

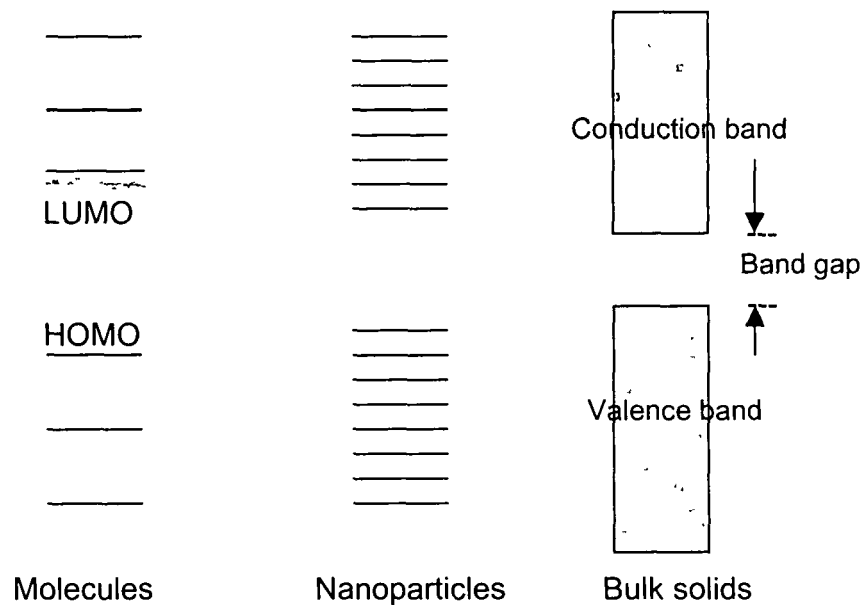


Figure 5. Evolution of energy levels: Macro to nanosystem

The increment in band gap energy is known as blue-shift energy. And so, quantization of the center-of-mass motion leads to a small increment (*blue shift*) in the exciton's total energy (first term on the RHS of equation-7). For the smallest possible dots, the wavelength shift towards blue, is about ~ 200 nm (1eV) [33, 34].

The nature of size quantization can be probed through interpretation of the optical absorption spectra (OAS). For a bulk semiconductor, at absolute zero one has continuous valence and conduction band with an energy spacing in between top of the valence band and bottom of the conduction band. With size reduction, two effects simultaneously occur for a low dimensional structure. First, band gap increases significantly and then continuous energy bands gradually turn into discrete levels (figure-5). Therefore, for a smallest possible dot one obtains largest band gap energy and maximum spacing between the discrete energy levels. From the absorption spectra one can correlate the amount of blue shift with quantum dot size distribution. They are :

- 1) Stronger the blue shift with respect to bulk, stronger is the quantum confinement as quantum dots of variable size absorb photons of variable energies.
- 2) Long tailing in the optical absorption spectra represents large inhomogeneity in the quantum dot size distribution.

3) Existence of sharp peaks in the OAS represents exciton absorption (at respective wavelength) which corresponds to the transition between lowest 1s-1s electronic states. Higher transition states are rarely observable and may be expected in the ultra pure samples.

The quantum size effects or discretization of electron energy levels are revealed in these structures when their size approaches that of the bulk exciton diameter. So, in addition to surface properties ($s/v > 1$), electronic effect needs to be considered. The band structure of the bulk solids gradually develops with increasing particle size i.e. molecular

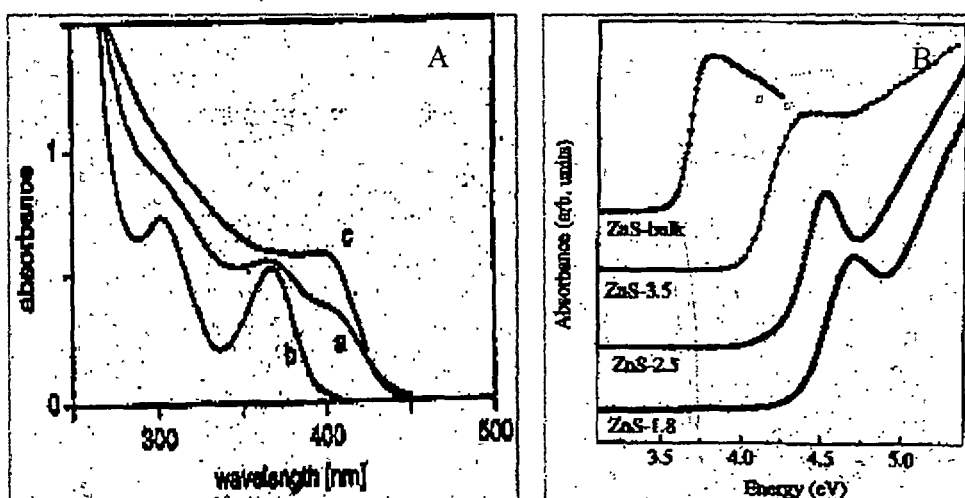


Figure 6. A- Optical absorption spectra of CdS quantum dots recorded during a size selective precipitation. Spectrum of (a) the cluster mixture, (b) the supernatant solution and (c) the redissolved precipitate; B- Size quantization OAS of ZnS quantum dots with respect to bulk

orbitals convert into delocalized band states. This transition could be impressively observed in the OAS of semiconductor nanoparticles. Sharp and discrete molecular excitonic absorption bands of the ultra small particles gradually convert into the typical unstructured edge like absorption with increasing particle size alongwith shifting of the onset of the absorption from the short wavelengths toward the bulk edge [35]. In this aspect, many exciting experiments have been performed on this novel state of matter with usable material properties in such diverse fields as luminescence, nonlinear optics, catalysis, electronics and solar energy conversion. Figure-6(A) represents OAS of CdS quantum dot samples prepared by size selective precipitation [36,37], whereas figure-6(B) depicts that of ZnS quantum dots (with wavelength-energy conversion) [34].

1.4.5 Theoretical support

The Mott-Wannier exciton is a weakly bound $e^- - h^+$ pair created by photons coupled to a material (figure-4). It can be represented in a simple hydrogen like picture, it has energy levels E_n proportional to n^{-2} ($n = 1, 2, 3, \dots$). The corresponding Bohr orbitals have the radii $R^{(n)}$ in units of nm given by

$$R^{(n)} = 0.5 \frac{\epsilon_r}{m^*} n^2 \quad (9)$$

where ϵ_r is the relative dielectric constant of the material, m^* is the reduced effective mass of the electron and hole in units of the rest mass (m_0) of the electron and is given by

$$\frac{1}{m^*} = \frac{m_0}{m_e} + \frac{m_0}{m_h} \quad (10)$$

Let us consider a semiconducting material in the form of a sphere of radius R , which is of the order of (or less than) the first Bohr radius of the exciton, $R^{(1)}$. Then the exciton states will surely depend on the magnitude of R . We term such samples as spherical quantum dots. The exciton Hamiltonian is the sum of the kinetic energies of electron and hole, the Coulomb interaction energy (V_c) of the e^-h^+ pair, the potentials $V_e(r_e)$ and $V_h(r_h)$ experienced by the electron and the hole respectively due to the barrier. Thus, we write

$$H = -\frac{\hbar^2}{2m_e} \nabla_e^2 - \frac{\hbar^2}{2m_h} \nabla_h^2 + V_c + V_e(r_e) + V_h(r_h) \quad (11)$$

subject to the confinement potential for the quantum dot given by

$$V(r_i) = 0, \text{ for } r_i < R, \quad (i = e, h) \quad (12)$$

$$V(r_i) = \infty, \text{ for } r_i > R, \quad (i = e, h) \quad (13)$$

Neglecting the coupling between electron and the hole ($V_c = 0$) one can represent the exciton wave function as a product of the individual particle wave functions expressed by

$$\Psi(r_e, r_h) = \varphi_e(r_e) \varphi_h(r_h) \quad (14)$$

where $\varphi_e(r_e)$ and $\varphi_h(r_h)$ being electron and hole wave functions respectively. The individual wave functions for the electron and the hole are given by in terms of Bessel functions and spherical harmonics, which reads as

$$\varphi_{lmn}(r) = \left(\frac{2}{R^3} \right)^{1/2} \frac{J_l(\alpha_{nl}(r/R))}{J_{l+1}(\alpha_{nl}(r/R))} Y_{lm} \quad (15)$$

The quantum numbers l , m and n are restricted to $-l \leq m \leq l$; $l = 0, 1, 2, \dots$; $n = 1, 2, 3, \dots$. Here J_l are the Bessel functions of order l , and Y_{lm} are spherical harmonics. α_{nl} is the n^{th} zero of the spherical Bessel function of order l .

The spherical Bessel functions, $j_l(x)$, are related to the Bessel functions of the first kind

$$j_l(x) = \left(\frac{\pi}{2x} \right)^{1/2} J_{l+1/2}(x) \quad (16)$$

The values of α_{nl} and corresponding energy levels are given in table-1.

As the potential at the surface of the spherical quantum dot suddenly becomes infinite, the chance of finding the electron there must be nil. Mathematically, this can be represented as a boundary condition on the solution of the wave equation stated as

$$\left. \varphi_l(r) \right|_{r=R} = 0 \quad (17)$$

so that one can obtain energy levels for the electron and hole given by

$$E_{n,l}^{e,h} = \frac{\hbar^2}{2m_{e,h}} \left(\frac{\alpha_{n,l}^2}{R^2} \right) \quad (18)$$

To understand above facts more precisely, we consider a specific example by assuming a spherical CdS quantum dot of radius R nm having

Table 1. Energy levels of a spherical quantum dot of radius R [38]

n	l	level	$\alpha_{n,l}$	E_h	E_e
1	0	1s	3.1416	$-\frac{9.86965}{m_h} \left(\frac{\hbar^2}{2R^2} \right)$	$-\frac{9.86965}{m_e} \left(\frac{\hbar^2}{2R^2} \right) + E_g$
1	1	1p	4.4934	$-\frac{20.19064}{m_h} \left(\frac{\hbar^2}{2R^2} \right)$	$-\frac{20.19064}{m_e} \left(\frac{\hbar^2}{2R^2} \right) + E_g$
1	2	1d	5.7635	$-\frac{33.21793}{m_h} \left(\frac{\hbar^2}{2R^2} \right)$	$-\frac{33.21793}{m_e} \left(\frac{\hbar^2}{2R^2} \right) + E_g$
2	0	2s	6.2832	$-\frac{39.47860}{m_h} \left(\frac{\hbar^2}{2R^2} \right)$	$-\frac{39.47860}{m_e} \left(\frac{\hbar^2}{2R^2} \right) + E_g$
2	1	2p	7.7253	$-\frac{59.68026}{m_h} \left(\frac{\hbar^2}{2R^2} \right)$	$-\frac{59.68026}{m_e} \left(\frac{\hbar^2}{2R^2} \right) + E_g$
2	2	2d	9.0950	$-\frac{82.71902}{m_h} \left(\frac{\hbar^2}{2R^2} \right)$	$-\frac{82.71902}{m_e} \left(\frac{\hbar^2}{2R^2} \right) + E_g$

bulk band gap $E_g = 2.42$ eV at room temperature. For CdS system, $m_h = m_0$, $m_e = 0.667 m_0$. Then, the energy values (in eV units) may be usefully expressed for the various states (n, l) in terms of R by

$$E_{n,l}^h = - \left(\frac{0.0382}{\frac{m_h}{m_0} R^2} \right) \alpha_{n,l}^2 \quad (19)$$

$$E_{n,l}^h = - \left(\frac{0.0382}{\frac{m_e}{m_0} R^2} \right) \alpha_{n,l}^2 + E_g \quad (20)$$

Quantum mechanics selection rules states that the electron jumps only to those that obey the conditions $\delta n = 0$ and $\delta l = 0$. In otherwords, $1s(h) \leftrightarrow 1s(e)$, $1p(h) \leftrightarrow 1p(e)$, etc. transitions are supposed to be allowed. That is why the absorption or emission spectra would exhibit a blue-shift as the size (R) of the quantum dot is suppressed [38]. Therefore, electron inside a high security jail (here quantum dot) becomes a more energetic species than outside due to band gap enhancement.

1.5 Fabrication techniques

Producing monocrystalline, monodisperse and uniformly distributed quantum particles involve many physical parameters and machine complexities all of which cannot be controlled ideally and simultaneously in a specific route. Each synthetic route has its own advantage and limitations.

The various synthetic processes for nanoparticle formation include: molecular beam epitaxy (MBE) [39-41], electrochemical deposition [42,43], rf- sputtering [44,45], dc-magnetron sputtering [46,47], sol-gel [48], photochemical deposition [49,50], low pressure chemical vapour deposition (LPCVD) [51-53], chemical precipitation in colloids [54], mechanical grinding/alloying [55], magnetron co-sputtering [56,57], vapour deposition on cold substrates and on heated substrates [58,59], selective area metal organic chemical vapour deposition (SA-MOCVD) [60-63].

Recently, ion beam has become an important aspect for synthesis, modification and characterization of nanoparticles. The synthetic procedures include ion-implantation [64-70], ion beam mixing [71-73], ion beam assisted self organized nanostructure formation [74,75] and template synthesis [76-78].

1.5.1 Chemical routes

With adequate care of the processing parameters which affect drastically during the formation of quantum particles, chemical methods

have become convenient and reliable means of synthesizing quantum dot samples with an efficiency level not far behind that by MBE methods.

The prime motivation towards adopting chemical routes are :

- * Simplicity of fabrication
- * Requirement of only inexpensive instruments
- * Relatively shorter synthesis time
- * Possibility of large scale productions
- * Possibility of surface passivation with less difficulty
- * Feasibility of synthesis of metals, alloys, insulators, semiconductors and even compound nanoparticles
- * Possibility of producing single crystalline (monocrystalline) nanoparticles
- * Possibility of doping of large number of materials (Mn, Ni, Fe, Cu etc.) even at room temperature
- * Possibility of coating, capping and coupling of synthesized nanoparticles as per desired stoichiometric proportions
- * Accurate synthesis of nanoparticles in the form of colloids, powders and thin films

Quantum dots have been grown in the hosts such as zeolites [79], porous glass [80,81], miscelles [82,83], membranes [84,85] and anionic polymers [86,87].

1.6 Objectives of the present study

Although synthesis and characterization of compound semiconductor quantum dots have been reported by various workers, there is plenty of gaps to optimize quantum dot properties towards realizing practical applications. A II-VI compound semiconductor is a obvious choice because of large exciton binding energy in comparison with other compound semiconductors, which can be observable (even at room temperature) as excitonic absorption in the optical absorption spectra. Achieving fairly narrow and uniform size distribution by chemical route is encouraging and therefore, it could be a suitable option for large scale productions. Again, quantum dot / nanoparticle formation as well as modification by swift heavy ion irradiation have been studied since a decade ago. On the other hand, ion beam impact on polymer embedded nanoparticles is novel and needs to be unravelled.

Moreover, probing the particles of nanoscale and carrier transport in nanostructured films are impossible due to presence of weak link boundaries. But things get improved when one has a few number of arrayed quantum particles separated by thin dielectric medium under the influence of high intensity light (basically, hi-power pulsed laser). The interfacial charge transfer could be detectable through photocurrent generation in the external circuit, when connected to a biasing source. Previously, the interfacial charge transfer has been reported in coupled, coated and layered systems. But charge transfer in a embedded system

due to resonant excitation of $e-h$ pairs in a weakly confined quantum dot system provides deep insight to carrier tunneling at room temperature. This can be observed in the form of steps in $I - V$ characteristics. These unusual characteristics known as single electron effects, are the prerequisites for single electron transistors (SET). Next, improvement in third order nonlinear susceptibility has been observed in case of reduced dimensional systems. For the application in photonic switching, harmonic generation study of the signals coming out of the quantum dots due to mixing of waves is an important aspect. As many reports are available on account of resonant study and so, we have focused on four wave mixing non-resonantly and analyzed the phase conjugated signals.

The thesis is divided into seven chapters, each of which again split into various sub-sections. The very first chapter is introductory in nature. It discusses background of low dimensional systems (3D to 0D), density of states, energy level alongwith fabrication methods etc. Chapter-2 includes fabrication details and outlines proof of quantum dot formation interms of size determination by XRD, SEM, TEM etc. followed by theoretical illustrations. Chapter-3 deals with thermo luminescence study of surface states alongwith fluorescence emission and exciton absorptions. Study of phonons in nanoparticle system is highlighted in chapter-4. The vibrational features include characteristic longitudinal optic (LO) and surface optic (SO) modes and are discussed through analysis of resonant Raman spectra for CdS nanoparticles in different dielectric media. Swift heavy ion

irradiation experiment alongwith ion induced modified properties of quantum dots are explained in chapter-5. Physical phenomena that encourage possible applications in relevant areas like electronics and nonlinear optics, are elaborated in chapter-6. The same chapter describes single electron effects in quasi-arrayed ZnS/PVOH quantum dot system and nonlinear absorption process and third order optical process in CdS/PVOH semiconductor quantum dots. Conclusion and future directions are highlighted in chapter-7 followed by appendix, references, publications and addenda.



CHAPTER-2

**FABRICATION AND SIZE CONTROL OF
II-VI SEMICONDUCTOR QUANTUM DOTS**

CHAPTER-2

FABRICATION AND SIZE CONTROL OF II-VI SEMICONDUCTOR QUANTUM DOTS

Both large scale synthesis and preservation of nanoparticles is important from application point of view. In order to improve rigidity and to protect nanoparticles from environmental attack, embedding them in glass, zeolites or in polymer is desired. The synthesis of II-VI semiconductor quantum dots in Nafion[®] and Syrlin[®] membranes [88-90] was satisfactory to obtain stable nanoparticles. We have selected wide and direct band gap II-VI group semiconducting systems, as such systems in reduced dimensionality case are capable of showing excitonic absorption even at room temperature due to enhancement in excitonic binding energies. Again, we have chosen polyvinyl alcohol and styrene butadiene rubber latex (SBR) as dielectric matrices for embedding quantum particles.

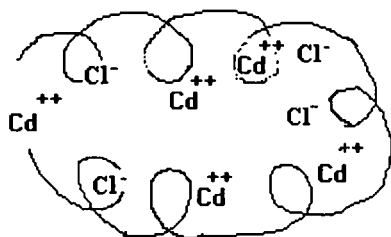
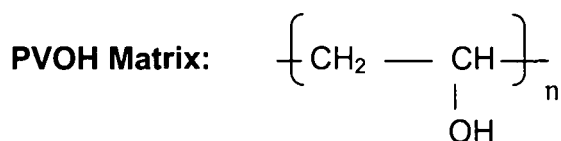
2.1 Properties of used polymer matrices

Structurally, the polymers possess arbitrary coil shaped shapes (figure-7). The free end groups, the number and size of the coils can be controlled as they depend on the molecular weight as well as synthesis parameters (concentration, density and nature of the solvent etc). Thus, they provide unique scope for atomic layer dispersion to form

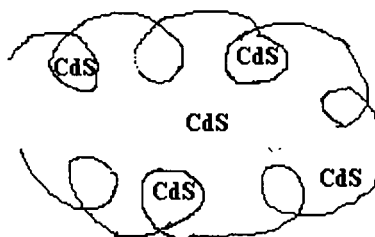
nanoparticles when a proper stoichiometry is maintained in choosing respective salts and solvents.

Polyvinyl alcohol (PVOH)

Unlike many polymers, it is a water soluble solid. It dissolves slowly in cold water but at higher temperature it goes fairly fast into the solution. PVOH solution like starch solution, gives an intense blue colour when reacted with iodine. PVOH is a good protective colloid for aqueous emulsions and is employed for this purpose in a large variety of emulsion and suspension systems. It also finds use in wet strength adhesives.



CdCl₂ mixed with PVOH solution



CdS dispersed with PVOH

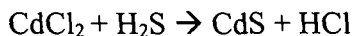


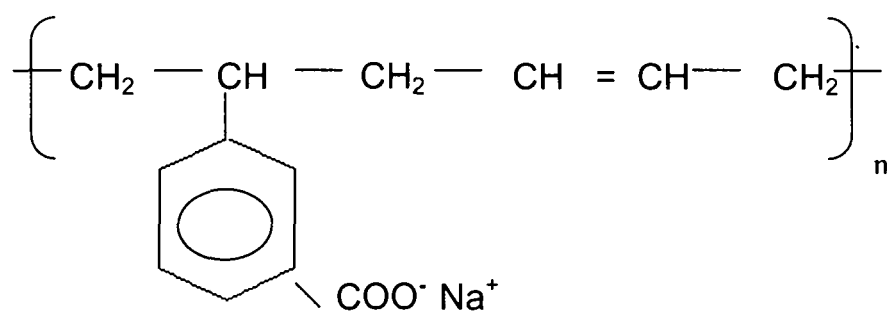
Figure 7(a). Cadmium sulphide quantum dots dispersed in PVOH

Further, it is used in the manufacture of textile fibres, where one major aspect to be taken care of is that the fibre as the final product should be made insoluble in water. PVOH fibres have excellent dimensional stability. They can be easily washed and dried. The fibres are also found to possess excellent resistance to abrasion and remarkable tenacity.

Carboxylated styrene butadiene rubber (SBR) latex

SBR is a synthetic rubber-copolymer of butadiene and styrene. They are made by the free-radical polymerization in an emulsion system using redox initiators such as hydrogen peroxide and ferrous sulfate. The resultant copolymers usually contain 80% of 1,3 (cis and trans) and 20% of 1,2 or 3,4 repeat units.

SBR latex :



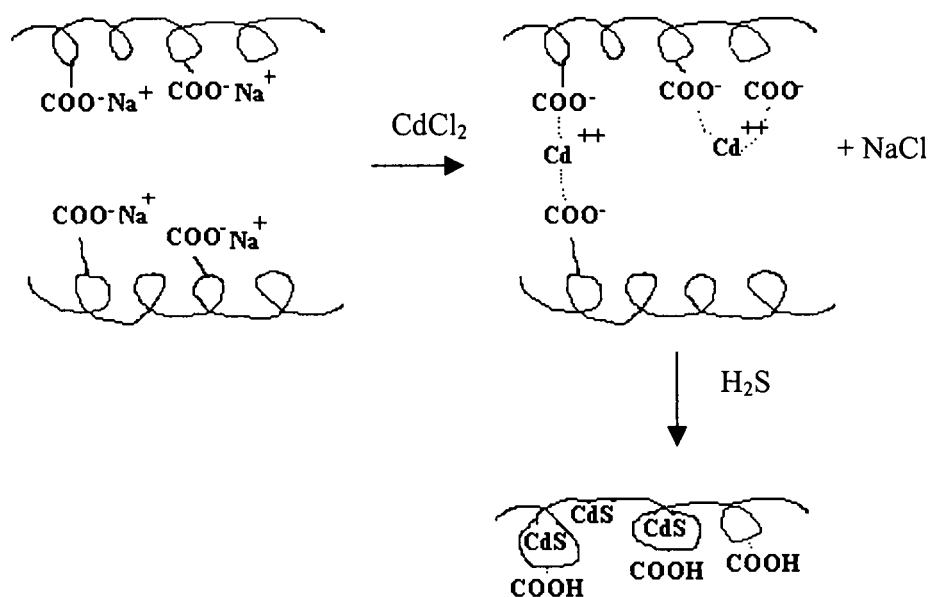


Figure 7(b). Formation of CdS quantum dots in carboxylated SBR latex

The physical properties of the polymers used in the fabrication process are given below in table-2.

Table 2. Physical properties of dielectric polymer matrices

Physical properties	PVOH	SBR latex
Glass transition temperature (K)	343	211
Melting temperature (K)	413	273
Refractive index	1.55	1.53
Specific gravity	1.30	0.93
Specific heat (J/gm-K)	1.66	1.89
Thermal conductivity (W m ⁻¹ K ⁻¹)	2.0	1.34
Molar mass a single structure unit (g)	58.2	221.6
Dielectric constant	2.0	3.1

2.2 Experimental details

Due to several advantages, chemical route is now-a-days followed for growing semiconductor nanoparticles. We have grown quantum particles in the dielectric host matrices by chemical processes illustrated below.

2.2.1 Synthesis of CdS and ZnS quantum dots using PVOH as matrix

- a) 2 % solution of PVOH was taken in a stoppered conical flask and CdCl₂ was added with varying concentration (1-3 wt%) under high stirring rate (200 rpm). The temperature was raised to 70⁰C and stirred for 3 hours. The sample under preparation was kept whole night at room temperature for complete dissolution to get a transparent solution. Again, stirring condition was maintained at least upto 1 hour for the said temperature and N₂-gas was bubbled through the solution for 3 hours. To this solution, H₂S gas was passed directly till no further precipitate of CdS is formed. The CdS nanoparticle containing PVOH films were cast over laboratory glass slides and allowed to dry in a closed chamber at room temperature. The films were washed with cold water 2-3 times to remove Cl⁻ ions and finally films were dried at 50⁰C in an oven.
- b) 2 wt% CdCl₂ solution was taken in a stoppered conical flask and 5 wt% PVOH solution was added under vigorous stirring and heating (60-70⁰C) magnetically for about 4 hours. N₂-gas was

bubbled through this solution for 3 hours. To this solution, freshly prepared 5 wt% ($\text{Na}_2\text{S} + \text{HCl}$) solution was added until the colour turns yellow. The flask was sealed and kept undisturbed for the whole night. Next day, the films were cast over the glass substrate and are dried by means of vacuum oven. The film was washed 2-3 times with cold water to remove Cl^- and films were finally dried in the oven.

- c) For another set, the films were cast at first and then kept in an enclosed vessel and allowed to stay in semidry condition followed by H_2S diffusion reaction. The samples were kept undisturbed for 2-3 days for completion of the chemical reactions. The CdS films were now ready for various experimentations.

Next, ZnS quantum dots were prepared by incorporating their chloride salts (0.25 g-mol ZnCl_2) into 3 wt% aqueous PVOH in a stirring environment which were followed by diffusion treatment of H_2S gas.

2.2.2 Synthesis of CdS quantum dots using carboxylated SBR latex

Carboxylated styrene butadiene rubber (SBR) latex was selected as matrix for fabricating CdS quantum dots.

- a) One coat of SBR latex was drawn over the laboratory glass plates and dried partially to avoid spilling, then they were dipped in 0.4 mol/l CdCl_2 solution for at least 4 hours. Now the film slides were

subjected to ammonia passivation for another one hour and finally washed with distilled water. The whole process was repeated at least thrice. Finally, the samples were injected with drop wise Na_2S solution in acidic medium (2N HCl) until the films glow yellow. Laboratory glass substrates were cleaned and quantum dot films were cast by stretching one over another at once.

- b) 1.5% SBR latex was reacted with 3 wt% CdCl_2 under high stirring condition at $\sim 70^\circ\text{C}$. N_2 -gas was bubbled through the solution followed by H_2S gas treatment. As grown CdS quantum dots on SBR matrix were cast in the form of films over laboratory slides and kept ready for experimentations.

2.2.3 Synthesis of Mn doped ZnS quantum dots using PVOH matrix

First, an aqueous solution of 0.15 M ZnCl_2 and 0.0045 M MnCl_2 was made such that the molar ratio of Mn to Zn was 3:100. The aqueous solution was mixed into as prepared 2.5 wt% transparent polyvinyl alcohol (PVOH) matrix under ~ 200 rpm stirring condition. Temperature was maintained to 65°C . Into this, dropwise injection of Na_2S solution led to the growth of ZnS quantum particles in PVOH matrix. Also, the ZnS nanoparticles are synthesized by grinding as received ZnS powder (99% pure, Lab-Chem) mechanically, followed by sintering ($\sim 900^\circ\text{C}$) and finally quenching

into ice-cold PVOH matrix. Colourless or faint milky coloured Mn doped ZnS samples were developed on the laboratory glass slides.

2.2.4 Preparation of ZnO quantum dots using PVOH matrix

(Quenching method)

0.05 g-mol ZnO powder (99.99% pure, Merck) was taken in a quartz crucible and heated in a furnace slowly upto a maximum temperature of 800⁰C for 6 hours in N₂ atmosphere. 8 wt% aqueous PVOH was made and kept in a specially designed ice-cold environment. The sintered powder was quenched into the aqueous PVOH followed by moderate stirring for about 2 hours. The whole process was carried out in a dark room to avoid the affect of light exposure on the growth mechanism of quantum crystals of ZnO in the polymer host matrix.

2.2.5 Miscellaneous method

A mixture of styrene, acrylic acid (95:5), benzoyl peroxide (0.5% on monomer weight) and methanol were taken in a stoppered conical flask. The contents are then flushed with dry N₂ gas. Polymerization of the copolymer was carried out at the chosen temperature (65⁰C). After the completion of the experiment the films were cast using the same co-polymer. The films were dried in a vacuum oven at 50⁰C followed by neutralisation with ammonia and washed repeatedly

with distilled water and dried in the same environment. The polymer was treated with CdCl_2 (1.5%) solution overnight. It was further washed repeatedly with distilled water and dried. Finally, passivation and exposure to H_2S gas, yield quantum dots/nanocrystallites of CdS. All the parameters and conditions of preparation in the various steps have been optimized by trial and error.

2.3 Principles of size determination

As low dimensional materials exhibit size dependent properties, accurate size measurement is an important task to explore related properties thereof. In brief, we describe here three important methods to guarantee formation of quantum dots in host matrices.

2.3.1 X-ray diffraction (XRD) method

X-ray diffraction (XRD) is the first-hand approach for crystal size investigations. Now-a-days, X-ray diffraction is a routinely used method for estimating average size of ultra small crystallites (quantum dots). In a bulk system, one observes a set of narrowed peaks corresponding to a definite crystal structure (normally, assessed from hkl parameters). However, the diffraction lines at subsequent peaks are found to be broadened with size reduction. Smaller the size of the crystallite, larger is the broadening of the respective peaks. XRD is also helpful in identifying

size distribution of the quantum particles to an appreciable extent by measuring full width at half maxima (FWHM)* of various peaks. The inhomogeneous broadening is due to the nonuniform size variation in the sample. Moreover, XRD provides useful information regarding crystal structure after obtaining information about planes of diffraction. Figure-8 represents XRD pattern of CdS, ZnS and ZnO quantum dots using PVOH matrices. From XRD patterns, Scherrer formula [48,91] can be used for

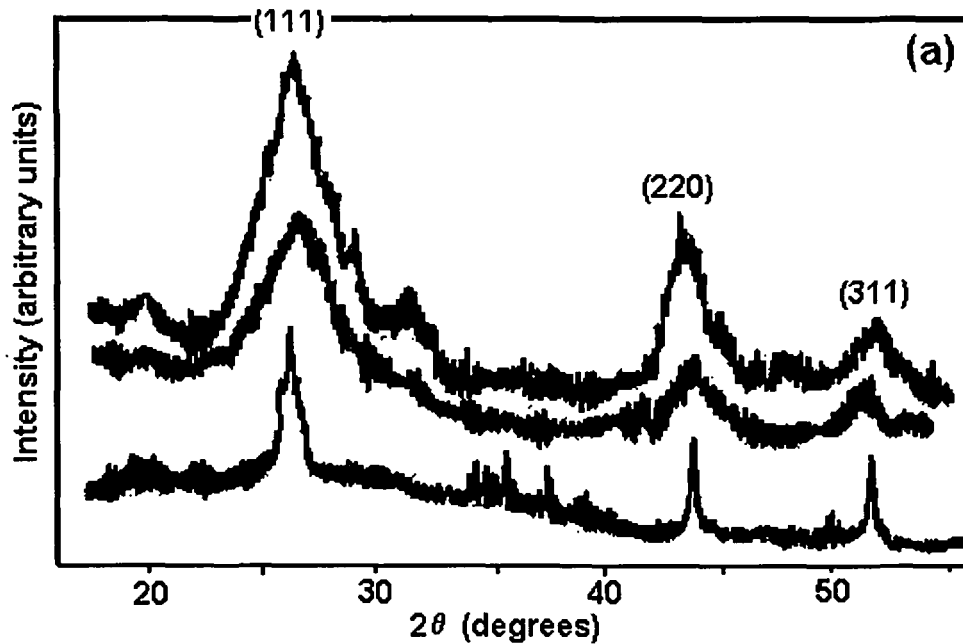


Figure 8. XRD pattern of (a) top to bottom: CdS/PVOH, CdS/SBR quantum dots; and that of bulk CdS

* Appendix-1

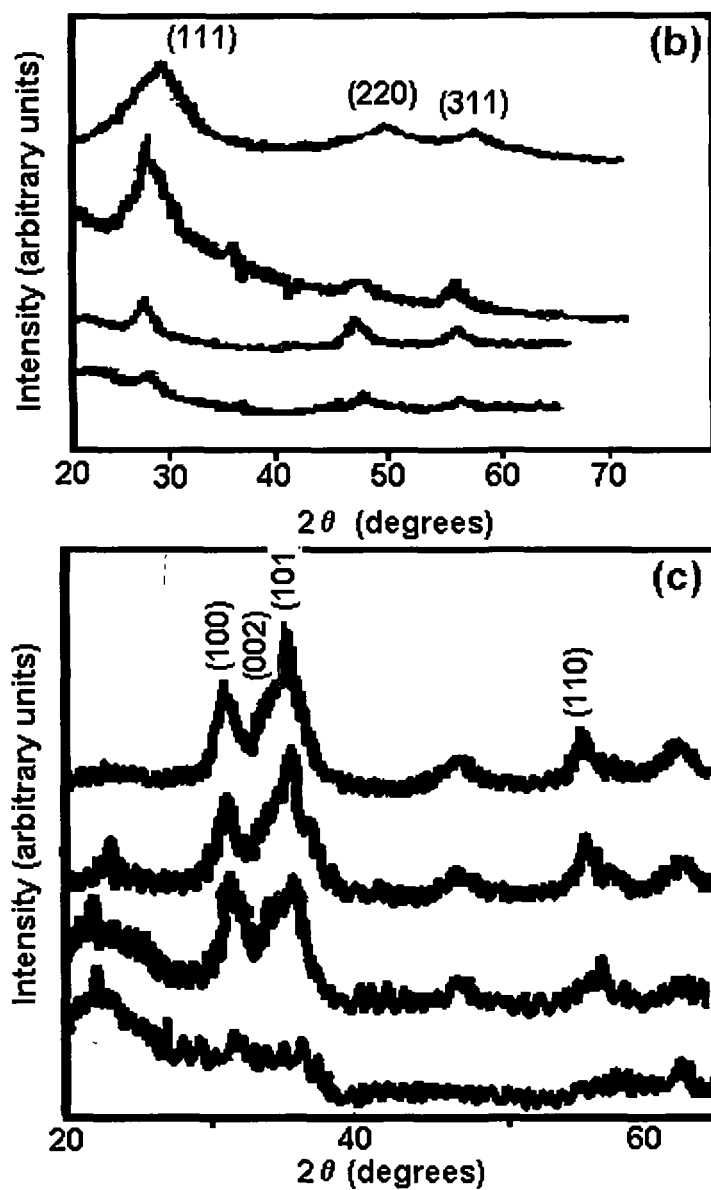


Figure 8. XRD pattern of (b) top to bottom: ZnS/PVOH*, ZnS/PVOH, (c) ZnO/PVOH*, and ZnS/SBR ZnO/PVOH, ZnO/SBR quantum dots

* Synthesis by quenching method

quantum particle size determination. The formula is given by

$$d = \frac{0.9\lambda}{w \cos\theta} \quad (21)$$

where, λ is the wavelength of the x-ray source (Cu $K\alpha$ = 1.541 Å)

w is the full width at half maxima (FWHM) and

θ is the diffraction angle.

Again, fitting the exact plane of diffraction (knowing the exact values of hkl parameters) one can reveal exact structure of the fabricated quantum dots.

X-ray diffraction peaks (111), (200) and (311) of CdS quantum dots in polymer corresponding to $2\theta = 27.4^\circ$, 44.2° and 53° suggests possibility of cubic - β phase. The average size of CdS is found to be 1.8 nm (figure - 8a). The size and strain of the ZnS nanocrystals can be calculated from the diffraction peak $2\theta = 47.2^\circ$ [92]. The peak was corrected for instrumental broadening prior to calculation of its integral breadth. Assuming a Gaussian distribution for the profile due to strain broadening and a Cauchy distribution for the profile due to size broadening, Tan et al. have calculated relative strain and effective size of the ZnS nanocrystals inside pores of silica gel [93]. For our representative PVOH embedded ZnS quantum dots, XRD pattern reveal a cubic phase corresponding to the diffraction peaks (111), (220) and (311) respectively. The size corresponding to the top diffractogram of figure-8b is found to be 51.2 nm.

XRD peaks of ZnO quantum dots exhibit formation of wurtzite phase. Our result is very similar to the report by Spanhel et al. [92]. The diffraction peaks are relatively wider and reflection corresponding to (002) plane appears to be a shoulder. Considering (110) peak, for the top diffractogram of figure-8©, we have measured FWHM, $w \cong 2.51^\circ$ obtaining an average particle size 4.02 nm.

2.3.2 Theoretical models based on blue shift

The blue shifted optical absorption spectra (figure-9) ensure increase in the gap energy of quantum crystals with respect to bulk value (not shown). In the quantum dots, electron in the conduction band and holes in the valence band are confined spatially. As a result of the confinement of both electrons and holes, the lowest energy of optical transition from the valence band to the conduction band increases resulting in the increase in the effective band gap. One can determine the blue shifted energy of the nanocrystallites (E_{gn}) corresponding to the absorption band edge using relation $E_{gn} = hc / \lambda$. The energy shift (ΔE) can be used in established models to estimate size of the relevant quantum dots.

According to Brus et al. [94], the energy of the first excitonic state of a semiconductor nanocrystallite with radius R is given by effective mass approximation (EMA) expression

$$E_{gn} = E_{gb} + \left(\frac{\hbar^2 \pi^2}{2R^2} \right) \frac{1}{m^*} - 0.1786 \frac{e^2}{\epsilon R} - 0.248 E_{RY} \quad (22)$$

where the first term on the right hand side is the band gap of the bulk semiconductor of the particular material, the second term represents the confinement energy (blue shift with respect to bulk) for the electron and the hole, the third term corresponds to $e-h$ coulombic interaction energy and the last term representing bulk excitonic binding energy written in terms of Rydberg energy E_{RY} . The second and the third term compete

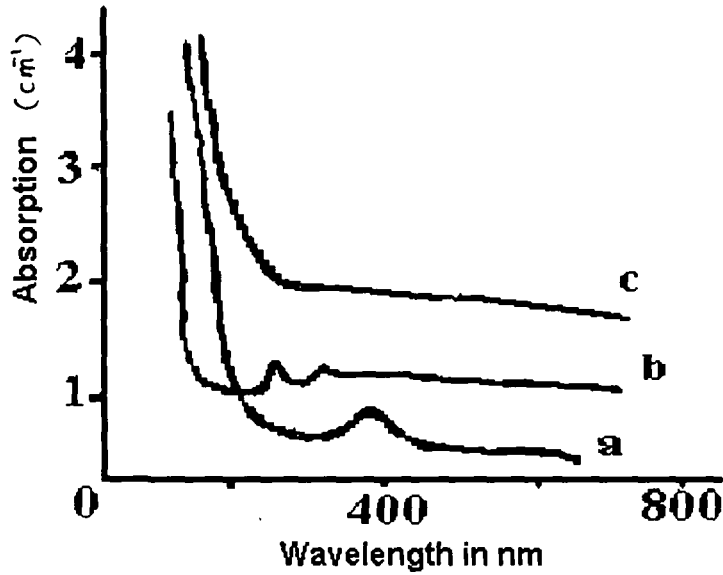


Figure 9. Optical absorption spectra of (a) CdS, (b) ZnO and (c) ZnS quantum dots

each other to redefine the excitonic levels in a quantum crystallite. When the coulomb radius of the quantum particle shrinks to the Bohr excitonic radius then the confinement energy term ($\sim 1/R^2$) dominates over coulomb energy ($\sim 1/R$), which is the case of strong confinement regime. In this

case, coulomb correction to the bulk band gap may be ignored and the electron and the holes are expected to be weakly correlated (individual particle confinement regime). But as size of the crystallite increases, coulomb correction is predominant and hence confinement energy can be ignored (excitonic confinement regime). The strong confinement and weak confinement conditions were analyzed for wide classification of semiconductor nanostructures [95]. Considering the case of individual confinement, coulomb correction can be deleted from the above expression to obtain blue shift energy as per EMA model

$$\Delta E = E_{gn} - E_{gb} = \left(\frac{\hbar^2 \pi^2}{2R^2} \right) \frac{1}{m^*} \quad (23)$$

Also, a hyperbolic band model has been suggested to explain the change of energy gap as a function of particle size [89]. The confinement energy expression of nanocrystallites reads as

$$E_{gn}^2 = E_{gb}^2 + 2 \left(\frac{\hbar^2 \pi^2}{R^2} \right) \frac{E_{gb}}{m^*} \quad (24)$$

$$\Delta E = E_{gn} - E_{gb} = \left(\frac{2 \hbar^2 \pi^2 E_{gb}}{R^2 m^* (E_{gn} + E_{gb})} \right)^{1/2} \quad (25)$$

Table-3(A) represents the blue-shift energy observed in CdS, ZnO and ZnS quantum dots, respectively (figure-9). The increment energy (blue-shift) with respect to bulk was fitted in EMA and HBM to estimate the size of the quantum dots. It was observed that the HBM model

overestimates for CdS and ZnO where size approaches to bulk Bohr radius. However, for ZnS the HBM model under estimates. Similarly, EMA which is appropriate for small crystallites but underestimates for large sized quantum dots due to coulomb correction factor (table-3B). Therefore, a theoretical model which correlate both EMA and HBM may be suggested to suit appropriate size determination of the quantum dots.

Table 3A. Calculation of blue shift energy

Quantum dot Samples	E_{gb} (eV)	Absorption edge-threshold (nm)	Experimental absorption-edge shift (nm)	E_{gn} (eV)	Blue shift energy (ΔE) (eV)
CdS	2.42	515	418	2.992	0.572
ZnO	3.35	375	340	3.678	0.328
ZnS	3.68	340	330	3.789	0.109

Table 3B. Size computation: Correlation between various models

Samples	Confinement size in nm (Exciton Bohr radius, a_B)	m/m_e	Scherrer formula (nm)	EMA (nm)	HBM (nm)
CdS	2.4	0.20	1.78	1.814	8.020
ZnO	1.3	0.27	4.02	2.062	12.428
ZnS	2.2	0.40	51.2	2.939	31.239

The ZnS, CdS films are expected to consist of a large number of quantum crystallites with varying shape and sizes and so the absorption peaks corresponding to level to level interband transitions are less sharp due to the enhanced phonon broadening and inhomogeneous broadening effects [96,97].

Synthesising hydroxyl free ZnO always requires much precautions. It has been reported that ~ 4 nm sized ZnO quantum dots exhibit excitonic absorption features at about 330 nm with and without capping agents [98]. In our case, where the ZnO quantum crystals are supposed to be hydroxyl free (prepared by sintering followed by quenching on polymer matrix) show absorption edge at ~ 340 nm (figure-9). The delayed stronger blue shift in ZnO is attributed to discrete excitonic states and lesser concentration of surface states with respect to CdS and ZnS samples.

2.3.3 Size confirmation through electron microscopy

Neither UV-visible absorption spectroscopy nor XRD is a direct probing method, but confirmation and accurate size measurement of quantum dots is very important and essential prior to study their characteristics. On the other hand, optical microscopy has several limitations with respect to magnification and resolution, it cannot be used to detect materials of size in the nm range. However, electron microscopy solves the problem because it is one of the most vital non-destructive

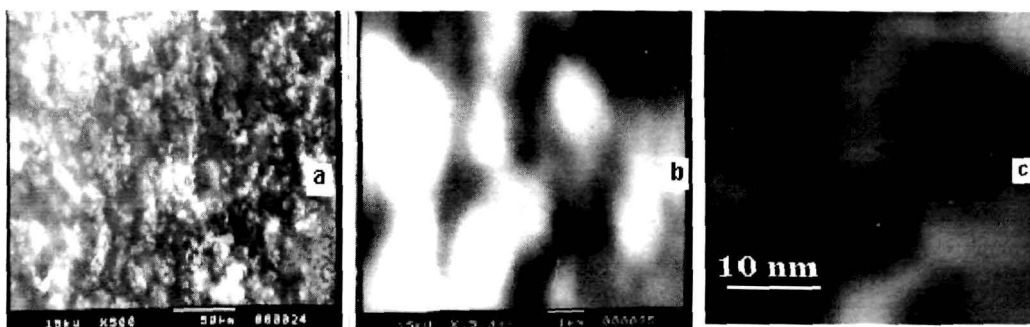


Figure 10. HRSEM (a,b) and HRTEM (c) images of ZnS/PVOH quantum dots

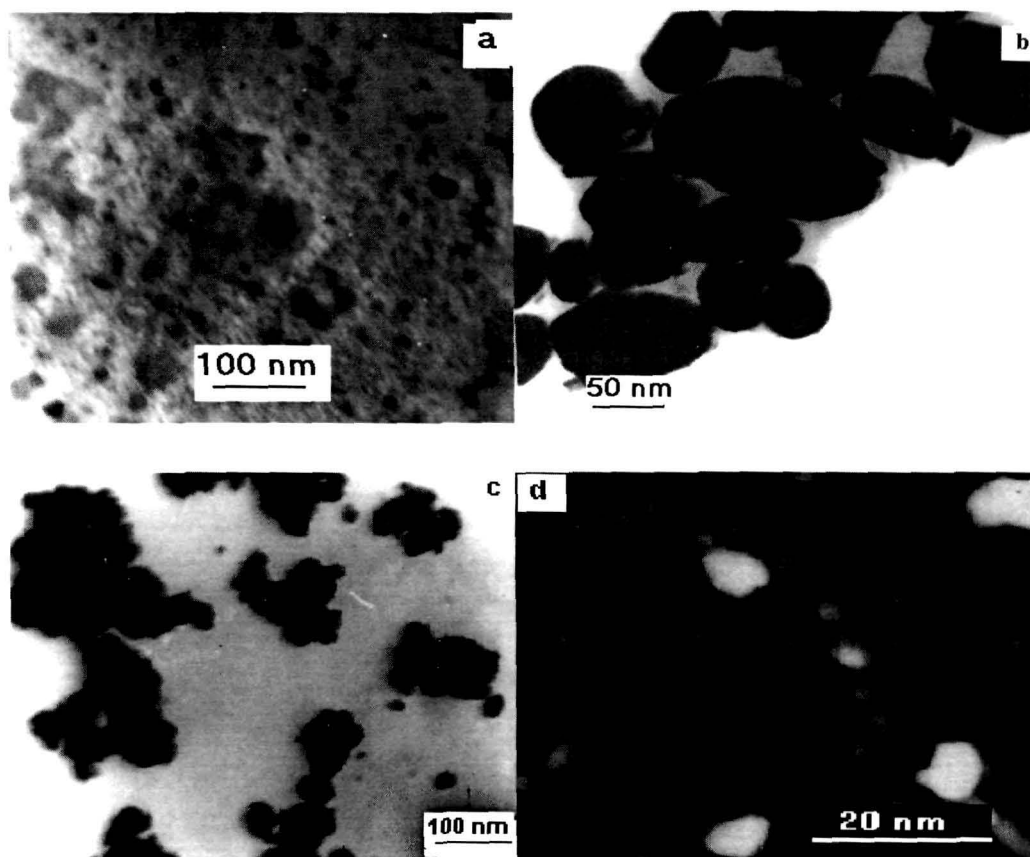


Figure 11. HRTEM images of (a) CdS/PVOH, (b) CdS/SBR, (c) CdS powder and (d) ZnO/PVOH quantum dots

testing method which can probe the particles down to < 1 nm. The sophisticated machines, we have used were scanning electron microscope (JEOL JSM-5200) and transmission electron microscope (JEOL JEM-100CX). Considering HRSEM images as shown in figure-10, we say ZnS quantum dots are densely packed and likely to exist in the form of aggregates. At higher magnification, HRTEM image reveals the size of ZnS quantum dots are in the range 30-40 nm (figure-10(c)). Figure-11(a)-(c) depicts bright field TEM images of nanometric CdS powder and CdS quantum dots in PVOH and SBR matrices. It has been found that quantum dot size down to 1.8 nm is observable for PVOH embedded CdS quantum dots (figure-11(a)).

Relatively large sized particles ~ 50 nm are found incase of SBR matrix which is represented in figure-11(b). The probable cause is due to rigid and atactic nature of PVOH with respect to SBR, which is an elastomer and relatively flexible, which leads to coalesce of smaller particles. Figure-11(d) shows bright field image of ZnO quantum dot depicting nearly spherical quantum dots of average size 2.2 nm.



CHAPTER-3

**CARRIER TRAPPING MECHANISM AND
THE ROLE OF SURFACE STATES**

CHAPTER-3

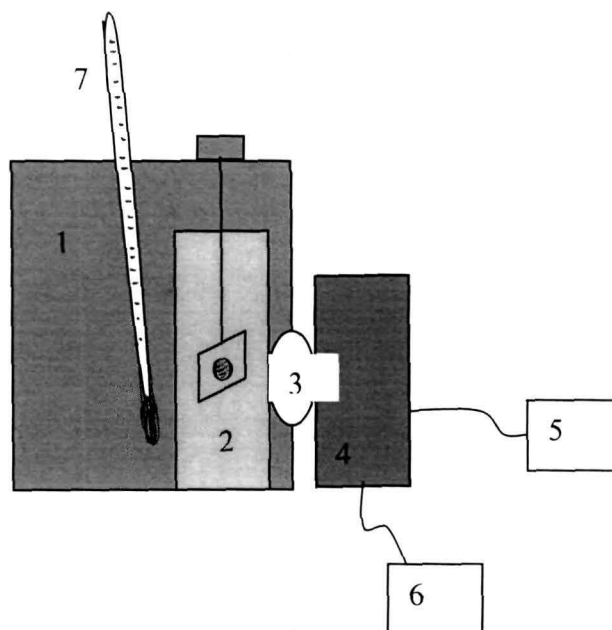
CARRIER TRAPPING MECHANISM AND THE ROLE OF SURFACE STATES

While going down to nanometer range, i.e. to a limit when even size dependent atomic properties can be featured, one has to consider surface properties. It is known that, due to extremely high value of surface-to-volume ratio, there exist huge number of surface defects. These defects are directly responsible for various luminescence patterns depending on the nature of charge trapping and detrapping process.

3.1 Thermoluminescence study of surface states

It is well known fact that trapped carriers are produced during sample processing or exposure to high frequency photons for a short duration. The trapped electrons can be detrapped and excited to the conduction level in a controlled thermal heating environment. If these excited electrons fall into recombination center (usually, where a '+ve' carrier resides) one observes luminescence. If the source of detrapping is 'heat' the luminescence is termed as thermo luminescence (TL). Technically, accurate term is thermally stimulated luminescence (TSL) rather than TL signifying the fact that heat merely stimulates the emission, not the excitation [99]. The glow curves are produced by the trapped carriers. As size of the particle decreases, surface states tend to

increase because of the enhancement of s/v ratio and so, most of the atoms are distributed over the surface of the nanocrystallites. As depicted



- 1- Oven/heater (upto 200⁰C)
- 2- Cuvette containing quantum dot sample in the form of films
- 3- Quartz tube (4x1x1cc)
- 4- Photomultiplier tube (PMT) model:931A, range 300 nm-650 nm
- 5- EHT power supply to PMT
- 6- Digital current meter model: DNM121
- 7- Thermometer (0-200⁰C)

Figure 12. Scheme of experimental set-up for thermo luminescence study

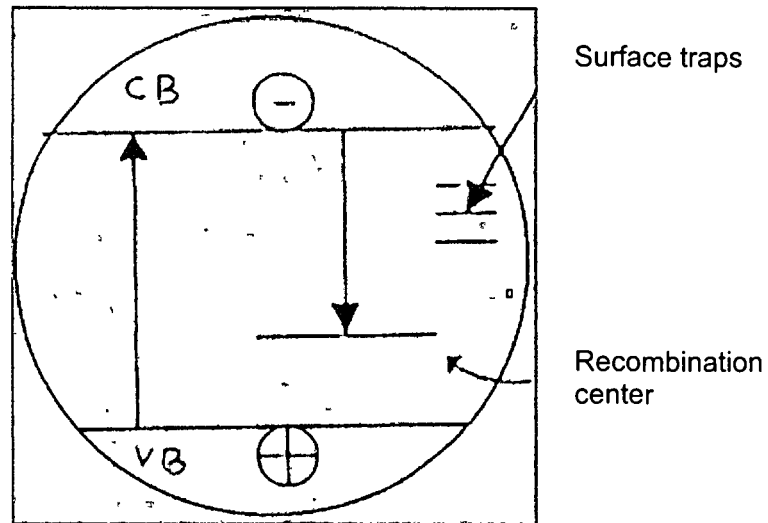


Figure 13. Schematic representation of surface states over a quantum dot

in figure-13, during synthesis a number of surface states are produced corresponding to different activation energies (E_A) which determine trap depths. In case of nanoparticles, the number is significantly high with extremely small activation energy differences (fractions of meV). These surface states which are nothing but the defect sites can act as trapping centers for '-ve' carriers (i.e., electrons). The nature of temperature dependent luminescence intensity plot (figure-14) is an unexpected signature of almost uniform emission of photons measured in terms of photocurrent which assess that e^-h^+ recombination takes place at slow rate. The experimental set up for TSL study is shown in figure-12.

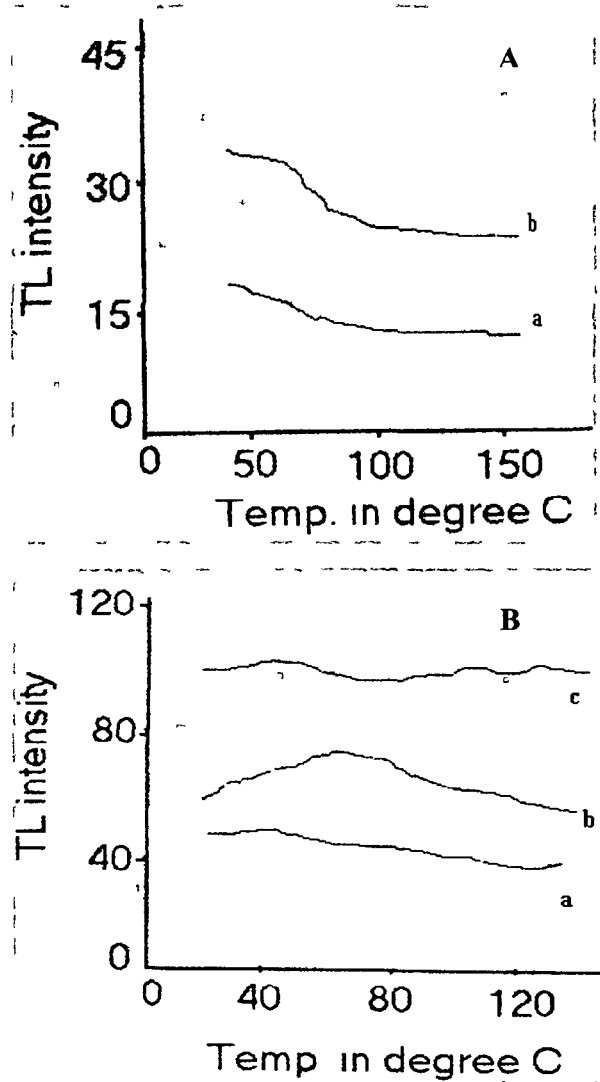


Figure 14. Thermo-stimulated response of (A) CdS quantum dots deposited over (a) plain glass substrate and (b) Ag coated glass substrate, (B) ZnS quantum dots deposited over (a) plain glass substrate and (c) Ag coated glass substrate. The response of ZnO quantum dots deposited over plain glass slides is shown in B(b)

We shall try to interpret our experimental plots with regard to first order and second order kinetics as the defect sites over the quantum dots may involve slow retrapping and fast retrapping processes respectively. The general one trap (GOT) expression for TL emission as given by Levy et al. [100]

$$I_{TL} = (ns)e^{\frac{-E_t}{kT}} \left[1 - \frac{(N-n)\sigma_n}{(N-n)\sigma_n + m\sigma_{mn}} \right] \quad (26)$$

Here ns being the net number of trapped electrons in the surface states, σ 's being respective capture cross sections, the term in the square bracket is the probability that the thermally released electrons will not be retrapped and the ratio $(N-n)\sigma_n / m\sigma_{mn}$ is the ratio of the retrapping to the recombination probability. We know that the excited electrons recombine with holes to give luminescence. As temperature increases the ratio of emptying of trap centres increases until all trapping centres become empty. Now two cases arise:

- (1) whether the released electrons retrap in some other surface states (fast retrapping) or,
- (2) recombine with a free charge of opposite kind (slow retrapping)

3.1.1 First order kinetics (slow retrapping)

Under slow retrapping conditions (where negligible retrapping is to be assumed during thermal excitation) the recombination probability is the dominant factor for which the GOT equation becomes

$$I_{TL} = (ns)e^{\frac{-EE_t}{kT}} \quad (27)$$

For a first order process, the rate of emptying the trapping sites $-dn/dt \propto n$. Integrating $t = 0$ to t and using a constant heating rate, $\beta = dT/dt$, yields the well known Randal-Willkins [101] first order expression for the function $I_{TL}(T)$, namely

$$I_{TL} = (n_0s)e^{\frac{-E_t}{kT}} \exp\left\{-\left(\frac{s}{\beta}\right) \int_{T_0}^T \exp\left(-\frac{E_t}{k\theta}\right) d\theta\right\} \quad (28)$$

where n_0 is the initial values of n at $t = 0$ and θ is a dummy variable representing temperature. Here, recombination plays a dominant role over retrapping and so we have the condition $m\sigma_{mn} \gg (N-n)\sigma_n$ and we argue that there is possibly plenty of active surface states from which electron gets detrapped after being excited by thermal means. Detrapping of electrons is followed by recombination with charge of opposite kind at the recombination centers thus giving different glow peaks corresponding to different activation energies. Again, the peak height decrease with

increase in activation energy and as the recombination process is ultra-fast the exact plot is a superposition of many glow peaks to give reduced rate in TL intensity with temperature (figure-15). Thus, we obtain suppression of recombination even if we say that recombination predominates over retrapping.

3.1.2 Second order kinetics (fast retrapping)

Here retrapping dominates over recombination i.e., $m\sigma_{mn} \gg (N-n)\sigma_n$. Applying this inequality to the GOT expression, along with the condition that the number of surface states is large compared to the number of trapped electrons ($N \gg n$) and number of recombination

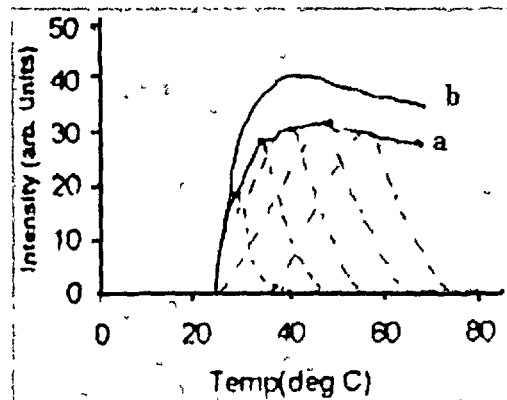


Figure 15. TSL plots of (a) CdS/SBR and (b) CdS/PVOH quantum dots. Schematic representation of superposition (----) of various glow peaks lead to flat response

centers equals to the number of trapped electrons ($n = m$) yield

$$I_{TL} = -\frac{dn}{dt} = s \left(\frac{\sigma_n}{N\sigma_{nm}} \right) n^2 e^{-\frac{E_t}{kT}} \quad (29)$$

With the additional assumption that $\sigma_{mn} = \sigma_n$ as long as $m = n$ we obtain Garlick-Gibson [102] TL equation for second order kinetics which reads as

$$I_{TL} = \frac{n_0^2 s}{N} e^{-\frac{E_t}{kT}} \left[1 + \left(\frac{n_0 s}{\beta N} \right) \int_{\tau_0}^{\tau} \exp\left\{-\frac{E_t}{k\theta}\right\} d\theta \right]^{-2} \quad (30)$$

It is to be noted that here retrapping probability \gg recombination probability. It means that after vacating the surface states a significant concentration of electrons try to retrap again (may be in some other surface state) before they could recombine finally with the holes at the recombination centers. That is why one gets delayed TL emission and a spreading out for a wide range of temperature (figure-14 & 15).

Luminescence in the nanocrystallites depends on the energy gap, oscillator strength and the excitonic binding energy [103]. All these factors are size dependent and hence the knowledge about well approximated size estimation plays vital role for enhanced luminescence efficiency. Factors such as the presence of nonradiative centers on the crystallite surface also affect luminescence. For small surface area, the probability

of existence of nonradiative centers is small as indicated by high and stable luminescence efficiency.

I_{TL} vs T of the quantum dots display peculiar flat response. The thermally excited electrons from the different surface states of the quantum dots take time for radiative recombination because of high density of trapping centers. So, because of enhanced surface states (traps), there is large probability of electron retrapping occurring from one surface state (from where electron has been excited to the conduction band) to the other before recombining with the hole at respective recombination center. Therefore, we have observed a uniform distribution of intensity over a certain range of temperature in case of CdS and ZnS samples (figure-14). Of course, the maximum intensity depends on the number of traps which in turn depend on the particle size, material type and nature of the surrounding medium over which they are deposited. Figure-14 B(b) justifies less number of surface states for ZnO quantum dots as a glow peak was observed corresponding to 72⁰C. Left portion of the peak describes emptying of the carriers from the surface states and right half represent recombination of the carriers at respective recombination sites. The *glow peak* corresponds to the temperature at which all the carriers have been emptied from the quantum dots. Recently, the electronic relaxation has been found to be sensitive to the solvent and insensitive to the particle size [104]. Ultrafast dynamics in semiconductor quantum dots is quite new and a novel issue by which relaxation response

of the carriers and their interaction with the phonons, other carriers and the surfaces are being extensively studied [105-107]. The effect of size on dynamic properties of charge carriers is still not well understood [108]. Compared to the bulk, two major phenomena occur which seriously affect electron life time. First, as the size decreases density of surface states is enhanced which tend to weaken the electron-phonon interaction. Thus, the electron life time is expected to increase with size. Second, spatial confinement lead to stronger interaction between electron and hole which increases the possibility of electron-hole recombination, thus reducing electron life time. In addition, the life time may be affected by the surface properties due to high density of trap states, which lead to significant nonradiative decays and shortens the life time. In the room temperature environment the phonon contribution cannot be totally denied. Since a huge percentage of the atoms in a quantum dot are on the surface, where dangling bonds, adsorbed species etc. produce traps for electrons and holes, the fate of the charge carriers generated by light absorption is strongly dependent on the existence of these traps [109].

3.2 Optical stimulated luminescence (OSL)

In recent years, OSL has become a popular method for determining equivalent doses for sedimentary deposits in dating applications and is growing in popularity in dosimetric applications [110,111]. Although applications in dosimetry have been less extensively reported, despite

obvious advantages: e.g., no need to heat the sample, avoidance of thermal quenching use of plastic dosimeters, etc. The descriptions of OSL from a variety of dosimetric materials have been reported [112,113]. Likewise thermo-stimulated luminescence, optical stimulation ($h\nu < E_g$) may drive surface states in participating in the mechanism of retrapping and recombination of carriers. The experimental set up is very similar to TSL set up (figure-12) except the fact that a 0.5 mW He-Ne laser ($\lambda = 532$ nm) was illuminated (5 minutes) removing the oven into the cuvette containing quantum dot sample (colloid form). Figure-16 depicts stable signature of OSL intensity over a large period of time. As photons have less energy than that of E_g of CdS, ZnO and ZnS samples, so there cannot be interband transitions to form excitons. Therefore, only surface state

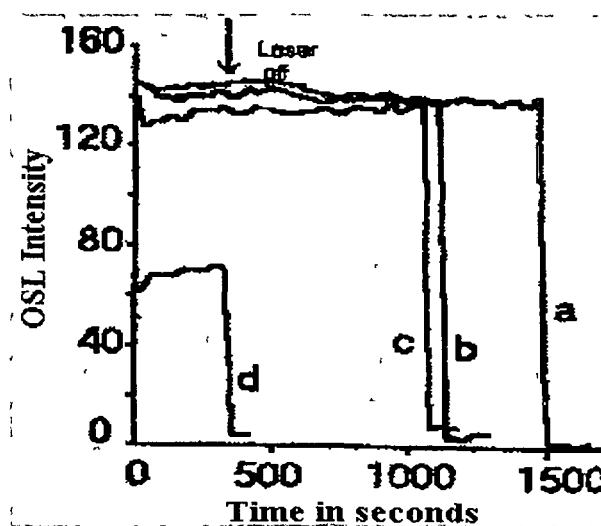


Figure 16. Optically stimulated luminescence pattern of (a) CdS, (b) ZnO, (c) ZnS and (d) damaged ZnO quantum dot samples

involvement will be the major issue to keep the intensity stable over significantly large time periods (e.g. 780 s for ZnS and 1140 s for ZnO). Thus, the role of surface state in suppressing the recombination emission is believed to be important aspect in case of quantum dots, for large s/v ratio.

In conclusion, we claim that both order kinetics fit well for suppression of recombination emission with respect to TSL curves which keep the thermo stimulated photo emission pattern for a longer period as a result of modified trapping mechanism. So, the process belong to *mixed order kinetics* in which, order of kinetics depend upon dominance of either retrapping or recombination process. Again, OSL response depicts strong involvement of surface states thus reducing recombination probabilities.

3.3 Excitonic absorption and surface states

Most of the time resolved measurements are pursued with the intention of the influence of the surface states in the excitonic or band edge fluorescence of quantum dots. The idea of direct observation on the interaction between the excitons and the surface states (trapped carriers) from OAS was cancelled by Chestnoy et al. [114]. The probable cause may be the contents of surface states are too low to be measured in the optical absorption spectra. The surface states increased largely in case of uncapped and not well passivated nanoparticles. The surface states signals have been observed successfully in case of chemically grown

uncapped ZnS systems [115]. Although in case of nanoparticles, s/v ratio is high and surface states are inherent, surface state signals are not detectable in OAS in capped systems.

In case of ZnS quantum dot systems, in addition to interband transition or exciton absorption band at around ~ 300 nm, second absorption band in the long wavelength region was detected [3,9,115,116]. The second band was suggested to be caused by the presence of surface states of the ZnS nanoparticles. Moreover, Chen et al. have confirmed this by studying absorption behaviour of encapsulated ZnS into the cages of (Zeolite-Y) and uncapped ones. The reduction of surface states in case of well passivated samples have been reported [117]. The evolution of second band arise due to the surface states, as the absorption is lying below the absorption edge of the particles, i.e., the absorption energy is lower than the band gap of the particles [115]. The strong trapped fluorescence arising from the surface states of capped, passivated nanoparticles have been found in literature [83,118-120].

We have selectively chosen CdS quantum dots embedded in PVOH matrix to reveal various energy states. The optical absorption spectra (OAS) of CdS/PVOH is shown in figure-17. It is found that when the the semiconductor- to- the polymer ratio is increased, or decreased the absorption response is strongly influenced. However, we observe 3:1 ratio is a better choice to work with from application point of view, as it shows broad excitonic band.

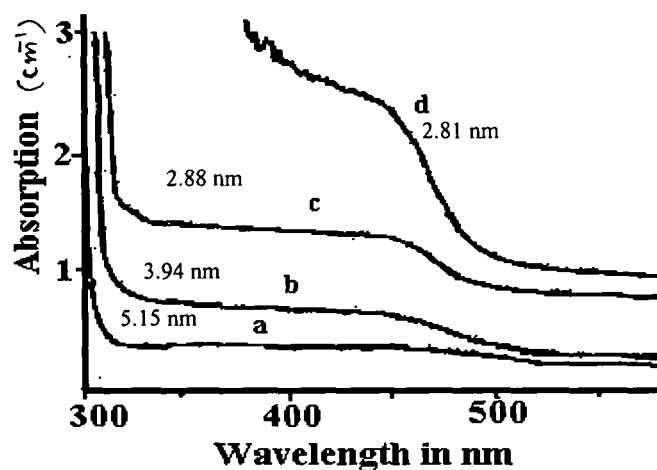


Figure 17. Optical absorption spectra of CdS/PVOH quantum dots with different CdS:PVOH ratios e.g. a) 6:1, b) 1:1, c) 1:3 and d) 3:1

All the spectra (figure-17) as obtained from the spectrophotometer were analyzed by a novel computing technique*. In this technique the picture is first digitized using standard software MATLAB®. The output data then analyzed using Microsoft spread sheet programs. The spectra obtained with wavelength-to-energy conversion (using digitization) is represented in figure-18(A). The first derivative of well resolved 3:1(oas1),1:3(oas2) and 1:1 (oas3) quantum dot samples are shown in figure-18(B).

* Appendix-2

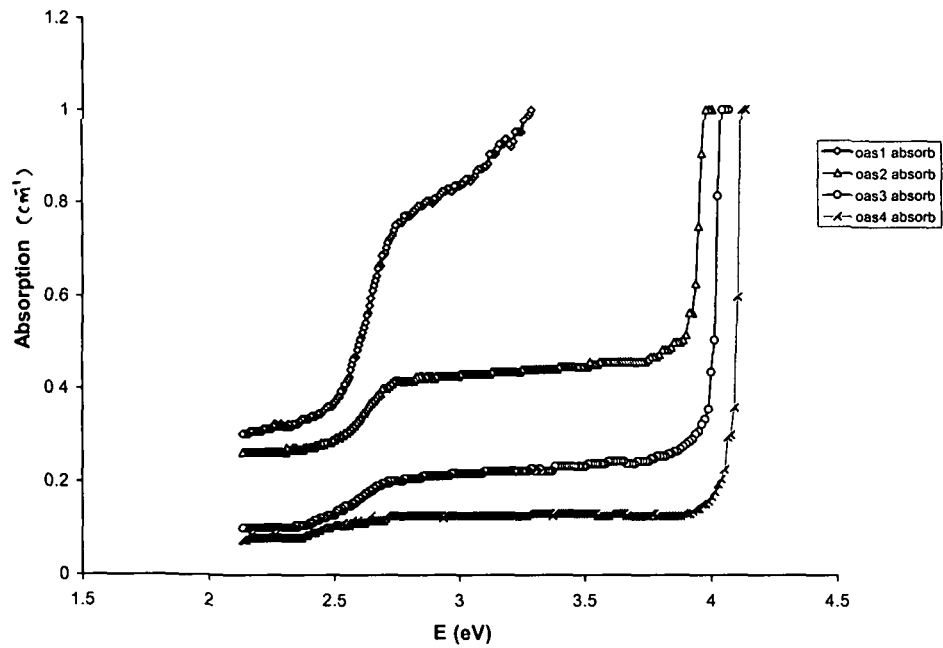
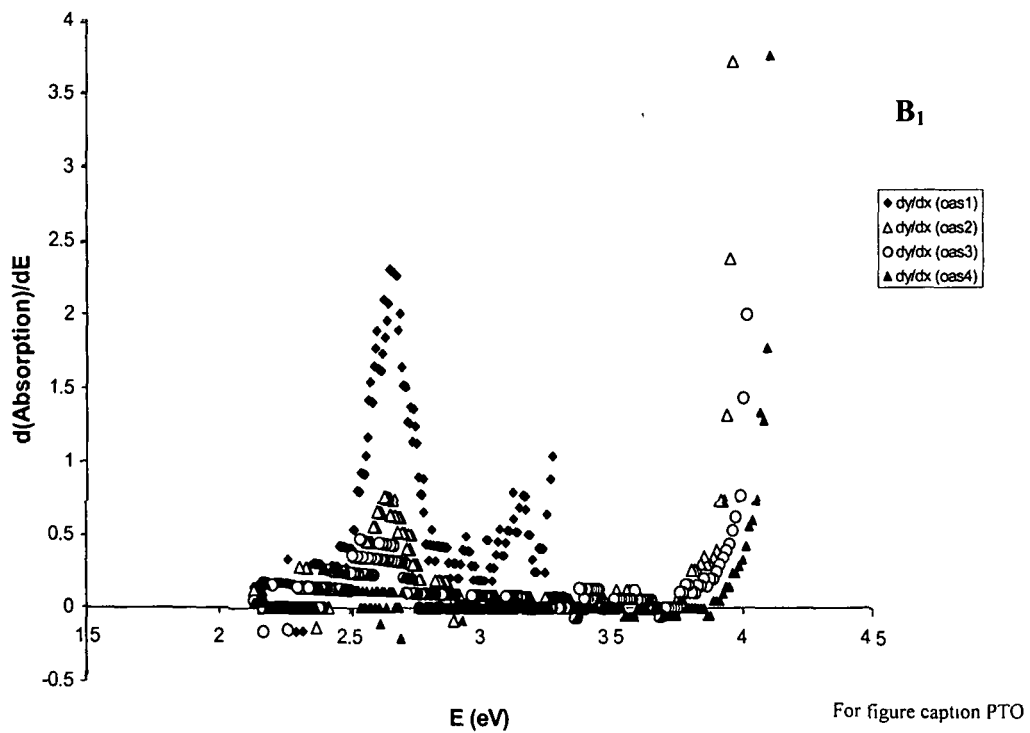


Figure 18(A). OAS spectra obtained from digitized data (figure-17)



For figure caption PTO

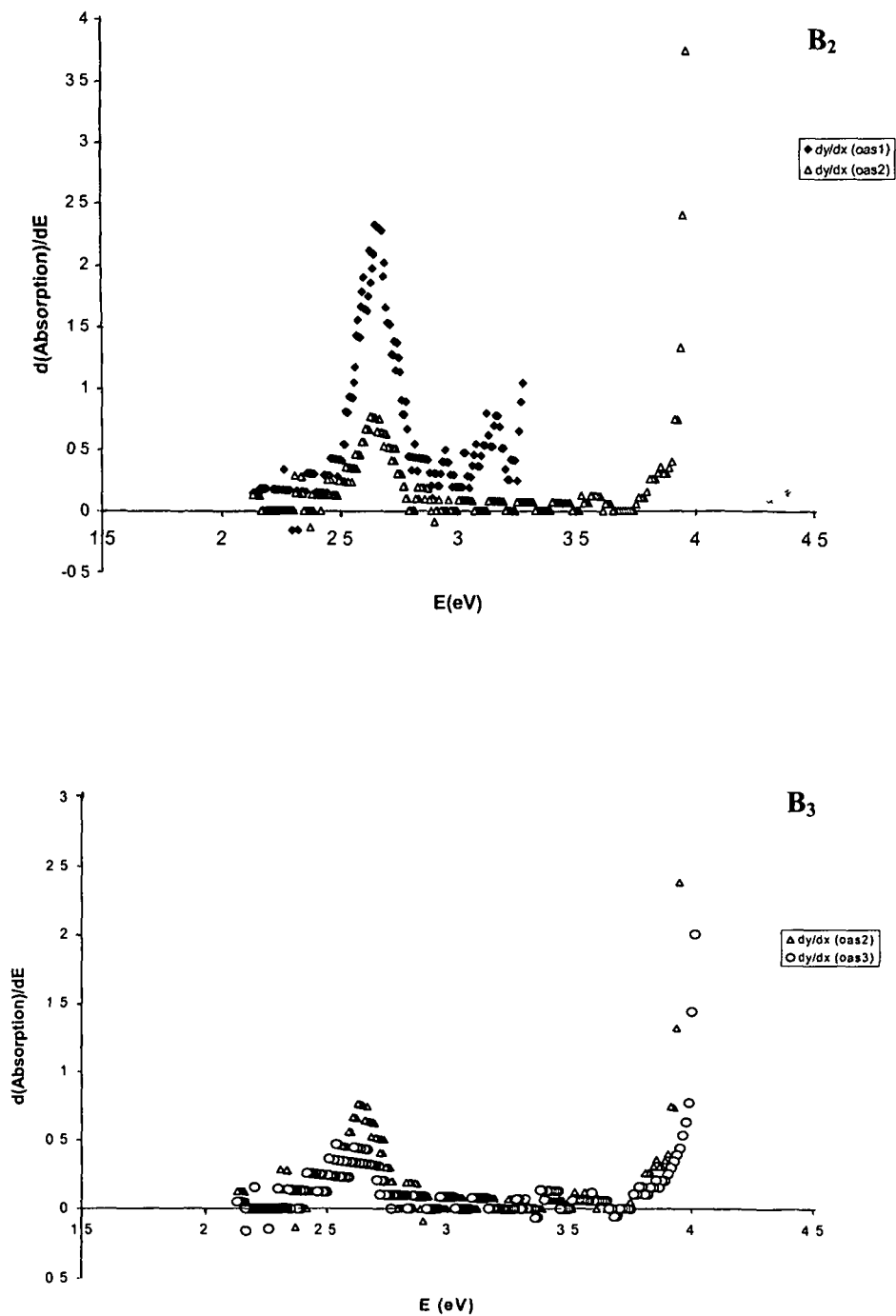


Figure 18(B) First derivative absorption response to energy of (B₁) 3 1(oas1), 1 3(oas2), 1 1(oas3), 6 1(oas4), (B₂) 3 1,1 3 and (B₃) 1 3,1 1 CdS quantum dots

Thus, we are successful in observing blue shift corresponding to various samples and in detecting most probable lowest excitonic transition levels (table-4 and figure-18) .

Table 4. Excitonic transition levels in CdS quantum dots

Sample type (CdS:PVOH)	Energy Peaks (eV)	Blue-shift (ΔE) (eV)	Absorption (cm^{-1})	Probable transition (Excitonic)
Oas-1 (3:1)	2.653 (Ω_1)	0.233	0.612	$1S_{3/2}(h) - 1S(e)$
	2.949 (Ω_2)		0.8245	$2S_{3/2}(h) - 1S(e)$
	3.123 (Ω_3)		0.904	$1S_{1/2}(h) - 1S(e)$
Oas-2 (1:3)	2.631 (Ω_1)	0.211	0.358	$1S_{3/2}(h) - 1S(e)$
	2.831 (Ω_2)		0.426	$2S_{3/2}(h) - 1S(e)$
Oas-3 (1:1)	2.541 (Ω_1)	0.121	0.149	$1S_{3/2}(h) - 1S(e)$
Oas-4 (6:1)	2.491 (Ω_1)	0.071	0.106	$1S_{3/2}(h) - 1S(e)$

If one look at the very first excitonic transition, one gets relevant information with respect to blue shift. As a bulk CdS has a band gap of 2.42 eV at 298⁰K. So, the blue shift amounts for Oas-1 to Oas-4 would be 0.238 eV, 0.211 eV, 0.121 eV and 0.071 eV respectively. The features of Oas-3 and 4 are not well resolved and so did not give any information to next transitions. Therefore, we claim that in order to notice multi excitonic transitions, the ratio 3:1 is appropriate stoichiometry for CdS : PVOH.

In the effective mass approximation (equation-22) the average quantum dot sizes for 3:1, 1:3, 1:1 and 6:1 samples are 2.81 nm, 2.99 nm, 3.94 nm and 5.15 nm. Due to the size dependence of carrier energies, optical spectra of quantum dots are strongly affected by inhomogeneous broadening which smears out the discrete structure of optical transitions resulting from three dimensional confinement [121]. In the strong confinement regime, the size dependence of energy transitions in quantum dots is dominated by a term proportional to $1/R^2$ (equation-22). In this case, the broadening of transitions ($2\hbar\Gamma_{\text{inh}}$) arising from a size distribution can be estimated from the expression $2\hbar\Gamma_{\text{inh}} = (4 \delta a/a) \Delta E$, where ΔE is the confinement induced shift of the optical transition, and δa is the halfwidth of the size distribution [121]. With $\delta a/a = 5\%$, typical for the best colloid samples [121] and $\Delta E = 0.238$ eV, 0.211 eV, 0.121 eV and 0.071 eV for 3:1, 1:3, 1:1 and 6:1 quantum dot samples; the inhomogeneous line widths are calculated to be 47.6 meV, 42.2 meV, 24.2 meV and 14.2 meV, respectively.

3.4 Fluorescence emission of quantum dots

Fluorescence emission is normally observed from the first excited singlet state of the molecule. Even if the electronic transition promotes the molecule to an energy state higher than s_1 (first excited state), the excess energy in condensed systems is dissipated away to the surroundings as thermal energy and the molecule comes to stay in the lowest excited

state. In this state it has a life time governed by the transition probabilities of absorption. In the absence of any deactivating perturbations, the molecule has a natural radiative life time, τ_N , inversely related to the integrated absorption intensity as given by ,

$$\tau_N = \frac{3.47 \times 10^8}{n^2 \nu_{\max}^2} \left(\frac{g_m}{g_n} \right) \frac{1}{\int \epsilon_\nu d\nu} \quad (31)$$

where g_m/g_n is a multiplicity correction factor, useful for intercombination transition between a singlet and a triplet state and the expression is for molecules dissolved in a medium of refractive index n . Here g_m and g_n are the spin statistical factors for the upper and the lower energy states, respectively. For singlet \rightarrow singlet transition, $g_m = 1$, and $g_n = 1$; for triplet \rightarrow singlet transition $g_m = 3$, $g_n = 1$. A more refined expression is given by Forster,

$$\frac{1}{\tau_N} = 2.88 \times 10^{-9} n^2 \int \frac{(2\nu_0 - \nu)^3}{\nu} \epsilon_\nu d\nu \quad (32)$$

All those factors which effectively alter the radiative life time are the same as those which cause variation in oscillator strength in absorption. The rate constant for fluorescence emission k_f is defined as

$$k_f = \frac{1}{\tau_N} = \frac{1}{\tau_0} \quad (33)$$

In the presence of other competitive deactivating processes, the average lifetime is much reduced and actual lifetime τ_f is

$$\tau_f = \frac{1}{k_f + \sum k_i} \quad (34)$$

where $\sum k_i$ is the rate constant for the i^{th} competitive process, assumed to be unimolecular. Due to the working of the Franck-Condon principle and thermal relaxation of vibrational modes, the fluorescence spectrum is always observed on the red side of the absorption spectrum, in approximate mirror image relationship for polyatomic molecules. This redshift of the fluorescence implies that the emitted quanta are of lower energy than the absorbed quanta i.e., $h\nu_f < h\nu_a$; Stoke's shift. Under certain conditions at high temperatures, when higher vibrational levels of the ground state are thermally populated, anti-Stokes effect ($h\nu_f < h\nu_a$) may be observed. Generally, there is an overlap region between absorption and emission spectra (figure-18(A) and 19). The intensity distribution in fluorescence spectra is independent of the absorption wavelength as long as the emission occurs from vibrationally relaxed upper state, emphasizing the Boltzmann distribution of molecules in the emitting state. Mirror image relationship (Levshin's rule) [122] in FL spectra is not observable if the excited state has very different geometry from that of the ground state as is usually the case for small unconjugated molecules.

The quantum efficiency of fluorescence, ϕ_f is defined as

$$\begin{aligned}\phi_f &= \text{number of quanta emitted} / \text{number of quanta absorbed} \\ &= \text{Intensity of emission (F)} / \text{Intensity of absorption (I}_a\text{)}\end{aligned}\quad (35)$$

In condensed systems, radiationless pathways are most common deactivating mechanisms. Since these deactivating processes also reduce the radiative lifetime, the measured lifetime τ_f is related to ϕ_f through τ_f^0 , the intrinsic lifetime as

$$\tau_f = \phi_f \tau_f^0 \quad (36)$$

Because of the independence of quantum efficiency on wavelength it is possible to obtain a fluorescence excitation spectrum which is defined and derived as follows:

Intensity of fluorescence F varies as fractional light absorption I_a , that is

$$F = \phi_f I_a = \phi_f I_0 \{1 - \exp(-2.303 \epsilon l C)\} \quad (37)$$

where ϕ_f is fluorescence quantum efficiency; I_0 is incident light intensity; ϵ the molar extinction coefficient, C the concentration in moles per litre and l is optical path length. For small fractional absorption, the exponential term can be expanded and one obtains,

$$F \approx 2.303 \phi_f I_0 \epsilon l C \quad (38)$$

Since ϕ_f is independent of wavelength, if F is measured as a function of wavelength of exciting light of constant intensity I_0 , the resulting variation in fluorescence intensity (called as fluorescence excitation spectrum) will reflect the variation in molar extinction coefficient (ϵ), as a

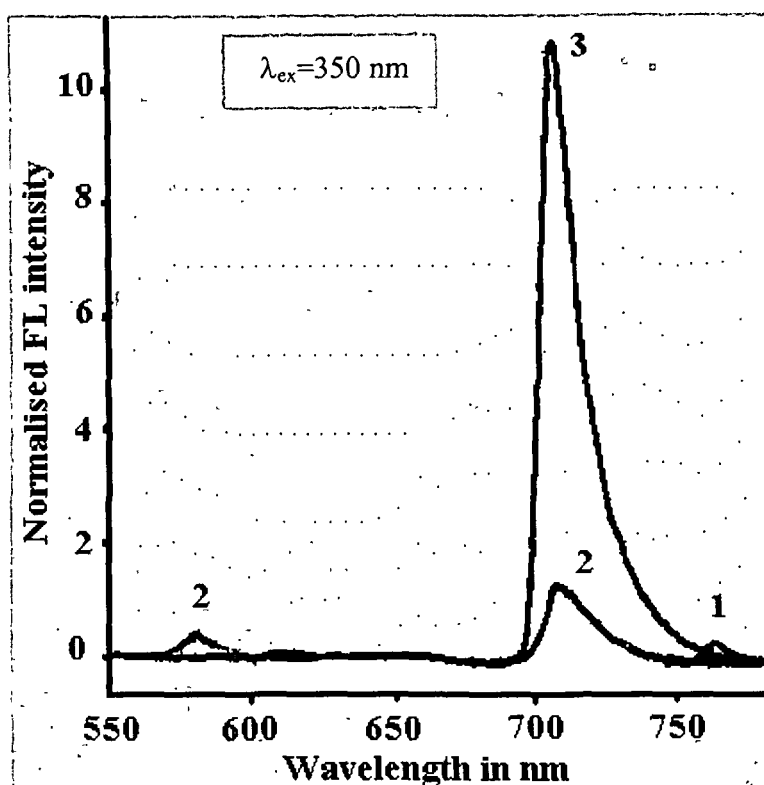


Figure 19. Fluorescence emission spectra of (1) PVOH matrix and (2) ZnS:Mn and (3) CdS quantum dots

function of wavelength or wavenumber. The FL excitation spectrum should, therefore, reproduce the absorption spectrum of the molecule. A fluorescence excitation spectrum is a more sensitive method of obtaining the absorption spectrum and is of great analytical value in systems containing a number of fluorescent species or a large background absorption.

Also, the quantum dot / quantum well structures fluoresce to substantial amounts. All fluorescence spectra consist of a single and

relatively narrow fluorescence band occurring close to the onset of absorption. The room temperature fluorescence quantum yields of 3 - 5 % have been encouraged temperature dependent stationary and time resolved fluorescence spectroscopy experiments. Besides nonradiative transitions, at least two kinetically distinguishable processes act as channels for the removal of excitation energy. The nature of these channels still remains unraveled [123].

The instrument model used for recording FL emission of quantum dots was F-2500 FL spectrophotometer and operated at excited wavelength $\lambda = 350$ nm. We have observed relatively weak fluorescence at around 763 nm corresponding to PVOH matrix (figure-19, peak 1). Next, ZnS quantum dots fluoresce at 707 nm, where as CdS quantum dots fluoresce strongly at around 706.5 nm possessing largest quantum yield of around 92%. We propose the fluorescence efficiency of the surface states to be higher than that of the band edge or excitonic emission in case of extremely small (~ 2 nm) CdS quantum dots. However, for ZnS:Mn quantum dots additional peak at around 582 nm is observed due to the presence of delocalized electrons of Mn, which is consistent to the reports of Bhargava and co-workers [124].



CHAPTER-4

**VIBRATIONAL FEATURES OF
EMBEDDED QUANTUM DOTS**

CHAPTER- 4

VIBRATIONAL FEATURES OF EMBEDDED QUANTUM DOTS

At room temperature, lattice vibrations are inherent to almost all solids. Quantized energy of lattice vibrations are termed as phonons. Normally, in a bulk system, two independent replica of phonon aggrissions are observed, namely acoustic phonons in the low frequency range and optical phonons in the high frequency range. Further, both type of phonons are divided into two broad categories transverse mode (T) and longitudinal (L) mode. Thus, the vibrational characteristics include:

1. Transverse acoustic (TA) mode
2. Transverse optic (TO) mode
3. Longitudinal acoustic (LA) mode
4. Longitudinal optic (LO) mode
5. Mixed modes and higher order modes

4.1 Electron-phonon coupling

The analysis of the interaction of electron-hole pairs with phonons starts with the investigation of the two main contributions arising from (i) the coupling to acoustic phonons by deformation potential or piezoelectric

interaction and (ii) the polar Frohlich coupling to optical phonons [125,126]. The Frohlich coupling scheme describes the coupling of the electric field created by the vibrations of the ionic nuclei with the Coulomb field of the optically excited e^-h^+ pairs. Due to the deformation potential, however, excitons couple to the longitudinal acoustic phonons. The compression and expansion changes the ion bond length, thus modulating the semiconductor band gap and the exciton energy.

One experimental approach to study the electron-hole pair phonon interaction is the analysis of resonant Raman scattering as well as the Stokes shift (Δ) between absorption and luminescence peaks. Qualitative discussions can be made in terms of Huang-Rhys parameter ' S ' [127], comparing the ratio between the zero phonon line and the corresponding higher phonon satellites. The approach is based on a simple phenomenological model resulting from the Franck-Condon* picture with the ground and the excited states being displaced harmonic oscillators. The line shape in absorption and luminescence, and the cross section of Raman scattering can be derived by calculating the overlap integral of the wave functions of the undisturbed and the displaced harmonic oscillators.

In absorption and luminescence according to Huang and Rhys, the optical phonons and their set of satellites give rise to a line shape of the spectra corresponding to

* Appendix-3

$$\alpha(\omega) = A \exp[-S(2\bar{n} + 1)] \times \sum_{p=-\infty}^{\infty} \left(\frac{\bar{n} + 1}{\bar{n}} \right)^{p/2} I_p \left(2S\sqrt{\bar{n}(\bar{n} + 1)} \right) \delta(E - E_x + S\hbar\omega_{LO} - p\hbar\omega_{LO}) \quad (39)$$

with \bar{n} the thermal average of the vibrational quantum number

$$n(T) = \frac{1}{\exp(\hbar\omega_{LO} / kT) - 1} \quad (40)$$

S is the so called Huang-Rhys factor, I the Bessel function of second kind, ω_{LO} the LO-phonon frequency and p the number of phonons taking part in the optical transitions. Equation-39 represents a series of equally spaced delta functions with the energy separation of the phonon energy values. At zero temperature the same equation corresponds to the Poisson's distribution $S^l e^{-S} / l!$. For $S < 1$, the maximum of the envelope over all phonon replica is situated near the zero-phonon line; in the case of $S > 1$, the phonon satellites are stronger in their intensity compared to the zero phonon line and the maximum of the envelope shifts to lower/higher frequency for phonon emission/absorption, respectively. The difference between the maximum of absorption and emission, the so called Stokes shift in the Franck – Condon model*, is given by

$$\Delta_{Stokes} = 2S\hbar\omega_{LO} \quad (41)$$

and the line broadening due to the phonon coupling is given by

* Appendix-3

$$\Delta_{FWHM} = \hbar\omega_{LO} 2S^{1/2} \quad (42)$$

In the Franck-Condon model the displacement δ of the minima of the two parabola describing the vibronic potentials and representing the degree of vibrational coupling, is related to the Huang-Rhys parameter [127,128]

$$S = \frac{\delta^2}{2} \quad (43)$$

The first theoretical and experimental investigation of the Huang-Rhys parameter S and, thus of the electron-phonon coupling strength in quantum dots has been given by Klein et al. [129] considering uncorrelated electrons and holes. Because of the lack of knowledge of the exact wave functions, the authors use a model charge distribution where only the electron is confined and the hole resides at the centre of the sphere. For such a charge distribution a size independence of the electron-phonon coupling has been derived from the calculation. Good agreement between the calculations and experimental results from resonant Raman scattering has been achieved when choosing the Huang-Rhys parameter in the order of $S \sim 0.5$. The exciton-LO phonon coupling in spherical quantum dots has also been treated theoretically by Nomura and Kobayashi [130]. They have considered contributions arising due to the non-parabolicity of the conduction band, the valence band mixing and Coulomb interaction. A non-monotonic size dependence of the exciton-phonon coupling has been obtained, which is closely related to the spatial

extension of the exciton wave function itself. It has been reported that for CdSe quantum dots, the coupling of the exciton to LO phonons has a minimum around $R = 7$ nm ($a_B = 5.6$ nm). It becomes stronger in the range $R < 7$ nm, mainly due to the confinement-induced mixing of hole wave functions. In the range $R > 7$ nm, the confinement is more influenced by the Coulomb interaction. From the point of theory it seems that theoretical predictions give values of S not exceeding 0.1-0.5, taking account spin-orbit interaction, finite potential wells, non-parabolicity and Coulomb interaction. S around (or larger) than unity could only be attained by introducing a strong charge separation artificially, for example, by an additional charge [130], by surface polarization [30,131], or by other effects breaking the spherical symmetry such as strain and lattice deformation. The predicted size-dependence of the coupling strength of electron-hole pairs to LO phonons differs considerably in the published results, both constancy, and increase and decrease with increasing confinement have been found.

As observed by resonant Raman studies, the LO-phonon frequencies in nanocrystallites (NCs) are essentially identical to those in bulk materials [132,133]. For CdSe, $\omega_{LO} = 210$ cm⁻¹ (27 meV) and for CdS $\omega_{LO} = 300$ cm⁻¹ (38 meV). We have measured the Δ_{Stokes} by measuring the absorption and emission peaks. The emission peaks remains almost same for all the samples. Referring to figure-18(A) &19 once again, the coupling constants could be determined (table-5). High coupling constants values are unique

in the embedded quantum dot systems, which signify probability of discretization of optical modes due to phonon confinement effects.

Table 5. Calculation of coupling strength in CdS/PVOH quantum dots

Absorption peak (from OAS) (eV)	Emission peak (from Lumin. spectra) (eV)	Difference $\Delta_{Stokes} = 2S\hbar\omega_{LO}$ (eV)	Coupl.strength (S)
2.658	1.764	0.894	11.76
2.630	1.764	0.866	11.39
2.541	1.764	0.777	10.22

4.2 Raman spectroscopy and surface optic phonons

Raman spectroscopy deals with the inelastic scattering of light from rigid spherical atomic sites. It is one of the best characterizing technique to study different vibrational modes in a given specimen. Similar to charge carrier confinement, phonons can also be confined within the particle [134,135]. Confinement of optical phonons lead to asymmetric and broadened line shapes [136], whereas confined acoustic phonons have frequencies which depend inversely upon the particle size and range from

a few cm^{-1} to a few tens of cm^{-1} [137,138]. Raman scattering from confined acoustic phonons can also be observed, and it can be used for determination of the particle size. Quantum dot size determination by low frequency inelastic scattering (LOFIS) have been reported in glass [134,139], aerogels [140] and in polymers [141]. Duval and co-workers have reported low frequency Raman bands in nucleated glass [139] and measured even the size of the particles consistent to x-ray diffraction and electron microscopy methods. The position of the low frequency Raman peaks was found as a function of the inverse of particle diameters [139]. An analysis of Raman peak intensity and polarization has inferred the existence of a spherical source of scattering. This observation together with the linear dependence of the Raman line shift from the inverse of nanocrystallite dimensions, suggested that vibrational *surface modes* (SO) of the particles are responsible for the observed Raman scattering [139]. Possible reason for the discrepancy between experiments and calculations might be the effect of particle shape. The deviation from spherical shape can cause changes in the vibrational frequency and Raman selection rules. Lines at low Raman shifts are attributed to localized acoustic vibrations.

Raman scattering measurements were performed at room temperature using 488 nm line of Ar ion laser in the backscattering configuration and recorded by a silicon CCD camera. The spectral resolution of the instrument was about 0.1 cm^{-1} . For the CdS particles, the

surrounding medium was initially air ($\epsilon_d = 1$) (CdS powder), then water ($\epsilon_d = 55.3$) (aqueous CdS) and for the rest it was PVOH ($\epsilon_d = 2$) (PVOH embedded CdS quantum dots). The laser power was adjusted to 20 mW in defocusing mode to avoid laser heating and coalescence of nanoparticles. The scattered intensities were analyzed using a double monochromator (SPEX, Inc) with a standard detection system.

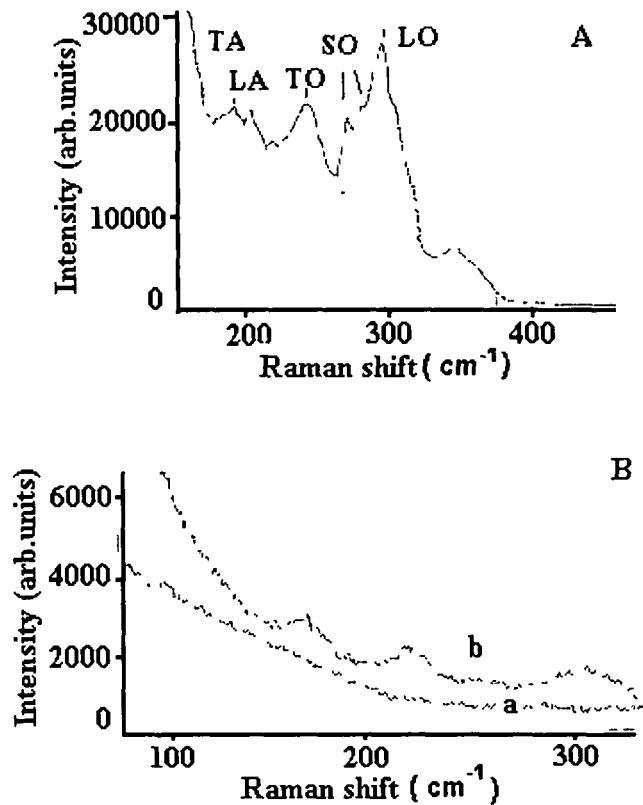


Figure 20 Raman spectra of CdS ultra-small particles (A) in air, (B)(b) in water and (a) response that of PVOH matrix

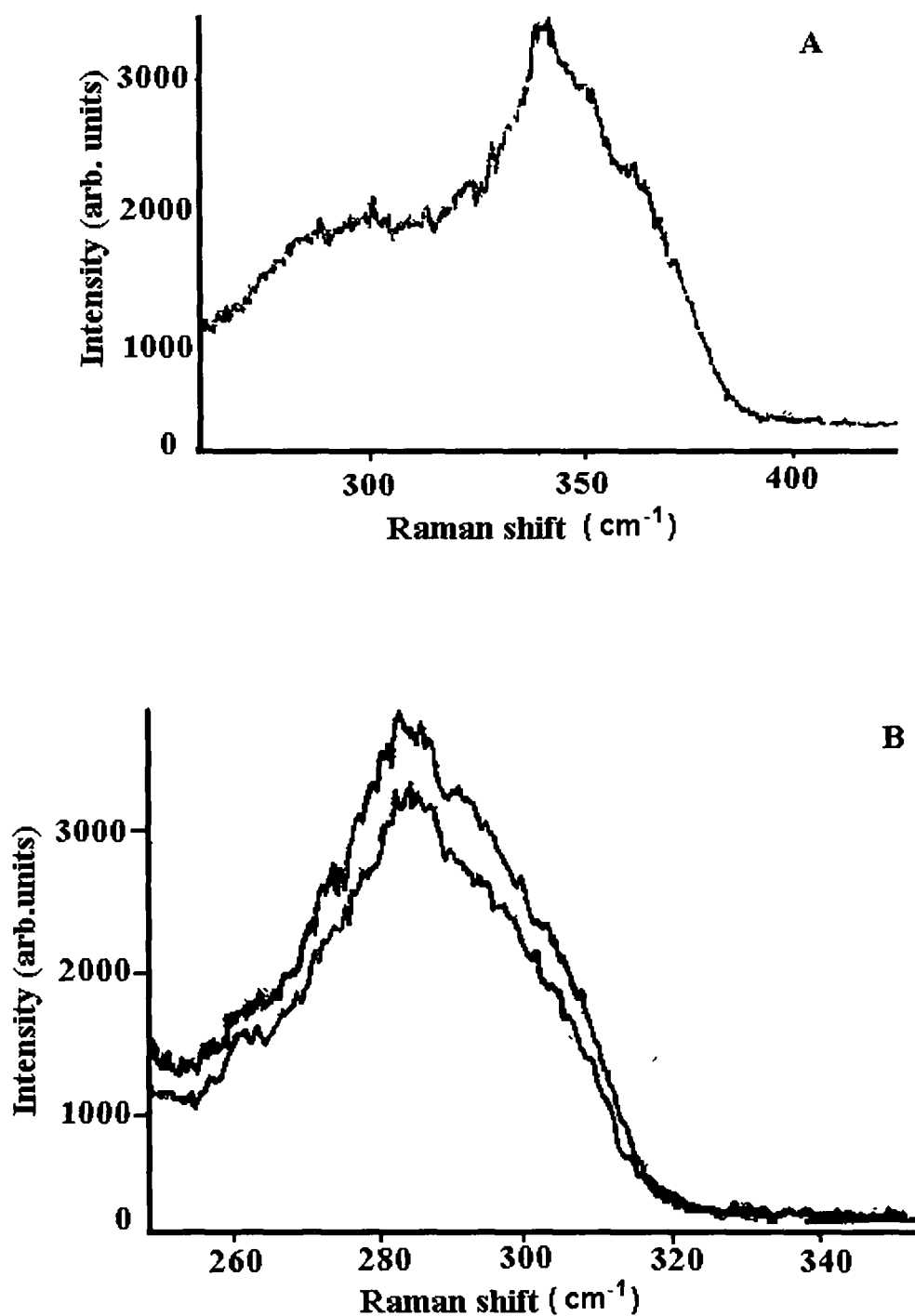


Figure 21 Resonant Raman spectra of CdS quantum dots with CdS PVOH (A) 1 15, (B) 1 4 prepared by direct treatment of H₂S

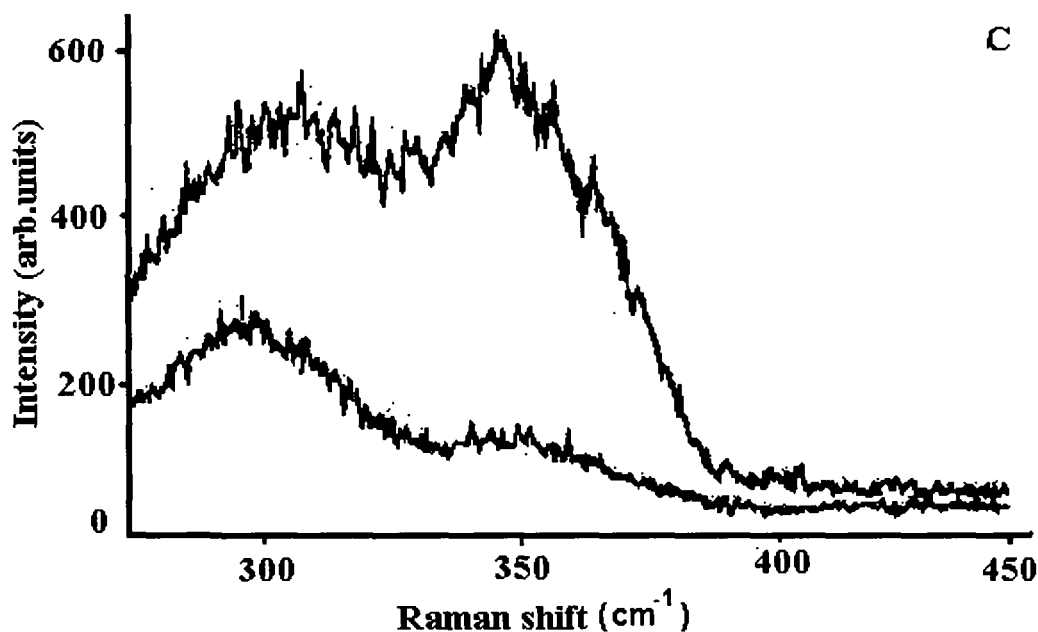


Figure 21. Resonant Raman spectra of CdS quantum dots with CdS:PVOH (C) 1:4 prepared by diffusion reaction of H₂S

As the surface to volume ratio is large for nanocrystallites, besides a characteristic first order longitudinal (1LO) phonon mode, surface optic phonon (SO) mode is expected in between LO and TO. Figure-20 depicts RR spectra of CdS nanoparticles in air, water embedded in PVOH. It was observed that in case of water, due to large dielectric constant differences SO phonon replicas are absent except presence of only LO and TO modes which are quite natural. Figure-21 represents response of LO and mixed modes due to direct treatment and diffusion treatment of H₂S (during synthesis). Also, effect of matrix concentration on RR spectral

response is illustrated in figure-22. As shown in figure-21, we have observed that LO mode shifts towards lower energy in case of direct treatment of H₂S (~ 282 cm⁻¹) with respect to diffusion treated H₂S (~ 300 cm⁻¹). A close look at figure-21(B)&(C) reveals that alongwith LO phonon replica LO+TA replica peaking around 348 cm⁻¹ for quantum dots

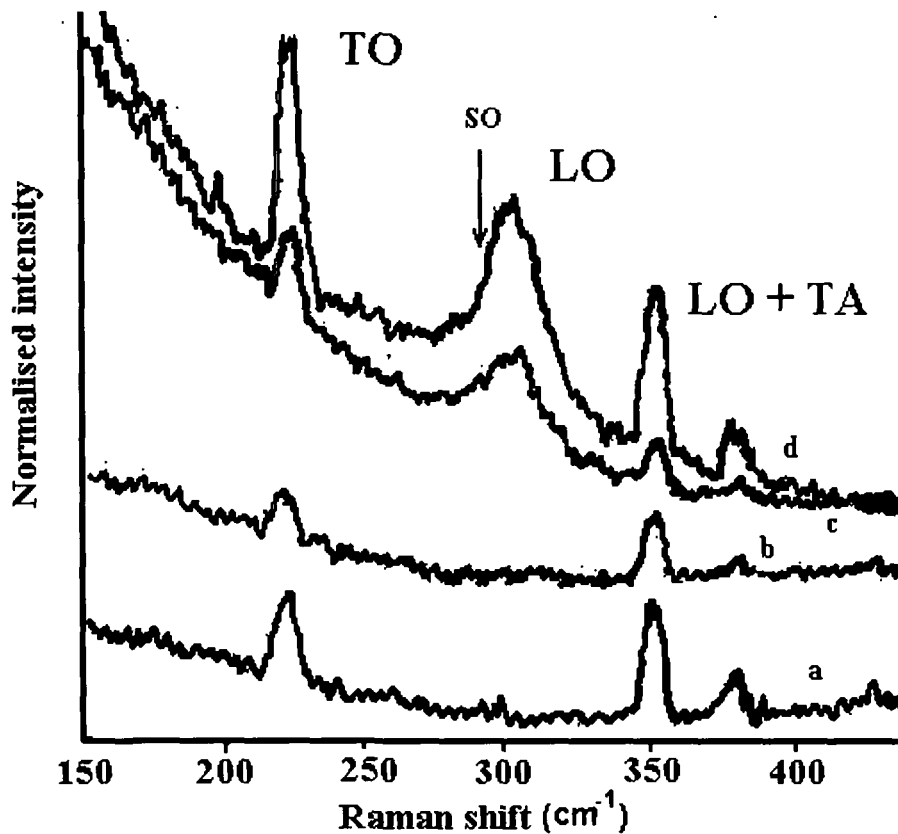


Figure 22. Resonant Raman spectra of (a) 6:1, (b)1:1, (c)1:3 and (d) 3:1 CdS/PVOH quantum dots

prepared by diffusion treatment of H₂S. The same event is not observable for the quantum dot sample prepared by direct reaction of H₂S. Figure-20 shows (CdS/air) characteristic first order phonon mode (1LO) at 296 cm⁻¹ ($\hbar\omega_l = 34$ meV) and a shoulder in the low frequency wing at around 282 cm⁻¹, identified as the surface optic phonon (SO) mode with characteristic TO mode observable at 242 cm⁻¹ ($\hbar\omega_l = 30$ meV). Similarly, for PVOH embedded CdS, we observe SO mode corresponding to a Raman shift ~ 272 cm⁻¹. The SO mode has already been reported in indirect gapped GaP semiconductor quantum dots [142], and is anticipated to be especially strong in highly polar materials when the electronic charge distribution is concentrated near the surface. The frequencies of SO modes are slightly smaller than those of the LO phonons. In the case of CdSe ($\omega_{LO} = 210$ cm⁻¹) for instance, they are in the range 194-200 cm⁻¹[129]. According to Klein et al. [129], the frequencies of the SO modes depend on the dielectric environment of the dots and is given by

$$\omega_l^2 = \frac{\omega_{TO}^2 \frac{l+1}{l} + \omega_{LO}^2 \frac{\epsilon_\infty}{\epsilon_d}}{\frac{l+1}{l} + \frac{\epsilon_\infty}{\epsilon_d}} \quad (44)$$

with $l = 1, 2, \dots$. Assuming air as the surrounding medium we obtain the lowest SO mode ($l = 1$) to occur at 282 cm⁻¹ after which the modes are indistinguishable due to extremely narrow energy differences between

successive modes. The evolution and validity of equation-44 is discussed in the succeeding section in macroscopic model of SO modes.

We have taken three medium for CdS quantum particles namely, air, water and polymer matrix (PVOH). The 1LO mode for CdS particles is observed at $\sim 300 \text{ cm}^{-1}$. The corresponding 1TO mode can be obtained using the Lyddane-Sachs-Teller relation [143]:

$$\frac{\omega_{LO}^2}{\omega_{TO}^2} = \frac{\epsilon_0}{\epsilon_\infty} \quad (45)$$

where $\epsilon_0 = 8.9$ and $\epsilon_\infty = 5.2$ are static and high frequency dielectric constants of CdS, respectively. Using respective values, the transverse mode 1TO is supposed to be observable at $\sim 230 \text{ cm}^{-1}$. The purpose of the chapter is to study the size and matrix dependent electron-phonon coupling for theoretical and experimental concerns and to explore surface optic modes, using resonant Raman scattering. We begin with a standard macroscopic model.

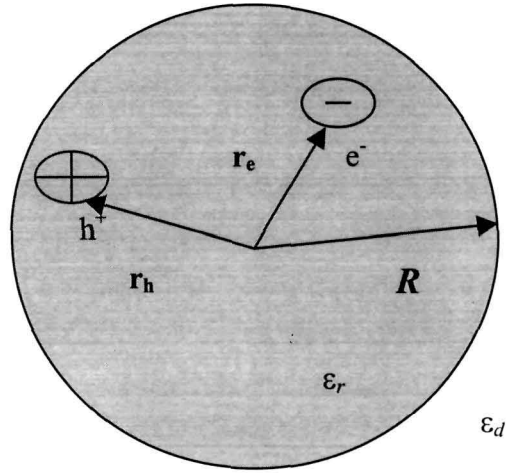


Figure 23. A spherical quantum dot having dielectric constant ϵ_r embedded in a matrix of dielectric constant ϵ_d

4.3 Macroscopic model of surface phonons

Referring to figure-23, we consider a semiconducting sphere of radius R and dielectric constant ϵ_r embedded in the surrounding medium of dielectric constant ϵ_d . We neglect any sorts of anisotropy in ϵ . We start with standard equations [144,145]:

$$\vec{D} = \epsilon \vec{E} = \vec{E} + 4\pi \vec{P} \quad (46)$$

$$\vec{E} = -\vec{\nabla} \phi \quad (47)$$

$$\vec{\nabla} \cdot \vec{D} = 0 \quad (48)$$

where \vec{D} , \vec{E} , \vec{P} and φ are the electric displacement, the electric field, the polarization density, and the electric potential respectively. From these, one finds

$$\varepsilon \nabla^2 \varphi = 0 \quad (49)$$

Now, we have two cases. Either $\varepsilon = 0$ or $\nabla \varphi = 0$.

CASE-1 $\varepsilon = 0$

The dielectric constant is given by:

$$\varepsilon(\omega) = \varepsilon_{\infty} \frac{\omega^2 - \omega_{LO}^2}{\omega^2 - \omega_{TO}^2} \quad (50)$$

where ε_{∞} is the high frequency dielectric constant at high frequency, and ω_{LO} and ω_{TO} are the LO and TO eigen frequencies related by equation-45. Therefore, the case $\varepsilon = 0$ corresponds to the internal LO modes of eigen frequency ω_{LO} . The eigen functions may be written in terms of orthonormal basis set in terms of spherical harmonics.

$$B_k j_l(kr) Y_l^m(\theta, \varphi); \quad (50^*)$$

where $j_l(kr)$ is the spherical Bessel function of order l and the Y_l^m are the spherical harmonics. The boundary conditions, continuity of φ and the normal component of D at the interface, imply in the case of the internal

LO phonons, that φ vanishes outside the sphere and on its surface. We then choose the k 's so that for each l, m

$$j_l(kR) = 0 \quad (51)$$

These k 's, which depend on l , are then equal to

$$k = \frac{\alpha_{n,l}}{R} \quad (52)$$

where $\alpha_{n,l}$ is the n^{th} zero of the spherical Bessel function of order l . The true quantum numbers are the n, l, m , but for simplicity we will use the notation l, m, k . Choosing condition (51), the normalization constant B_k is given by

$$B_k^{-2} = \left(\frac{R^3}{2} \right) j_{l+1}^2(kR) \quad (53)$$

for $l = 0$, this implies

$$B_k^{-2} = \frac{2k^2}{R}, \quad (54)$$

with $k = n\pi / R$ ($n = 1, 2, 3, \dots$). We then have the expression of φ for LO modes and, as the relative displacement $\mathbf{u} = \mathbf{u}_+ - \mathbf{u}_-$ of an ionic pair is proportional to \vec{P} and \vec{E} and is proportional to the gradient of φ . Of course, to get physically meaningful results, the quantum numbers must not be too large to account for the finite size of the crystal unit cell.

CASE-2 $\nabla\varphi = 0$

This will give us surface or SO modes. The possible solutions are such that

$$\varphi(r) = A_{l,m} r^l Y_l^m(\theta, \varphi) \quad \text{for } r < R \quad (55)$$

$$\varphi(r) = B_{l,m} r^{-l-1} Y_l^m(\theta, \varphi) \quad \text{for } r > R \quad (55^*)$$

The boundary conditions then imply

$$\varepsilon = -(l + 1/l) \varepsilon_d \quad (56)$$

with $l = 1, 2, 3, \dots$. For a given couple (l, m) we have several (as many as R allows) LO modes and only one SO mode. For this mode, once again, u is proportional to the gradient of φ . The eigen frequencies ω_l must satisfy equation-50.

Using equations-45, 50 & 56 various surface modes (ω_l) of CdS nanoparticles embedded in PVOH ($\varepsilon_d = 1.95$) matrix are determined (table-6). Also, for the sake of comparison, ω_l values are calculated both for nanometric CdS powder samples (air, $\varepsilon_d = 1$) and aqueous CdS samples (water, $\varepsilon_d = 55.3$).

Table 6. Raman shift of various surface modes

SO Modes	CdS/air (cm ⁻¹)	($\omega_{i+1}-\omega_i$) (cm ⁻¹)	CdS/water (cm ⁻¹)	($\omega_{i+1}-\omega_i$) (cm ⁻¹)	CdS/PVOH (cm ⁻¹)	($\omega_{i+1}-\omega_i$) (cm ⁻¹)
ω_1	278.33	-	229.57	-	268.27	-
ω_2	281.84	3.51	230.68	1.11	272.89	4.62
ω_3	283.15	1.31	231.23	0.55	274.71	1.82
ω_4	283.79	0.64	231.54	0.31	275.62	0.91
ω_5	284.19	0.30	231.75	0.21	276.20	0.58
ω_6	284.44	0.25	231.89	0.14	276.55	0.35
ω_∞	285.87	-	232.79	-	278.67	-

Keeping in mind the above theoretical findings, we have tried to correlate with the experimental data points.

It has been observed that for 3:1 and 1:3 ratio samples LO modes are asymmetrically broadened (figure-22). The asymmetry corresponds to the existence of SO modes in the low frequency wing of LO modes [146]. Interestingly, we notice for 1:1 and 6:1 ratios neither SO nor LO modes exist. We believe in 6:1 sample smearing out of LO modes may be due to

the fact that interaction of photons with the densely packed CdS particles are unable to excite optical phonons. On the other hand, we do not know why LO modes are absent even for 1:1 sample. As we are interested in the investigation of SO modes, we must deal with the asymmetry regime of the 3:1 and 1:3 spectra, where LO peaks are well resolved.

The top two spectra of figure-22 (c)&(d) were analyzed by a novel computing technique*. In this technique the picture is first digitized using standard software MATLAB®. The output data then analyzed using Microsoft spread sheet programs. A few data points are represented in table-7.

Table 7. Digitized data points of Raman spectra of CdS/PVOH quantum dots Pho1(3:1) and Pho2(1:3)

Raman Shift (cm ⁻¹)	d(Intensity) / d(Raman shift)	
	Pho1	Pho2
268.471338	-0.0056884	-0.0038622
269.426752	-0.0037923	-0.0019311
270.382166	0.00189614	0
271.33758	0	-0.0019311
272.292994	-0.0018961	0
273.248408	0	0.00193112
274.203822	0	0
275.159236	-0.0018961	0
276.11465	0	-0.0019311
277.070064	0.00189614	0
278.025478	0.00189614	0.00193112
278.980892	0.00379227	0
279.936306	0.00379227	0
280.89172	0.00189614	0
281.847134	0.00568841	0

Appendix-2

282.802548	0.00568841	-0.0019311
283.757962	0	-0.0019311
284.713376	0	0
285.66879	0	0.00193112
286.624204	0	0.00193112
287.579618	0	0.00193112
288.535032	0	0.00193112
289.490446	0.00379227	0.00386224
290.44586	0.00568841	0.00386224
291.401274	0.01327295	0
292.356688	0.01516908	0.00579336
293.312102	0.00568841	0.00579336
294.267516	0.00568841	0.00193112
295.22293	0.02085749	0
296.178344	0.02275362	-0.0019311
297.133758	0.01137681	0.00386224
298.089172	0.01896135	0.0096556
299.044586	0.02275362	0.00772448
300	0.00568841	0.00193112
300.955414	0	0.00386224
301.910828	0.00568841	0.00386224
302.866242	0.00189614	0.00193112
303.821656	0	0.00193112
304.77707	0.00379227	0
305.732484	0.00758454	-0.0019311
306.687898	0.00379227	0.00193112
307.643312	-0.0018961	0.00579336
308.598726	-0.0189614	0.00386224
309.55414	-0.0227536	0.00193112
310.509554	-0.0075845	-0.0038622
311.464968	-0.0056884	-0.0077245
312.420382	-0.0037923	-0.0096556

To obtain a clear contrast of the two digitized spectra, we have made plots of the first derivative of Raman Intensity vs Raman shift (figure-24(a)). The expected surface modes are to exist in the low frequency regime and so we have magnified the same response in figure-24(b). Corresponding to each surface mode there should be comparatively large values of first derivatives. The various SO modes, experimentally observed so far are given in table-8.

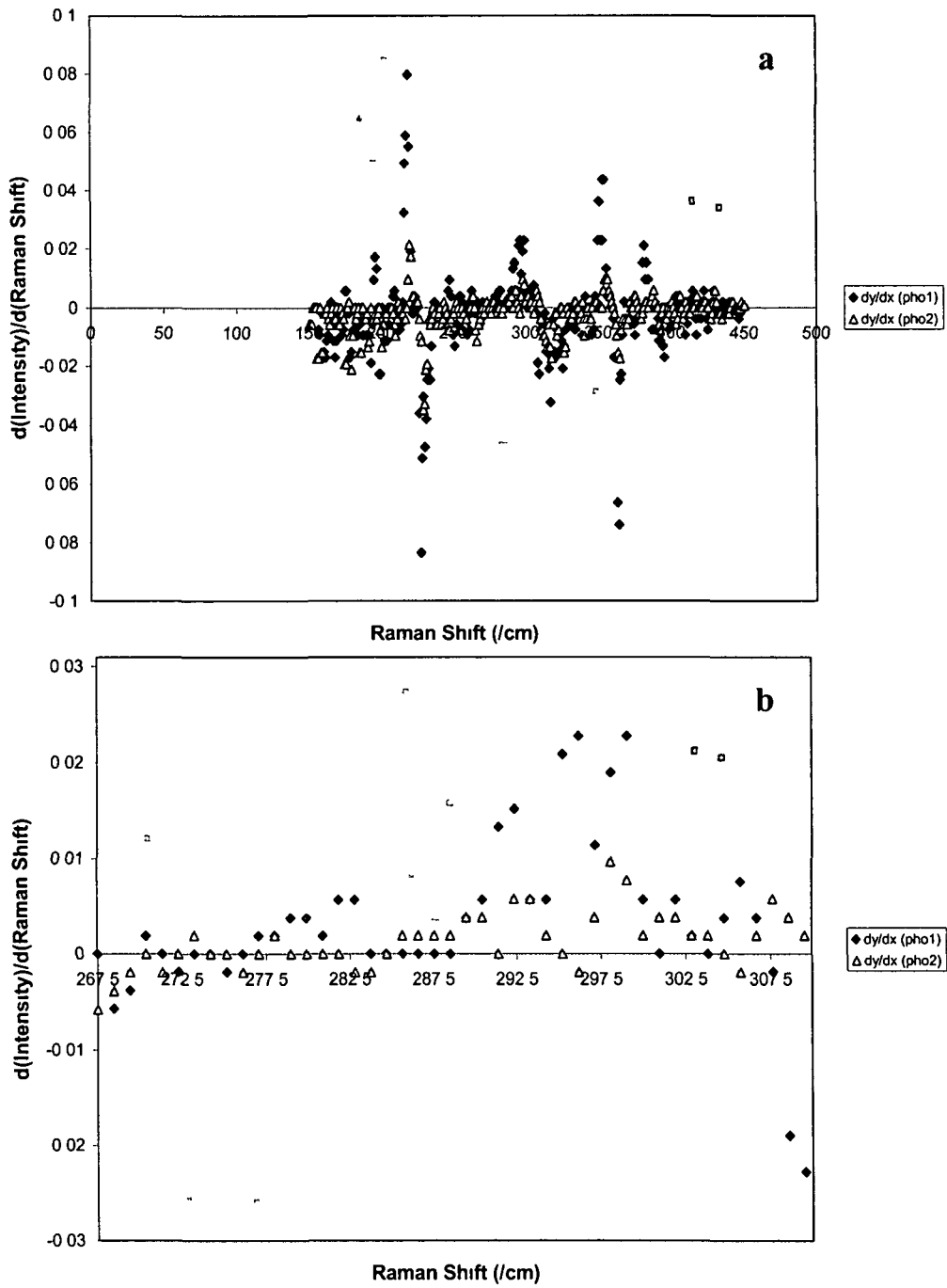


Figure 24 First derivative of Raman intensity with Raman shift for (a) Pho1 (3 1) and Pho2 (1 3) CdS quantum dots (b) response within 267- 308 cm^{-1}

Table 8. Correlation of SO modes: Theoretical and Experimental

Surface modes (ω)	Experiment				Theory (from tab-6)
	Pho1(3:1)	($\Delta\omega = \omega_{i+1} - \omega_i$)	Pho2(1:3)	($\Delta\omega = \omega_{i+1} - \omega_i$)	($\Delta\omega = \omega_{i+1} - \omega_i$)
ω_1	270.38	-	273.25	-	
ω_2	277.07	6.69	278.025	4.775	4.62
ω_3	278.025	7.645	285.67	12.42	6.44
ω_4	278.98	8.6	286.62	13.37	7.31
ω_5	279.94	9.56	287.58	14.33	7.93
ω_6	280.89	10.51	288.535	15.285	8.28
ω_∞	282.32	11.94	290.46	17.21	10.4

Referring to figure-24 and table-8, we predict various SO modes exist in successions both for sample Pho1(3:1) and Pho2(1:3). The points are obtained by considering the point where first derivative changes abruptly. Note that these modes detected so far experimentally, are in close proximity with the theoretical obtained values. The maximum available spacing for the existence of SO modes for 3:1 and 1:3 samples are found to be 11.94 cm^{-1} and 17.21 cm^{-1} , whereas theory predicts to an amount of 10.4 cm^{-1} .

Moreover, for the respective samples (Pho1 and Pho2) we expect LO modes at 296.18 (and 299.045 cm^{-1}) and 298.09 cm^{-1} respectively which are point of maximum change corresponding to longitudinal oscillations. Bimodal behaviour of the first sample guarantees confinement of LO modes. The second sample (1:3) did not provide adequate CdS particles to detect all possible modes.

Thus, we claim SO modes could be visible when a suitable matrix with appropriate stoichiometry is chosen. In our case the molar ratio of CdS to PVOH is 3:1. We have computed possible series of surface modes with respect to different matrices. Next, using equation-45 we that found that in case of water, the SO modes are absent because their energy corresponds to the energy of TO modes. Moreover, the discrete modes which exist as a result of finite energy spacings claim confinement of surface optic phonons in the embedded quantum dot systems.



CHAPTER-5

**ION IRRADIATION EXPERIMENT AND
MODIFIED BEHAVIOUR OF QUANTUM DOTS**

CHAPTER-5

SWIFT HEAVY ION IRRADIATION MODIFIED BEHAVIOUR OF QUANTUM DOTS

For years, swift heavy ion (SHI) beams have been used especially for fabrication and ion induced modification in material properties. In this unit, we have investigated SHI induced modified properties of the quantum dots. Prior to discussion of experimental results, we shall review in brief the ion-matter interaction processes.

5.1 Ion-matter interaction

When a swift heavy ion passes through a material, the free electrons available in its path gets excited within a time scale $\sim 10^{-15}$ sec. This electronic excitation leads to rise in temperature of the ion's track known as electronic temperature* which is of the order of 10^5 °K. Next, the energy is relaxed into lattice and so phonons get excited within a time frame of 10^{-12} sec. giving rise to lattice temperature rise of the order of 10^3 °K. Then, the energy of the ion is quickly transferred into other parts of the specimen. Due to fast quenching the ion path melts and one gets amorphized zone (very often, termed as *ion track* in the literature). The example of amorphization can be understood as the effect when a red hot piece of iron is suddenly dropped into a cold water reservoir. In fact, when

* Appendix-4

an energetic ion passes through the material it suffers two kinds of energy loss. First, nuclear energy loss ($S_n = (dE/dx)_n$) which is due to the interaction between the ion and the nuclei which is predominant for the ions carrying low energy value (KeV). Second, when energy increases it is the electronic energy loss ($S_e = (dE/dx)_e$) that comes into picture which significantly dominates over S_n for the beams in MeV range. S_{eth} is the threshold energy of ions below which only point defects are expected [147,148]. Ion tracks are found only for the cases when electronic energy loss (S_e) exceeds the threshold energy (S_{eth}) value.

5.2 Our quantum dot systems

Our specimens are unique and novel in the sense that the quantum dots / nanoparticles are embedded into the polymer host and therefore, only grain characteristics would be focus area of study under ion irradiation. Conventional nanostructured films suffer from grain boundary problems, which are the sources of weak link resistivity. However, the problem is avoided by embedding nanoparticles into a suitable polymer matrix. Because, the quantum dots / nanoparticles are separated each other by finite distances (interparticle separation more than the size of the quantum dots) and thus, ion bombardment study in these novel systems promise to be exciting area of study to understand better the ion-matter interaction in terms of well known models e.g. *a) thermal spike model and b) coulomb explosion model* [149-151].

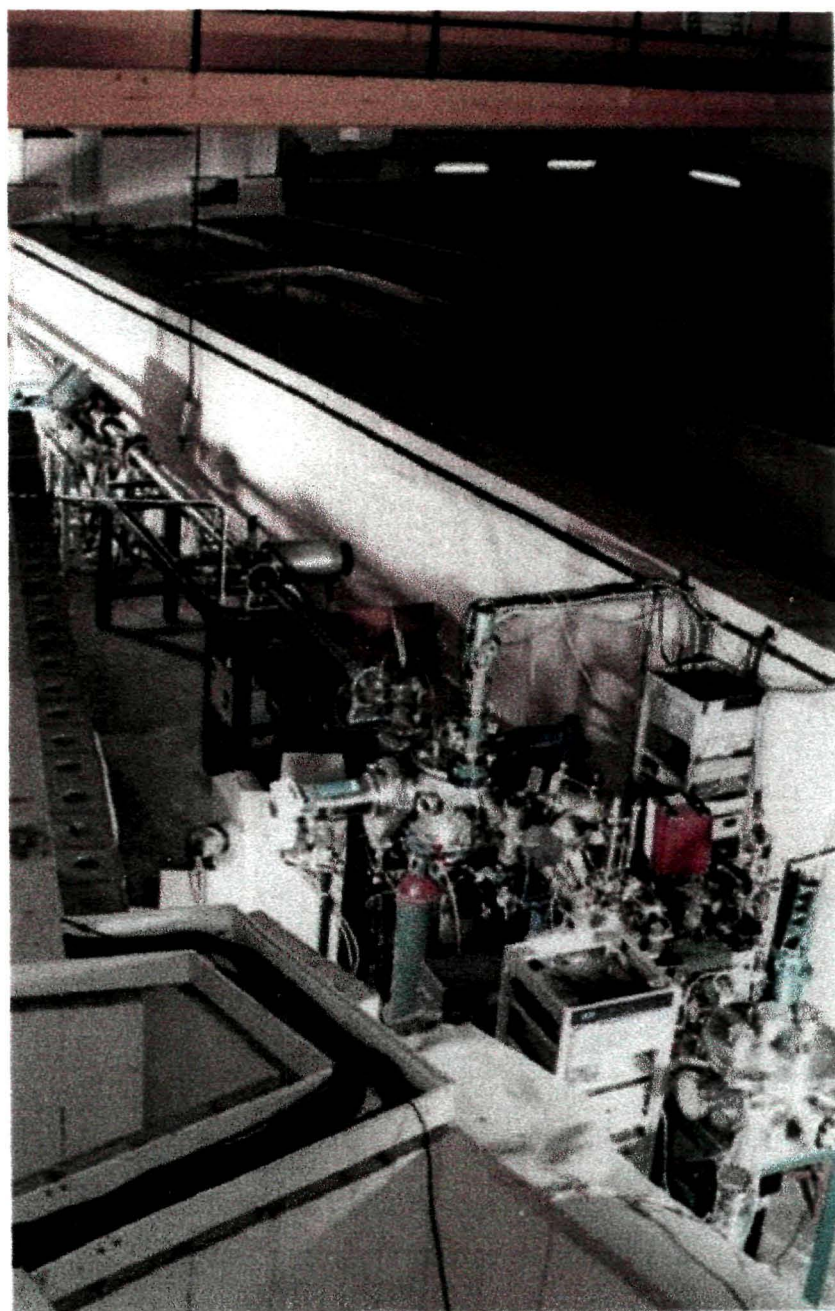
For $S_e < S_{eth}$ point defects are created which segregates into grain boundaries [148]. A fast ion produces ~ 5 nm track for $S_e > S_{eth}$ in polymers [152]. So, now if the ion finds a few embedded nanoparticles, either or combination of the following possibilities would be guaranteed.

- * Fragmentation into still smaller nanoparticles
- * Amorphization of the nanocrystallites
- * Simple evaporation
- * Melting into bigger crystallites
- * No effect (as if un-irradiated sample)

The advantage of preparing quantum dots in the polymer is manifold. First, due to the presence of large carbon cages and ligands, which alter in size with concentration, pH, temperature and stirring atmosphere, one can grow size controlled nanoparticles in the polymer. Second, as most of the polymer are dense viscous fluids, making a thin film out of it is relatively easier for characterization purpose. Third, in case of conjugated polymers delocalized electrons may participate in the transport properties.

5.3 The irradiation experiment

The irradiation experiment was carried out on each of four identical II-VI (CdS, ZnO, ZnS etc.) quantum dot samples. The samples were mounted on a vacuum shielded vertical sliding ladder having four rectangular faces. They were irradiated in the Materials Science chamber under high vacuum ($\sim 4.6 \times 10^{-6}$ Torr) by using the 100 MeV ^{35}Cl ion beam with an approximate beam current of 1.0 pA (particle nano-ampere), available from the 15UD tandem pelletron accelerator at NSC*, New Delhi, India [153,154]. The ion beam fluence was measured by integrating the ion charge on the sample ladder, which was insulated from the chamber. The fluence was varied in the range 10^{11} - 10^{13} ions/cm². In order to expose the whole target area, the beam was scanned in the x-y plane over the sample. The projectile range of the incident ion, as estimated by SRIM program [155] was found to be more than the thickness of each of the sample films. The ion beam energy and the thickness of the target was so chosen that only modification due to the electronic energy loss (S_e) affects the exposed sample. The ion beam induced effect was analyzed in terms of absorption spectra obtained by using UV-visible spectrophotometer, operated at low photon count rate to give all the natural peaks. Alongwith the absorption spectra, HRTEM, HRSEM, fluorescence and photoluminescence studies were carried out for irradiated quantum dots with respect to un-irradiated pristine samples.



MATERIALS SCIENCE BEAM LINE

FIGURE 25

**Ion irradiation beam hall of Material Science beam line in
Nuclear Science Centre, New-Delhi-110 067, India**

5.3.1 Ion induced effect of hydroxyl-free ZnO semiconductor quantum dots

Fabrication details of oxide semiconductor nanoparticle systems (e.g. ZnO, CdO etc.) in the presence of reaction byproducts, unreacted species and dispersing media already exist in the literature [68,156-160]. As discussed in chapter-2, we have obtained hydroxyl-free ZnO quantum dots by adopting a quenching technique. The samples thus prepared were chosen for the irradiation experiment. 100-MeV chlorine ion was selected for the irradiation experiment with fluences 1×10^{11} , 5×10^{11} , 5×10^{12} and 1×10^{13} ions/cm². Recently, swift heavy ion irradiation induced grain splitting and even disappearance of nanometric grains of SnO₂ powder was reported by Berthelot et al [161]. Their observation of the fragmentation of larger grains into smaller ones in particular has been explained by thermal spike induced internal pressure inside the grains.

ZnO is a direct band gap semiconductor with bulk band gap 3.35 eV at 300⁰K. So, bulk ZnO has got an absorption threshold corresponding to $\lambda = 371$ nm. It is well known that when the electron has a small effective mass and the material dielectric constant is large, the mean distance of the electron from the trapping center (ionized donor or hole) is large. In otherwords, orbital frequency of the e^-h^+ pair about their center of mass will be slower than (or, approximately equal to) the frequency of the lattice vibrations. Then, the appropriate value to be considered is static dielectric constant i.e; ϵ_0 . If the corresponding

behaviour of our representative ZnO nanomaterial system, could be accounted for by effective mass approximation (EMA model) [94], then experimental redshifts with ion fluences must satisfy well even for the determination of the average quantum dot size. The EMA with static dielectric constant is used to calculate a scaled binding energy:

$$E_b = E_{RY} \left(\frac{m^*}{\epsilon_0^2 m_e} \right) \quad (57)$$

where E_{RY} is the Rydberg energy (13.6 eV) in the hydrogen atom model. Now for ZnO; $m^* = 0.27 m_e$ and $\epsilon_0 = 8.5$ and so, $E_b \sim 51 \text{ meV} < 100 \text{ meV}$. Therefore, the combination of a small effective mass and large dielectric constant makes the EMA relevant subject to the consideration of the static dielectric constant [162]. A simple expression for the change in the band gap energy when an un-correlated e^-h^+ pair being generated is given by [163]

$$\Delta E = \frac{\hbar^2 \pi^2}{2R^2} \left(\frac{1}{m_e^*} + \frac{1}{m_h^*} \right) - 1.786 \left(\frac{e^2}{\epsilon R} \right) + pol. \quad (58)$$

where R is the average radius of the quantum dots, m^* being the respective effective masses for electron and hole, ϵ is the dielectric constant, and $pol.$ represents polarization terms. This approach generally predicts an increase in the band gap energy with decreasing particle size. The plot of ΔE vs R in case of ZnO nanoparticle system is shown in figure-26. The average size of the irradiated quantum dots was estimated using the same plot (table-9).

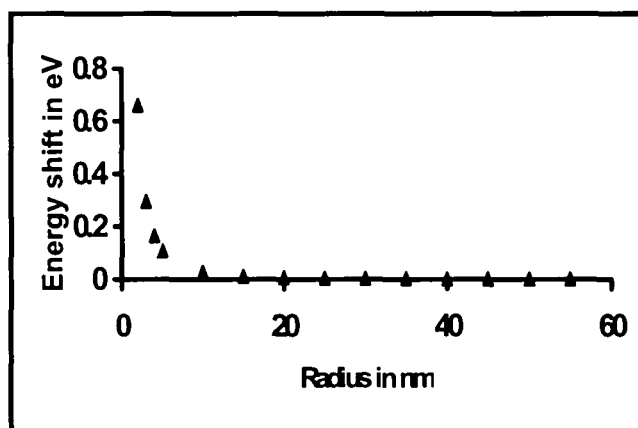


Figure 26. Energy shift vs size of the nanoparticles in ZnO system

Table 9. Energy shift and size effect due to ion fluence variations

Irradiation fluence (ions/cm ²)	Absorption edge (nm)	Band gap energy	ΔE energy-shift	R (nm)
Bulk	371	3.350	0	-
0	260	4.770	1.420	1.3
1x10 ¹¹	285	4.361	1.011	1.8
5x10 ¹¹	315	3.945	0.595	2.3
5x10 ¹²	335	3.710	0.360	4.0
1x10 ¹³	370	3.359	0.009	50.0

In fact, chlorine ion was selected for irradiation for two specific reasons. First, this was to introduce bleaching action upon any unwanted species if any attached to the ZnO quantum dots to obtain extra-pure ZnO quantum particles. This enables off-line characterizations to deal with

information obtained only from extra-pure ZnO quantum dots. Second, as our ZnO quantum dots are embedded in the PVOH polymer matrices and polymer easily gets amorphized through evolution of ion tracks even at low ion energies, hence a light ion like oxygen/chlorine would be preferable to notice appreciable irradiation induced effects upon the embedded nanoparticles.

The electronic stopping power of the chlorine beam (S_e), found from SRIM program [155] is about 553 eV/A^0 . The irradiation leads to the energy deposition at four different fluences without implantation of swift chlorine ions into the quantum dot samples.

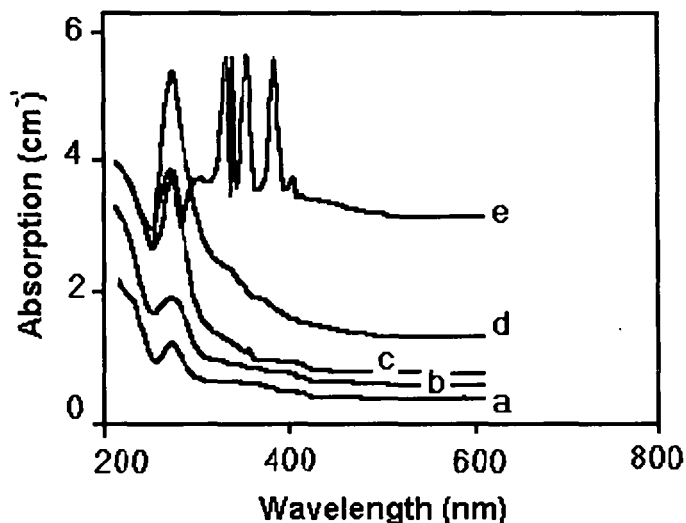


Figure 27. OAS of (a) virgin and irradiated (b) 10^{11} (c) 5×10^{11} (d) 5×10^{12} (e) 10^{13} ions/cm² ZnO semiconductor quantum dots

UV-visible spectroscopy, which provides useful information regarding optical band-gap is being treated as an important tool for material investigations. The optical absorption spectra of virgin and irradiated ZnO quantum dot samples are shown in figure-27. For the un-irradiated sample, free exciton absorption at around ~ 260 nm was noticed. The excitonic peak becomes pronounced and sharper upto the threshold fluence i.e., 5×10^{12} ions/cm² while in the spectrum of second dose, nearby band was seen around the main peak which is possibly due to the second exciton creation corresponding to the same $n = 1$ level. While for the third dose, in addition to $n = 1$; $n = 2$ excitonic absorption was noticed which was not observable in case of virgin sample. Again, band edge was found to be shifted strongly towards red illustrating the fact that ion bombardment leads to modification of quantum particle behaviour. The possible cause may be due to C-C bond breakage of the polymer. Fast ion beam melts the quantum particles and rapid quenching leads to aggregation into bigger clusters within a time scale of about 10^{-12} sec. But, it is reasonable to say after a close look at the absorption plot that the nature of particle aggregation depends strongly upon ion fluence as we had observed long tailing with increasing fluences. Obviously, long tailing was due to large inhomogeneity of nanoparticles with respect to virgin sample. Therefore, nanoparticles have not actually been damaged but they were modified in size and in structure under ion irradiation as

revealed from HRTEM depicted in figure-28. Beyond threshold fluence, polymer was supposed to be amorphized completely. The quantum particles thus lose their support in the polymeric matrix and they coalesce into bigger clusters. At the highest fluence, the larger sized quantum dots (~ 50 nm calculated by using EMA) behave as free-standing particles. We thus observe growth of nanoparticles under energetic ion irradiation, whereas Berthelot et al [161] have seen particle fragmentation.

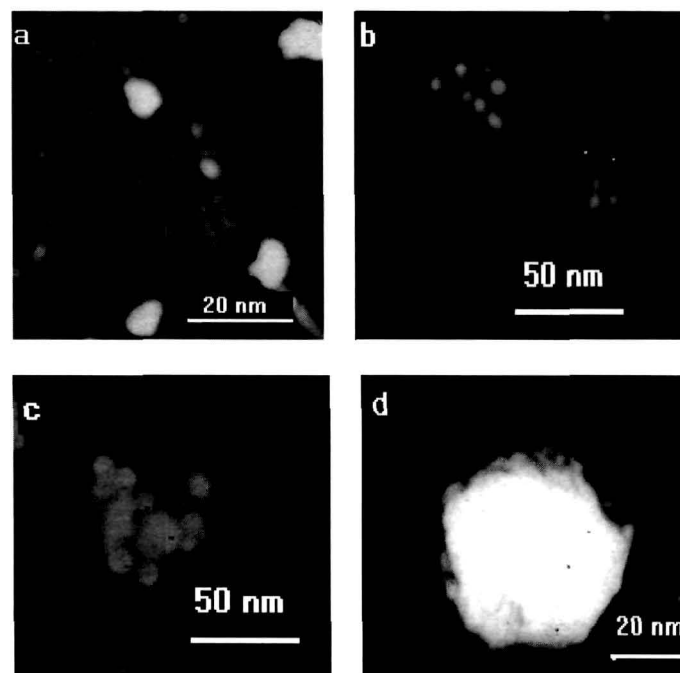


Figure 28. HRTEM images of (a) pristine and ion exposed (b) 1×10^{11} (c) 5×10^{11} (d) 5×10^{12} (e) 10^{13} ions- cm^{-2} ZnO semiconductor quantum dots

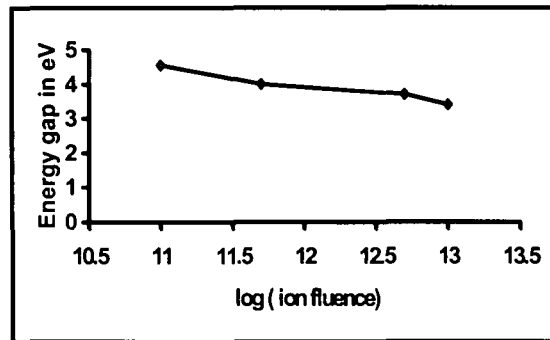


Figure 29. Energy gap response to log of ion fluence variation

Though both the effects are produced due to the electronic energy loss of the SHI in the medium, the details of the microstructure and actual energy deposited by the ions differ in both the cases. Another interesting feature observed in the spectrum of highest dose (1×10^{13} ions/cm²) selected so far, was an unexpected signature of free carrier excitonic absorption corresponding to $n \geq 2$ levels (figure-27). The other in between subsidiary peaks are due to the excitons bound to the neutral donors. If the excitons collide with impurities such as donors or acceptors, they are bound to them and afterwards are annihilated exhibiting luminescence. The logarithmic response of the energy gap with ion fluence being depicted in figure-29. The negative slope representing suppression of energy-gap parameter of ion exposed quantum dots with respect to un-irradiated one.

Thus, although EMA is still considered not fully adequate to describe energy-shift as a function of size for various semiconductors, with proper justification we have fitted it for measuring ZnO quantum dot

size after ion irradiation study. The result agrees well with HRTEM observation. The optical absorption study shows redshift of the onset with respect to virgin. Next, the evolution of free exciton absorption to higher levels ($n \geq 2$) are suggested for the ion dose beyond critical value. The highest dose shows pure ZnO behaviour of which size estimated to be ~ 50 nm in consistency with the transmission electron micrographs.

5.3.2 Grain growth and grain fragmentation : Effect of polymer hosts upon embedded CdS quantum dots

Bulk CdS has a direct band gap of 2.405 eV at room temperature. To improve electronic and optical properties, energy gap is tuned with the selective size of the material known as size quantization [164-166]. In order to optimize electronic, magnetic, spectroscopic and structural properties it is important to obtain details of individual quantum grains rather than an assembly of grains. To avoid severe problems e.g., the problem of weak link resistivity due to the presence of high density grain boundaries in nanostructured films, we have synthesized quantum dots / nanoparticles embedded in dielectric matrices of different physical properties. The quantum dots were grown in two variety of polymer matrices namely, polyvinyl alcohol (PVOH) and carboxylated styrene butadiene rubber (SBR) latex which are already discussed in chapter-2. They were irradiated with 100 MeV chlorine beam with fluences 1×10^{11} , 5×10^{11} , 5×10^{12} and 1×10^{13} ions/cm². Melting of quantum dots has been

observed in case of CdS powder and PVOH embedded CdS quantum dot samples while grain bursting predominates in CdS/SBR system as revealed from high resolution electron microscopic images. The mechanism of grain growth and grain fragmentation has been illustrated with experimental results.

While traversing through matter, SHI loses its energy in two ways. They are nuclear energy loss (S_n) due to elastic collisions with atoms of the solids and electronic energy loss (S_e) due to inelastic collisions of the electrons with the projectile ion. Ion implantation, cluster assembled nanoparticle formation etc. are governed by S_n for KeV energetic ions [66,69,167]. The latter process involves MeV energies and is used for introducing nanoscale defects and studying surface modification [168,169]. Although the appearance of track effects in polymers is known since some decades [152], there is hardly any report available describing ion-matter interaction for chemically synthesized polymer embedded semiconducting quantum dots. Synthesis of PVOH embedded CdS nanoparticles by gas-aerosol reactive electrostatic deposition technique has been explained by Salata et al [170]. The electronic and nuclear energy losses alongwith stopping ranges are shown in table-10.

Table 10.

Electronic energy loss (S_e), nuclear energy loss (S_n) and stopping ranges of Cl ion

Projectile energy (E) (MeV)	$S_e=(dE/dx)_e$ (eV/A ⁰)	$S_n=(dE/dx)_n$ (eV/A ⁰)	Stopping range (μm)
10 ⁻²	12.24	48.59	10.8x10 ⁻³
10 ⁻¹	36.12	48.15	77.2x10 ⁻³
1.0	126.7	18.72	71.1x10 ⁻²
10	485.0	3.77	32.3x10 ⁻¹
100	537.2	0.57	18.45

Two existing models viz., Coulomb explosion or ion spike model [149] and the thermal spike model [151] are well supported by a number of reports [172-175]. From table-10 it is clear that for 100 MeV beams, the thickness of the samples corresponding to PVOH and SBR matrices are (for our case, 6.2 μm and 1.0 μm) well below the projectile ranges (for physical properties see table-2, chapter-2). The chamber pressure during irradiation was 5×10^{-6} mbar maintained by a diffusion pump to avoid hydrocarbon contamination during ion irradiation.

5.3.2.1 Grain growth effect

Irradiation leads to narrow size distribution of particles by allowing minimum sized nanoparticles to melt and fast quenching results in average-sized particles in the sample. With increase in fluence, average diameter increases until complete amorphization of the polymer. The particles become freestanding and under heavy dose, some of them

coalesce into bigger sized grains and some split into smaller grains. Of course, the nature of coalesce or splitting solely depend upon relative positions of the quantum grains and point of ion impact.

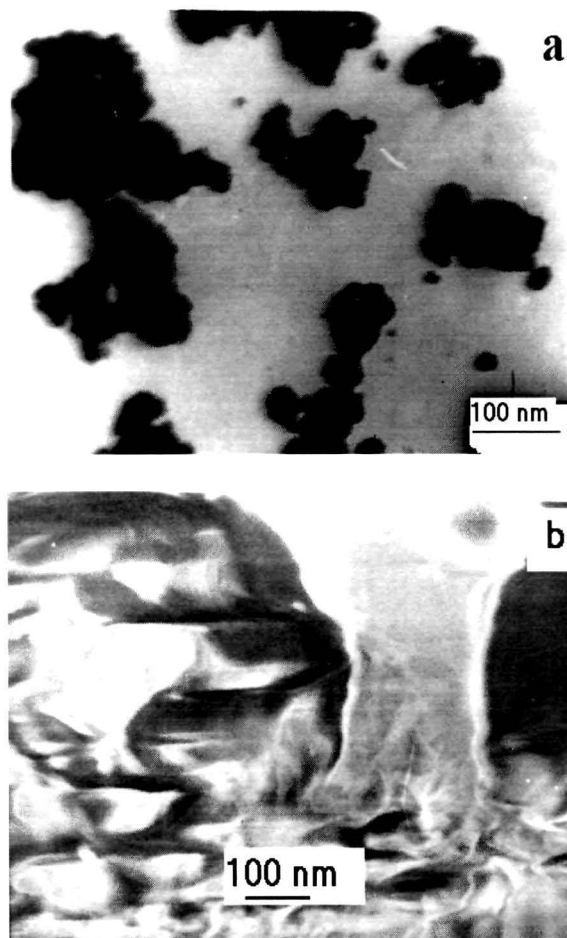


Figure 30. (a) HRTEM image of nanometric CdS powders (b) HRSEM image of molten CdS powder (after irradiation with fluence 5×10^{12} ions/cm²)

Once the matrix is damaged stability of the quantum dots is reduced as melting predominates over splitting - a case we have observed for powder nanometric CdS sample in contrary to the earlier report of grain splitting of nanometric SnO₂ powder [161]. Due to technical hardship in taking TEM image we have taken high resolution SEM photograph of melted nanometric powders shown in figure-30(b). Influence of the grain size governing phase transformation has been studied by Hemon et al. [175]. Also, with specific reference to preceding discussion, we have observed the optical absorption study which fits fairly well with the transmission microscopy study of ZnO quantum dots, where melting was predominant over splitting [176].

In fact, PVOH matrix is a dense, rigid and atactic polymer. It is well known that swift heavy ions on their way through matter lead to heat deposition followed by maximum rise in electronic temperature ($\sim 10^5$ °K) within a time scale of 10^{-15} sec and lattice temperature ($\sim 10^3$ °K) rise within a time frame of 10^{-12} sec. So, under energetic ion irradiation, loosely packed CdS nanodomains (particle size is less than the interparticle separation) come closer due to C-C bond damage of the polymer and finally they melt into bigger domains of dimension ~ 40 nm (figure-31). The mechanism may be analogous to the case of the growth of thin films. The total energy of the system decreases if two islands (here quantum particles) are converted to one. As a result surface area decreases, smaller islands evaporate atoms at higher rate than larger islands and the

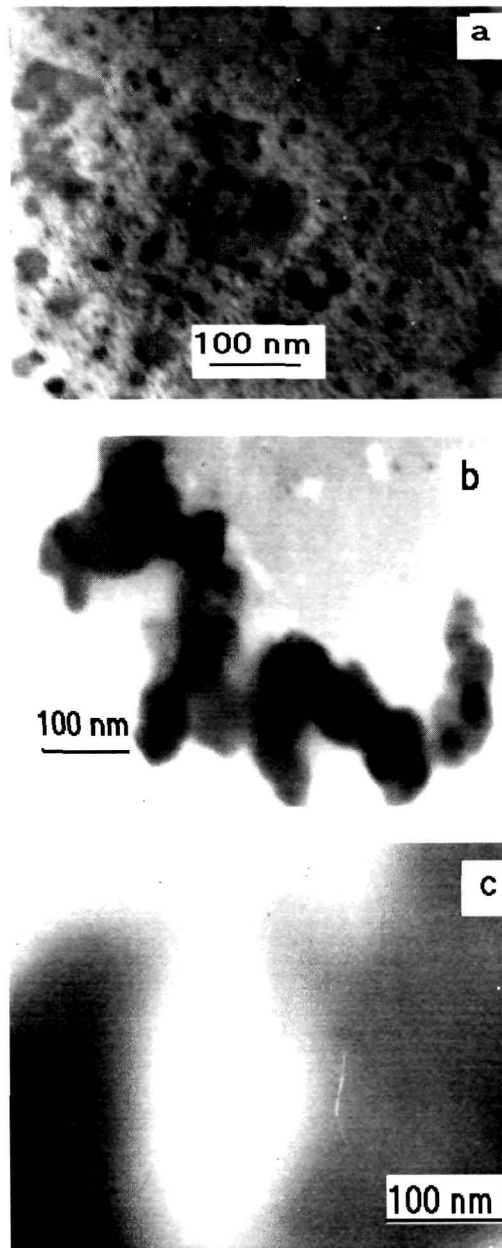


Figure 31. HRTEM images of (a) pristine and (b) ion irradiated (5×10^{11} ions/cm²) assembly of melted quantum grains (CdS/PVOH) (c) HRSEM image of surface polished quantum dot (5×10^{11} ions/cm²)

evaporation rate is given by the curvature of the islands [177]. Moreover, diffusion gradients cause growth of larger islands at the expense of smaller ones. The observed quantum particle grain growth situation may be termed as ostwald ripening under ion irradiation. The inverse ostwald ripening and self organization of nanoclusters due to ion irradiation has been reported by Heinig et al [178]. The positive point of getting larger sized quantum particles is surface smoothing and narrow size distribution.

As depicted in figure-30(a), pristine CdS powder has size range 10 -100 nm. Upon ion irradiation, individual fine particles melted, mixed and exist as if in semifluid form. In contradiction to powder, in CdS/PVOH quantum dot systems, ultra small nanoparticles (~ 4 nm) of pristine sample melted into ~ 40 nm sized surface polished dots (figure-31(a)&(b)). Also, size distribution is narrow due to organized grain growth as a result of melting. Smooth surface of an irradiated quantum grain has been shown in figure-31(c). Figure-33 depicts atomic force microscopy (AFM) images (AFM facility of Universitat "Politechnitat" of Bucharest, Romania) of irradiated CdS/PVOH sample. Although large inhomogeneity is still predominant in the sample, in addition to polished surfaces, AFM images represent spherical and cylindrical growth of the quantum dots. Also, the same surface was tried to visualize using JVC KY-F70 Syncroscopy (Adelaide, Australia) but it did not give appreciable results except feature of some irregular craters (figure-32(b)).

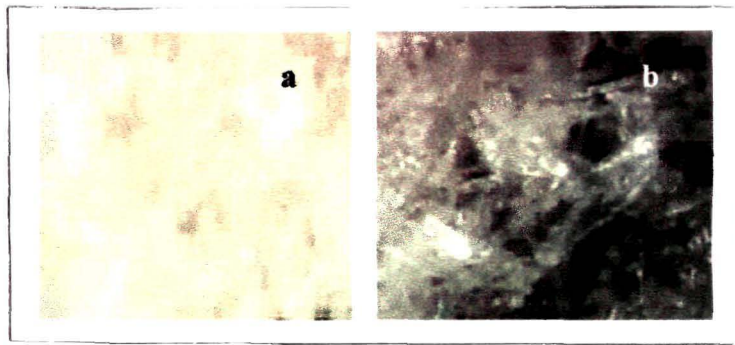


Figure 32. Synchroscopy optical micrographs of (a) virgin and (b) irradiated CdS quantum dot sample

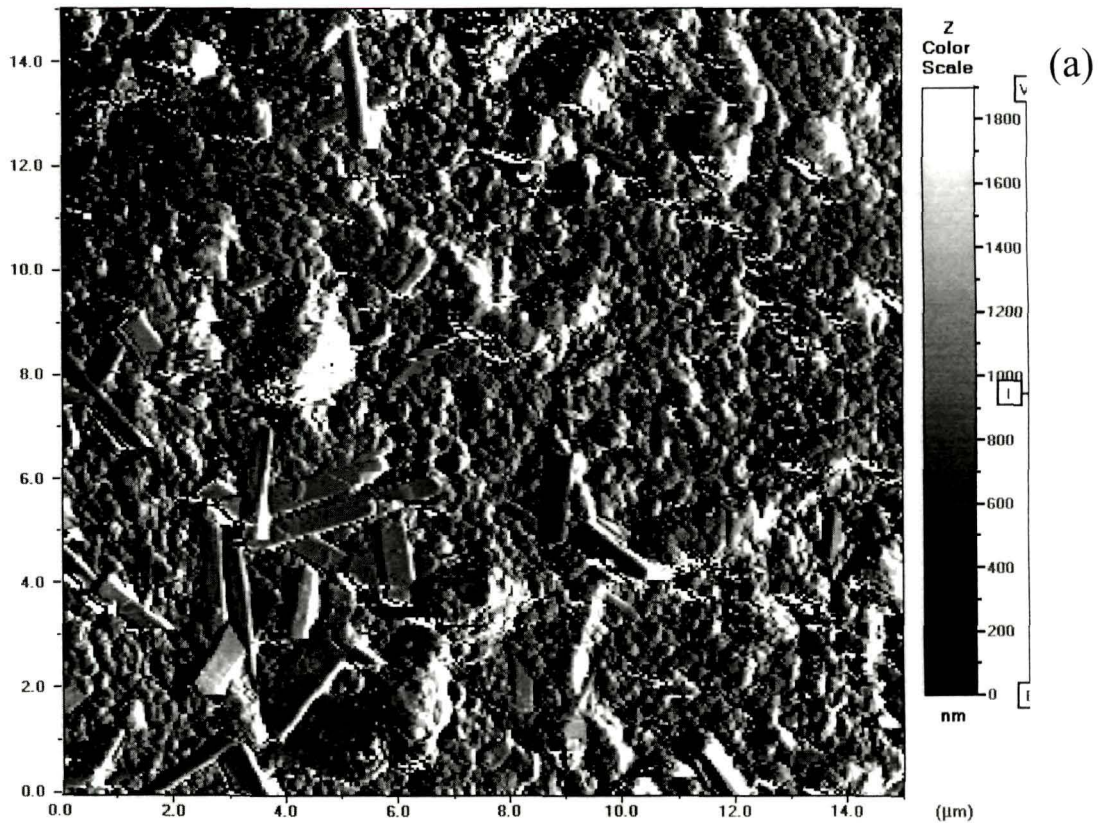


Figure 33. (a) Computer generated AFM view of irradiated (5×10^{12} ions/cm²) CdS quantum dots

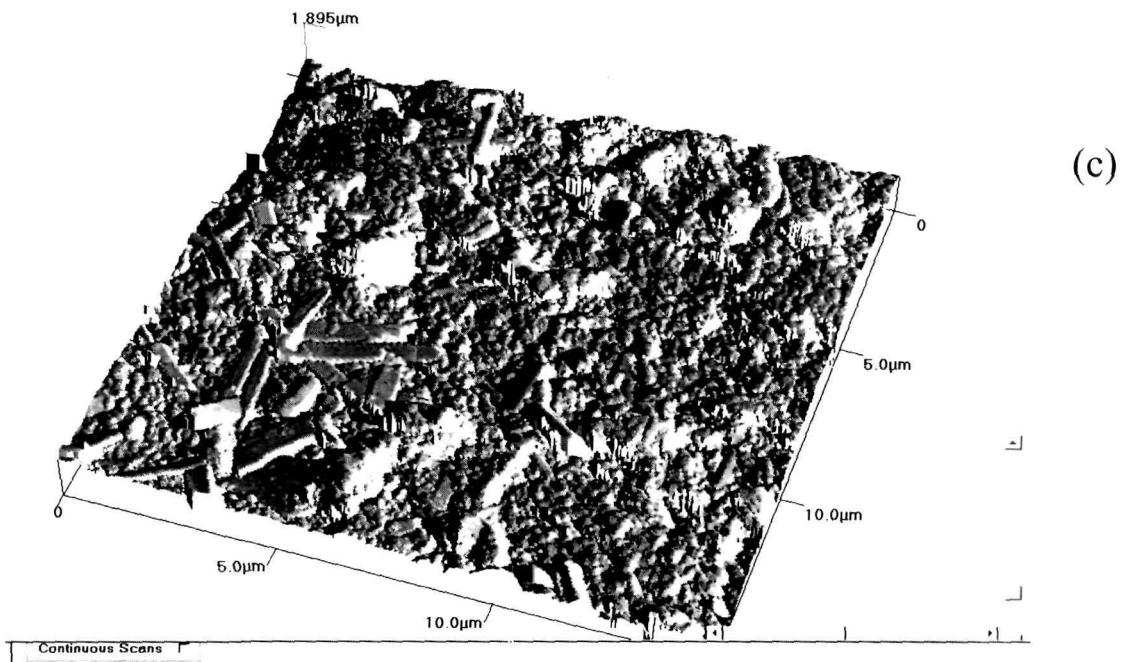
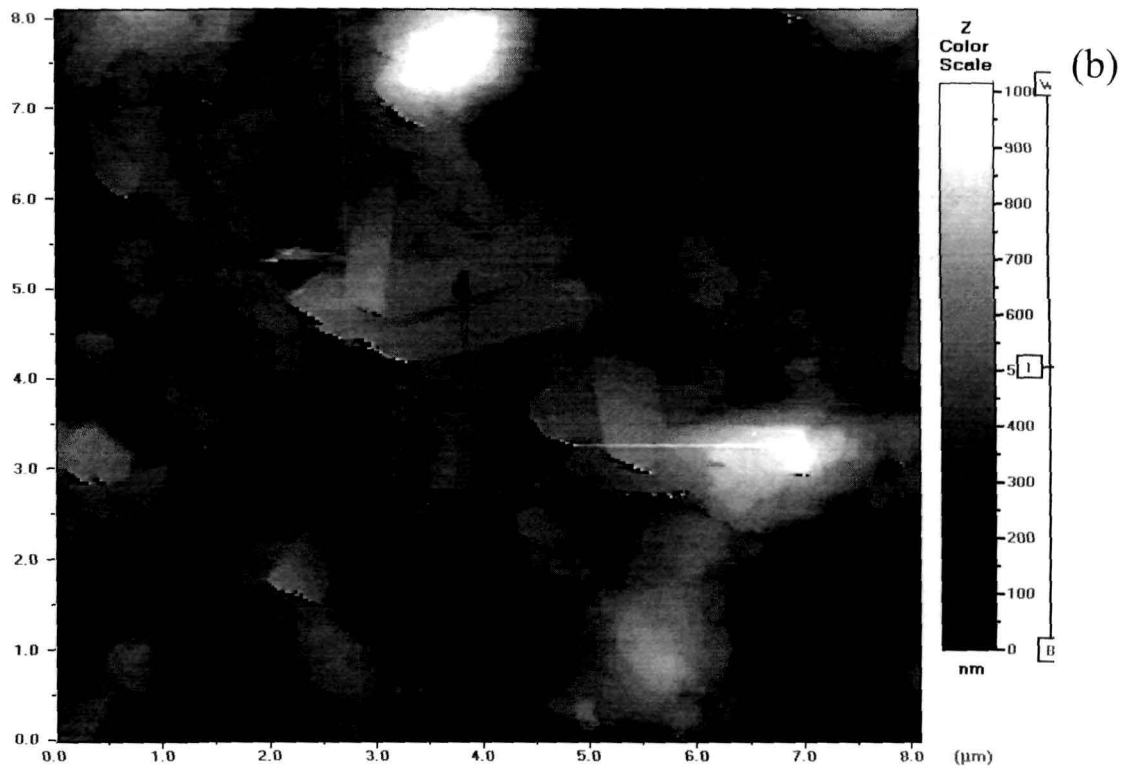


Figure 33. AFM images of (b) original and (c) 3D view of irradiated (5×10^{12} ions/cm²) CdS quantum dots

5.3.2.2 Grain splitting effect

Referring to the electron micrographs depicted in figure-34(a), we say that in CdS/SBR quantum dot samples, domain size is larger than the interparticle separations and therefore nanodomains are supposed to be densely packed. Due to large S_e , SHI irradiation creates a high density of $e^- - h^+$ pairs along its trajectory through CdS quantum grains. Each $e^- - h^+$ pair softens the lattice vibration by removing covalent bonds which results into instability in the lattice structure as observed in case of direct band type InP systems [179]. For quantum dots embedded in SBR matrix, (which is much more flexible and exist in cis-trans isomeric states with respect to PVOH), ion impact causes heat dissipation into whole of the sample region. Therefore, due to the direct impact of ions quantum grains burst into smaller grains (figure-34(b)). Further, one specific feature of such fragmented quantum dots is regular spheroidal shape. The pristine and fragmented particle dimensions are presented in table-11.

Table 11. Grain melting and fragmentation effect of embedded quantum dots

Fluence (Cl cm^{-2})	CdS powder R (nm)	CdS/PVOH R_{avg} (nm)	CdS/SBR R_{avg} (nm)
0	10-100 nm	4.0	65.0
10^{11}	-	11.2	21.1
5×10^{11}	-	19.7	17.2
5×10^{12}	molten	41.0	6.2

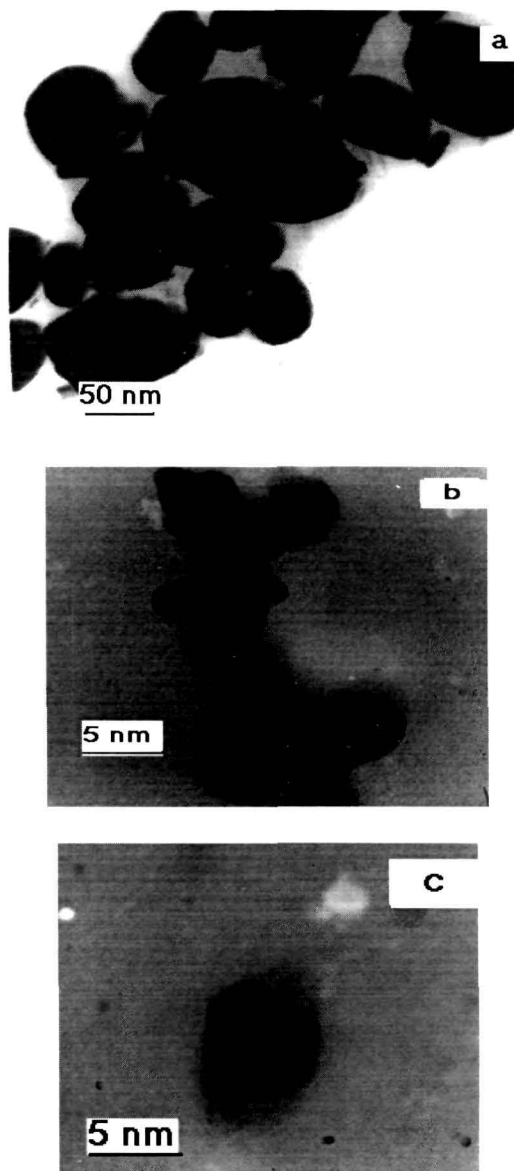


Figure 34. HRTEM images of (a) pristine and (b) irradiated (5×10^{12} ions/cm²) grain splitted CdS/SBR system (c) an isolated quantum grain after fragmentation

5.3.2.3 Interpretation

Due to fast energy transfer by swift heavy ions, the centre of the track is highly ionized. Then violent repulsion among the target ions may lead to atomic motion at the cost of electronic potential energy. The strength of vibration depends upon charge neutralization time and ionization density [171,172,180]. Normally for metals charge neutralization is too fast ($> 10^{-14}$ sec) and Coulomb explosion is not possible [181]. However, when the system is an isolated low dimensional semiconductor it has a large density of surface states. So, electronic recombination will be slow and the explosion model would be relevant for the case. It has been reported in the literature [181], desorption cross section is high ($5 \times 10^{-13} \text{ cm}^2$), for 5 MeV/u Ar + Polypropylene (PP). A large fraction of total deposited energy is converted into broken bonds for $Z_p > 15$. In our case, for chlorine beam $Z_p = 17$ and there are ionization capabilities of $> 60\%$ for all electrons in the center of the track and nuclear potentials of $> 70 \text{ eV}$ for $Z_p > 15$ at 5 MeV/u [181]. Therefore, all ionized hydrogen atoms close to the track would be set in motion by such a strong potential and heat deposition cause semiconducting quantum dots to coalesce as a result of grain growth - a case observed in CdS/PVOH system. In CdS/SBR quantum dot system, the polymer matrix is an elastomer which is relatively flexible and light. The direct ion impact upon individual quantum dots (size $\approx 65 \text{ nm}$) led to grain bursting resulting into $\sim 6.2 \text{ nm}$ grains on an average scale.

Hence, both powder and polymer embedded CdS quantum grains have been irradiated at critical fluence (5×10^{12} Cl/cm²). HRSEM and HRTEM revealed the nature of grain growth / fragmentation as a result of heat dissipation and the dissipation, possibly faster in the later case due to the presence of a flexible matrix. To avoid irregular shapes, to keep size distribution uniform and to obtain smooth surface, embedded quantum dots are to be preferred. In summary we arrived at two complementary aspects:

1. The splitting of larger domains (~ 65 nm) into ultra small domains (~ 6 nm) in case of CdS/SBR quantum dots is possibly due to the increase in internal pressure beyond critical limit. This is in contrary to CdS quantum dots embedded in PVOH where melting and grain growth was noticed. So, a flexible matrix like SBR may be chosen to notice grain fragmentation effect.
2. Stability of embedded CdS particles is more than that of its powder form. The embedded grains can be reshaped and polished by tuning ion fluence, which is not at all possible when taken in powder form.

5.3.3 Irradiation induced surface emission enhancement in ZnS:Mn quantum dot system

Although large number of reports related to luminescence properties [124,164,182-186] are available for both Mn-doped and undoped metal sulfide nanoparticle systems, ion irradiated studies are limited in number as far as luminescence is concerned. After growing Mn doped zinc sulfide nanoparticles in a aliphatic polymer namely, polyvinyl alcohol we have irradiated them with 100 MeV chlorine beam with fluences 1×10^{11} , 5×10^{11} , 5×10^{12} and 1×10^{13} ions/cm². The intention of Mn doping was to correlate luminescence response with ion fluence variation. The irradiation dose deposited in embedded Mn:ZnS/PVOH samples at four different fluences are calculated using SRIM program [155]. The amount of heat deposition as a function of fluence results into melting led grain growth phenomena (table-12).

Table 12.

Irradiation led heat deposition and grain growth of ZnS:Mn quantum dots

Irradiation dose (Cl-cm ⁻²)	Absorbed energy (Joules)	Absorption edge (nm)	Avg. grain size (nm)
0	0	310	11
1×10^{11}	0.539	314	14
5×10^{11}	2.698	320	-
5×10^{12}	26.976	325	32
1×10^{13}	53.952	326	41

5.3.3.1 Absorption spectra of irradiated Mn doped ZnS quantum dots

Figure-35 depicts significant redshift of the onset of absorption of the ion irradiated ZnS:Mn quantum dot samples. As the amount of energy shift is size dependent for a particular material and the size of the nanoclusters alters with fluence variation, we believe there has been significant grain growth of nanoparticles under ion irradiation. It was known that the compounds with oxygen and nitrogen (containing non bonding electrons) are capable of displaying characteristic absorption in the UV region due to promotion of electrons in σ , π orbitals [187]. And so, spectra were taken after calibration with the reference matrix PVOH. Virk et al. [188,189] have proposed that due to the presence of imide group (NC=O), absorption spectra possess transition peaks in the UV regime.

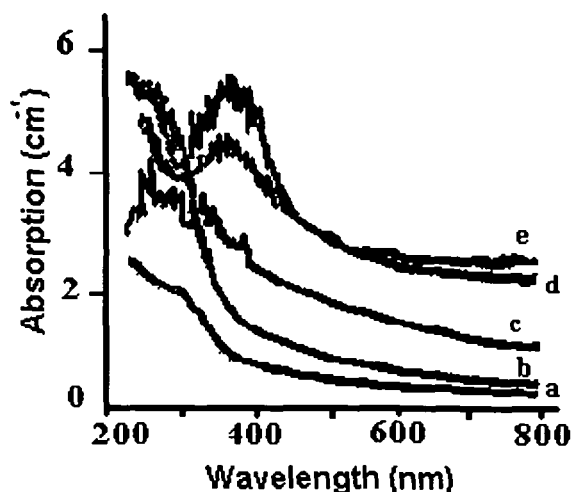


Figure 35. OAS of (a) virgin and irradiated (b) 1×10^{11} , (c) 5×10^{11} (d) 5×10^{12} and (e) 1×10^{13} ions/cm² ZnS:Mn/PVOH nanoparticles

Although in aliphatic alcohols, the hydrogen atom was reported to be removed by interaction of radiation yielding α - hydroxy alkyl radical which has already been investigated [190-192]; aliphatic polyvinyl alcohol has neither N nor double bond(s) to facilitate carrier transition in the ultra-violet regime.

In addition to redshift of the onset of absorption, we see absorption band at around 300 nm, corresponding to exciton absorption of the particles, which has been studied extensively in case of undoped ZnS systems [3,9]. It has been reported in representative ZnS nanoparticle systems that surface states are mainly responsible for evolution of second broad band in the long wavelength (\sim 500 nm) region [115]. Moreover, it was proposed that the second band disappears for capped ZnS nanoparticles in comparison to uncapped ones, because of relatively less number of surface states in capped nanoparticles. We did not see any second absorption band in the virgin and low dose exposed samples. But interestingly, for the samples irradiated with high fluences a second band emerges at around \sim 400 nm (figure-35). We believe appearance of such a band in the absorption spectra possibly due to the presence of surface states of ZnS:Mn nanoparticles which are now free from matrix encapsulation [193]. Thus, even if ZnS:Mn nanoparticles have grown from an average size of 11 nm to 41 nm (table-12) due to ion impact, we observe recovery of the second band due to the surface states when the nanoparticles are free from matrix encapsulation.

5.3.3.2 Illustration of electron microscopic images

Figure-36 represents modified behaviour of ion irradiated nanoparticles with respect to the pristine. The figure-36(a) depicts high resolution SEM image of ZnS:Mn nanoparticles in the form of assembly embedded in PVOH whereas TEM image of individual nanoparticles of size about 11 nm is shown in figure-36(b). Swift ion irradiation leads to deposition of huge amount of energy which causes rise in electronic temperature ($\times 10^5$ °K) and afterwards (10^3 sec) cause lattice temperature rise ($\times 10^3$ °K). The enormous rise in temperature (which exceeds melting point of ZnS i.e. 2100°K) within a time scale of 10^{-12} sec. melts easily all near by particles along with the matrix represented in figure-36(c). Rapid quenching gives rise to recrystallization as if grains have grown independently into definite sizes. The process of grain growth is a combined result of heat deposition and pressure effect. For the samples irradiated with highest dose (1×10^{13} ions/cm²), we have obtained well developed regular nanoclusters of average size 41 nm (figure-36(d)). The cluster of quantum grains is displayed as a cross sectional view against figure-36(e). They are supposed to be freestanding as already the polymer host matrix has been damaged due to complete amorphization. The complete amorphization was confirmed by no weight loss observation of the heavily exposed sample.

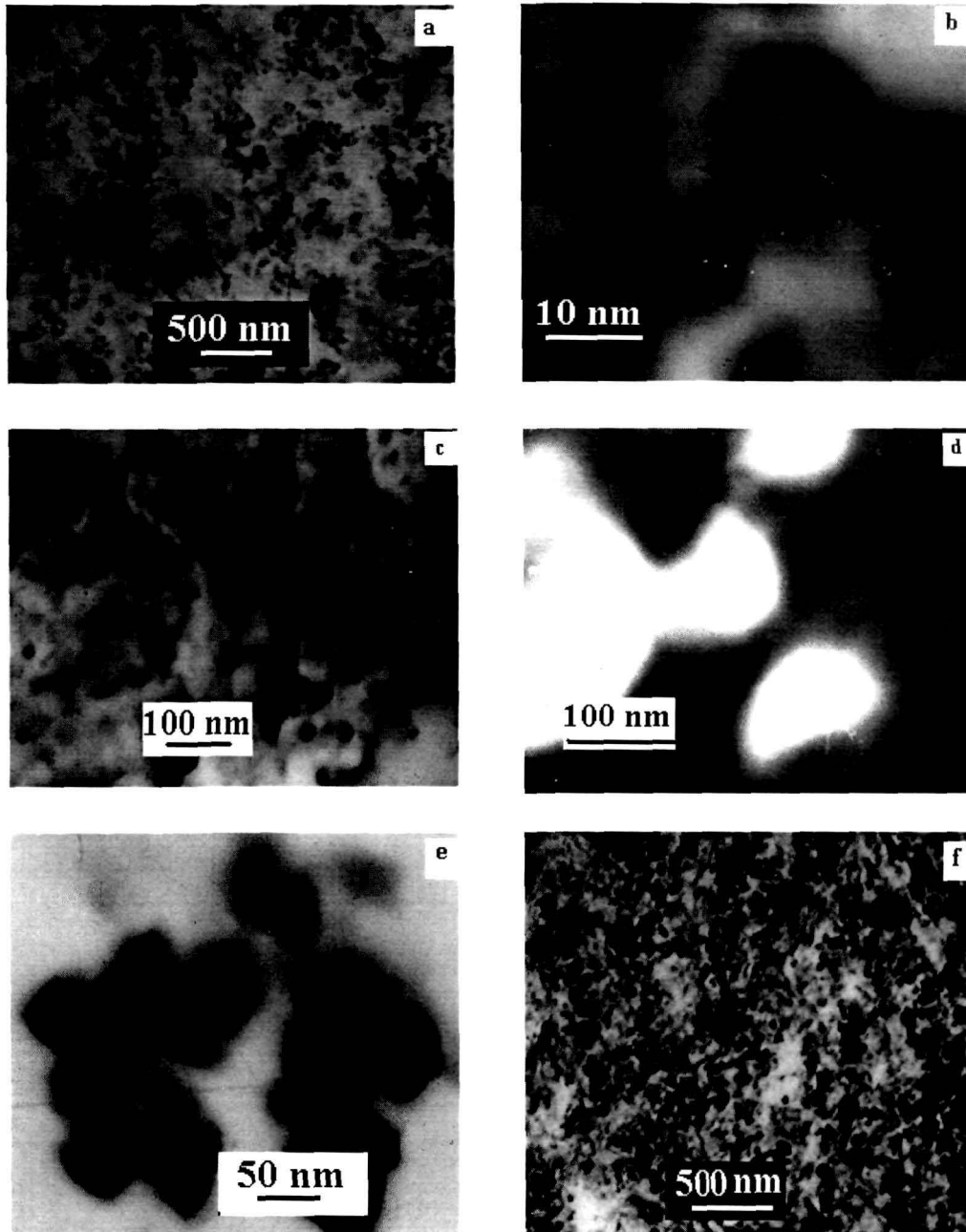


Figure 36. (a) HRSEM and (b) Bright field TEM image of virgin (c) Melting of the ion irradiated (5×10^{11} ions/cm²) (d) & (e) Cluster of individual grains grown as a result of irradiation (1×10^{13} ions/cm²) (f) A cross sectional view of the heavy ion exposed (1×10^{13} ions/cm²) polymer embedded ZnS:Mn nanoparticle samples

5.3.3.3 Photoluminescence (PL) studies

The PL study is important as it provides information relating to different energy states available between valence band and conduction band responsible for radiative recombination. It has been studied that the photoluminescent efficiency of coated ZnS:Mn nanocrystals is higher than the powder samples due to passivation of surfaces [124,183]. The ZnS nanoparticles have got a weak PL emission relative to Mn doped system. The band to band excitation in ZnS has been used to excite the Mn^{+2} emission. The subsequent transfer of electron and hole into the electronic level of the Mn ion leads to the characteristic emission of Mn^{+2} in ZnS systems [116,194]. In consistency with these reports, we have noticed yellow-orange emission for ZnS:Mn nanoclusters with peak wavelength ~ 582 nm [193]. It is attributed to transitions involving d-electrons of the Mn^{+2} ions [195,196]. The Mn^{+2} ion d-electron states act as efficient luminescent centers while interacting strongly with s-p electronic states of the host ZnS nanocrystal into which normally, external electronic excitation is directed. In an undoped quantum dot system, the external band edge as well as impurity related luminescent efficiency at room temperature is too low to be of any practical consequences [197]. We also did not expect such emission for undoped ZnS system (figure-37(a)).

With increase in ion fluence, there is no significant shift of the emission peaks arising out of Mn^{+2} . It is well known that when PL emission peak energies are less than the band gap energy of the material,

these bands correspond to the transitions involving donors, acceptors, free electrons and holes. The appearance of the PL peaks at energies substantially lower than the band gap suggests that the transitions from the energy states in the band gap are being favoured for the luminescence process in these nanocrystalline ZnS films [47]. As depicted in figure-37, the first emission peak position shifts towards blue with increase in ion fluence. We recognize these peaks as a result of trapped luminescence, which have been reported in the form of broad bands in the PL spectra [118]. Such peaks were attributed to the presence of surface states in the nanocrystals. The surface emissions become more intensive with increase in ion dose because of the extent of free standing ZnS:Mn nanoparticles depends on the degree of amorphization of the polymer host matrix.

Previously, surface emission shift due to the size variation was discussed [114]. However, in case of second emission peak arising from Mn^{+2} site, particle size does not significantly affect the emission wavelength [185]. As illustrated in table-12 and 13, in consistency with earlier reports, the shifting of surface emission peak towards blue is due to the grain size effect studied for different substrate conditions [47]. The resulting intense emission may be regarded as the total luminescence contributed by all the surface states, when the particles become fully free standing (for highest dose). Because for heavily exposed samples, the nanoparticles are completely free from matrix encapsulation.

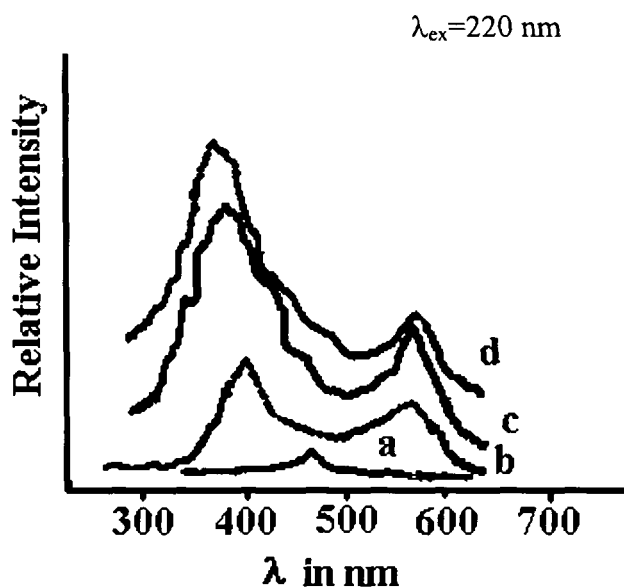


Figure 37. PL emission spectra of unirradiated (a) polymer embedded undoped ZnS and (b) Mn doped ZnS ; and ion irradiated (c) 5×10^{11} ions/cm² (d) 5×10^{12} ions/cm² Mn doped ZnS nanoparticles.

Table 13. Photoluminescence emission of virgin and irradiated ZnS:Mn nanoparticles

Samples	excitation wavelength (λ)	Peak positions in nm			
		λ_1	Energy	λ_2	Energy
ZnS	220	480	2.576	-	-
Mn:ZnS-D ₀	220	405	3.179	580	2.131
Mn:ZnS-D ₂	220	382	3.236	582	2.124
Mn:ZnS-D ₃	220	375	3.296	582	2.124

In conclusion, we claim that embedded polymer system is advantageous to observe regular grain growth process under ion irradiation. The size of the grains can be tuned by selecting proper ion fluence. The samples irradiated with the highest fluence are free standing and that is why strong surface emissions are visible in PL spectra which arise basically, from the surface states. The surface emission energies are calculated to be 3.179 eV, 3.236 eV and 3.296 eV for fluences 0, 5×10^{11} and 5×10^{12} ions/cm², respectively. Moreover, the Mn⁺² emission peak of irradiated samples does not shift appreciably, on the other hand intensity improves because heavily exposed nanoparticles overcome barrier encapsulation. However, shifting of emission peaks towards blue due to size effect is contrary to our experimental results, where main contribution comes through existence of the surfaces states (even in the presence of significant grain growth). Therefore, sensitivity of the optical sensors and other optoelectronic devices could be improved using ion irradiated and doped semiconductor quantum dots.



CHAPTER-6

APPLICATIONS
APPLICATIONS

CHAPTER-6

APPLICATIONS IN NONLINEAR OPTICS AND ELECTRONICS

The possible applications in nonlinear optics and electronics is highlighted in this chapter through various sections and sub sections. As the size of a semiconductor crystal is reduced, the physical properties of these materials change dramatically. For instance, in a large crystal, the overall size and shape of the crystal makes no difference to the crystals' internal properties. However, for smaller crystals, the surface plays an important role and as the fraction of atoms of the surface becomes larger, the arrangement of the nuclei changes to relax the energy of the system as a whole. Thus, even for very small surface-to-volume ratio (if R is the radius of a spherical crystal then, $s/v = 3/R$), semiconductor crystals transform to a more close packed structure. This process minimizes the energy of the entire system. This transition is estimated to take place at a cluster size that contains upto 1000 atoms [198]. For semiconductors in a host material, this structure can be smaller than an isolated structure because of the passivation of the bonds by the host material [199]. We have investigated nonlinear optical properties of PVOH embedded CdS quantum dots. They include third order fluorescence activation process in case of ion irradiated CdS/PVOH quantum dots, nonlinear optical transmission and four wave mixing to estimate respective third order susceptibilities of CdS/PVOH quantum dots. We are

successful in observing third order nonlinearity (relative intensity vs energy) in the fluorescence spectra of irradiated CdS/PVOH quantum dots. The photon induced single electron effects are studied on ZnS/PVOH quantum dots, which are of vital interest for developing single electron devices [200, 202]. As possible application in electronics we have chosen arrayed ZnS quantum dots (arrayed in the sense that quantum dots are larger in comparison with the interparticle separations and uniformly distributed within the sample) and have successfully observed room temperature single electron effects under pulsed laser irradiation at proper biasing. Thus, the single electron effects, which is a prerequisite for developing single electron transistor has been observed if quantum dots are arrayed and pulsed photon is able to excite a few electron - hole pair under desirable bias voltage.

6.1 Third order nonlinearity in the fluorescence activation of ion irradiated CdS/PVOH quantum dots

A number of intensive studies on fluorescence activation process of composite semiconductor nanoparticles have been carried out both for embedded as well as continuous systems. The nonlinear optical properties of CdS are found significant applications in optical switching [203]. Erel and co-workers have reported nonlinearity in the luminescence pattern of single crystal CdS beyond band gap excitation [204]. We have compared fluorescence (FL) activation process both for virgin and ion irradiated

(fluence: 10^{11} - 10^{13} Cl/cm^2) CdS/PVOH quantum dots. It is found that fundamental emission is quenched and shifted towards higher energy values in case of the ion irradiated dots with respect to the virgin ones. Moreover, the lowering in fundamental quantum yield is believed to be compensated by additional fluorescence for significantly large spectrum of energy (figure-38 and table-14).

Table 14. Fluorescence measurements of virgin and irradiated CdS quantum dots

Experimental parameters	Fluence ($\text{Cl}\text{-cm}^{-2}$)	FL emission (eV)	Energy difference(meV)	Relative quantum yield
Instrument: F-2500 FL Spectrophotometer Temperature: 293 ⁰ K Scan mode: Emission EX WL: 350 nm Scan speed: 25 nm/sec PMT voltage: 400 V	0	1.7552	-	100%
	5×10^{11}	1.7519	3.30	28.57%
	1×10^{13}	1.7505	4.70	10.62%

The figure-38 depicts FL emission response of virgin and ion irradiated CdS quantum dots embedded in PVOH polymer matrix. All the samples are excited by $\lambda = 350$ nm (3.56 eV) laser line of F-2500 FL Spectrophotometer with a scan speed of 1500 nm/min. The spectra were analyzed by a novel computing technique*. In this technique the picture is first digitized using standard software MATLAB[®]. The output data is then analyzed using Microsoft Excel[®] spread sheet program.

* Appendix-2

CdS has a characteristic fluorescence spectrum having emission peak at about 700 nm (1.78 eV) [87] below which there is sharp fall in FL emission intensity. However, numerous reports say addition of Cd^{+2} ions and increasing pH of the solution to alkaline values lead to FL activation at around ~ 500 nm, which is close to the onset of absorption [83]. A number of reports have appeared in which the fluorescence was utilized as a parameter for investigating charge carrier dynamics taking place in the particles, where

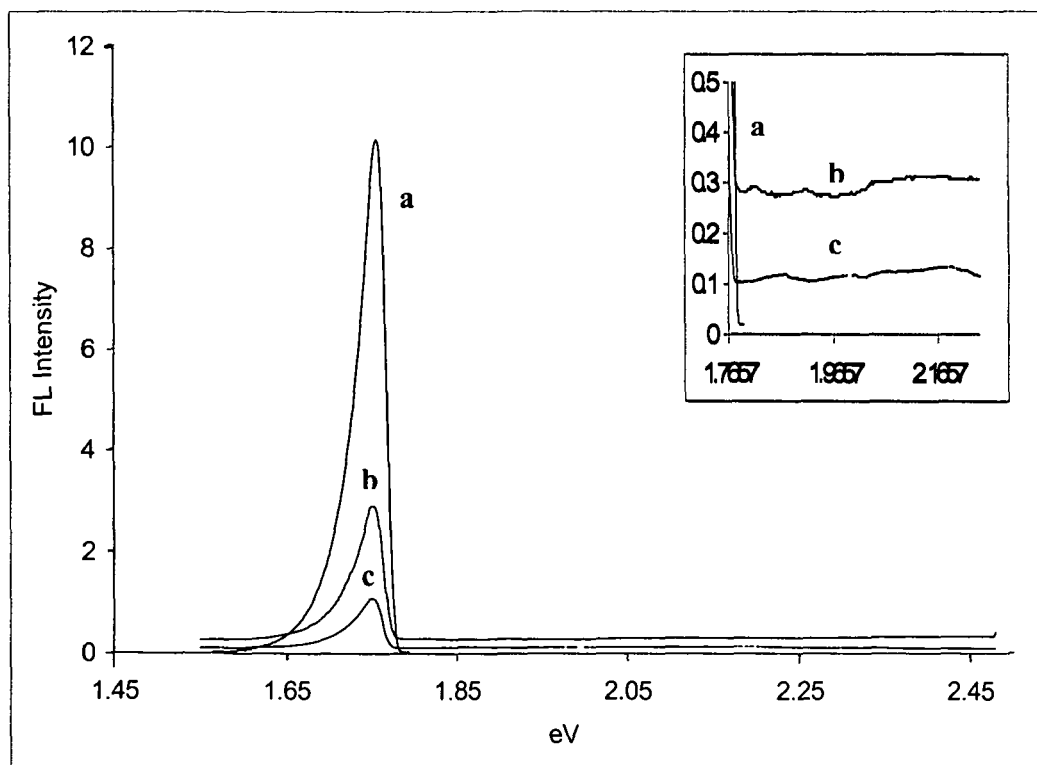


Figure 38. Fluorescence spectra of (a) virgin and ion irradiated (b) 5×10^{11} and (c) 1×10^{13} ions/cm² CdS quantum dots. The inset shows fluorescence response within energy spectrum 1.76 to 2.24 eV

the dynamics were governed by the surface composition and structure [118, 205-209]. Moreover, the FL activation the FL activation has been observed to be size dependent [182,210].

We have observed that CdS fundamental emission ($\lambda = 704.099$ nm, $E = 1.7552$ eV) has been shifted towards higher energy value by amounts 3.30 meV and 4.70 meV for irradiated quantum dots corresponding to fluences 5×10^{11} and 1×10^{13} ions/cm². We believe such spectral shifts possibly due to modification in charge distributions over CdS quantum dots. The illumination of CdS nanocrystals leads to the photo-oxidation products Cd⁺² and SO₄⁻² [2,87,211]. As a result of ionization and subsequent recombination processes, the charge distribution around the dots changes, resulting in a spectral (Stark) shift of the emission [212,213]. Again, the relative quantum yields are suppressed to 28.76 % and 10.62%, respectively with additional yields throughout a broad spectrum of energy with peaks at subsequent points (figure-38, inset). The emission peaks are well resolved in the first derivative plots (figure-39). In fact, irradiation leads to grain growth followed by surface smoothening and thus lowering the surface traps. Therefore, the whole effect destroys the sites where radiationless recombination of the charge carriers can occur leading to the recombination of charge carriers either before they are trapped or while they are trapped in very shallow traps.

Moreover, surface smoothening is justified by relative number of distinct emission peaks for irradiated quantum dot samples. In otherwords,

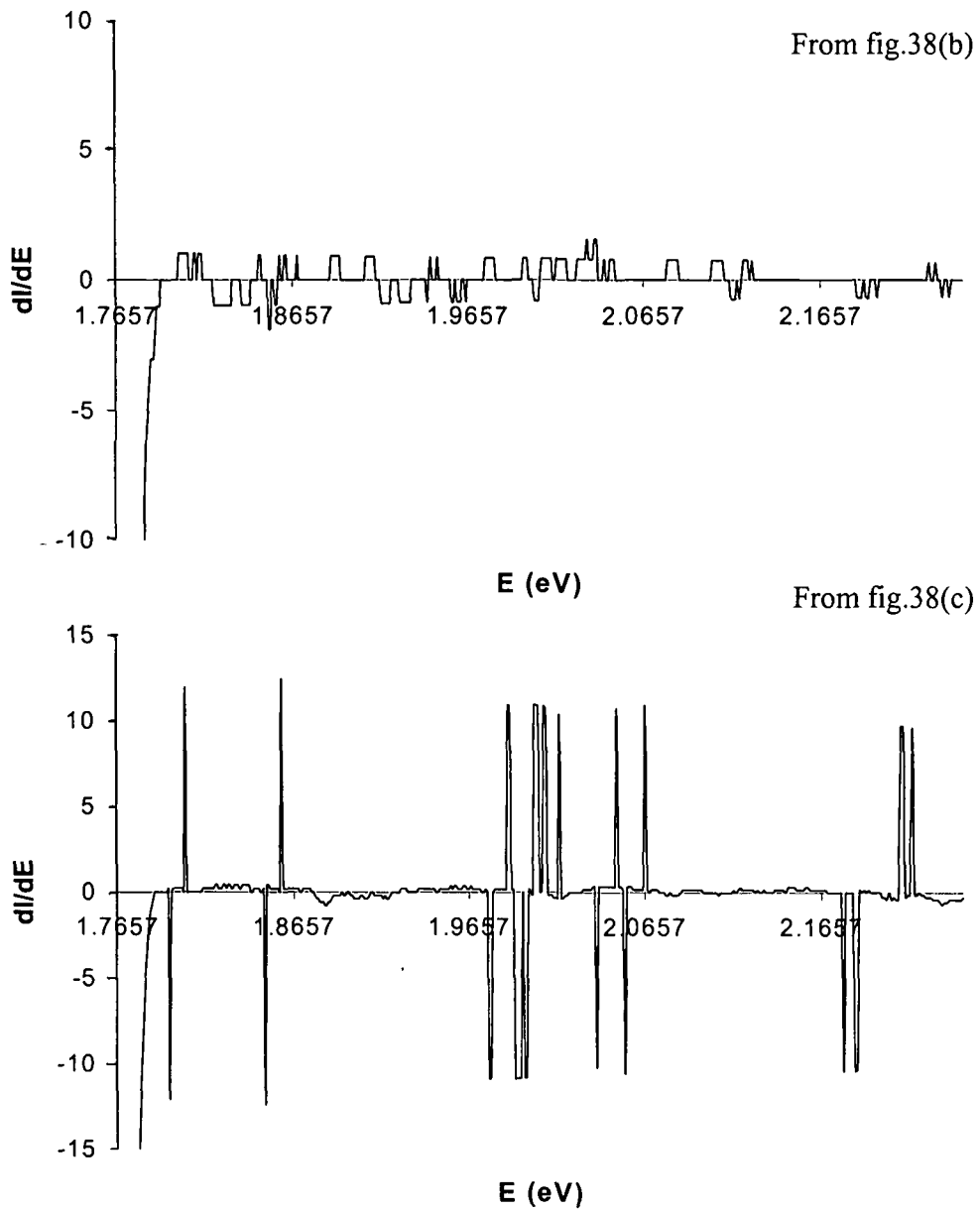


Figure 39. First derivative FL-spectra of ion irradiated CdS quantum dots
(Both spectra are inset of figure-38)

for higher fluence, less number of FL emission peaks are noticed due to decrease in the number of traps (figure-38 & 39). Hence, ion irradiated CdS quantum dots with controlled fluence variation could be suitable options for luminescent devices having broad energy spectrum.

Concerning the numerical values of relative intensities (RI) and photon energy (PhE) of fluorescence emission at fluences: 5×10^{11} , 1×10^{13} ions/cm² an empirical equation can be obtained as:

$$RI = a_0 + a_1 \cdot (\text{PhE}) + a_2 \cdot (\text{PhE})^2 + a_3 \cdot (\text{PhE})^3 \text{ which reads as} \quad (59)$$

$$y = a_0 + a_1x + a_2x^2 + a_3x^3 \quad (59^*)$$

Numerical details of the third order interpolation at different fluences with respect to the above equation are given in table-15 which is essentially a data list of relative fluorescence emission intensity vs corresponding photon energy. The numerical data obtained experimentally, confirms that there exists strong third order optical nonlinearity in irradiated quantum dots (figure-40). The nonlinearity is apparent from the figure-40 because, relative FL emission intensity includes even third powers of the incident energy of photons.

Table 15. Results of fluorescence emission spectra of irradiated CdS quantum dot samples (after adopting digitization procedure)

CdS-D2 (5×10^{11} ions- cm^{-2})		CdS-D4 (1×10^{13} ions- cm^{-2})	
Coefficients:		Coefficients:	
b[0]	3.0105	b[0]	-0.3302
b[1]	-2.4767	b[1]	0.9396
b[2]	0.3511	b[2]	-0.6331
b[3]	0.1032	b[3]	0.1376
Photon Energy (eV)	Relative Intensity	Photon Energy (eV)	Relative Intensity
2.227667328	0.311611785	2.192349278	0.134984348
2.126956042	0.311611785	2.189745022	0.134984348
2.123400581	0.311611785	2.187146946	0.134984348
2.10696438	0.311611785	2.166582195	0.133109565
2.081643978	0.306585789	2.157706225	0.133109565
2.048081105	0.301559792	2.147650895	0.131234783
2.043687652	0.301559792	2.141413767	0.12936
2.039313009	0.301559792	2.132742404	0.12936
2.033870971	0.296533795	2.129047566	0.127485217
2.018786637	0.286481802	2.119256966	0.127485217
2.010267052	0.281455806	2.115608666	0.127485217
1.998669358	0.281455806	2.091604029	0.125610435
1.977921925	0.276429809	2.071624294	0.125610435
1.909535448	0.286481802	2.065820341	0.125610435
1.889651029	0.281455806	2.049740939	0.12186087
1.846614235	0.281455806	2.017217237	0.114361739
1.813225809	0.291507799	2.008426023	0.118111304
1.80978134	0.291507799	2.004059088	0.118111304
1.803784905	0.286481802	1.987850846	0.116236522
*	*	1.966643334	0.114361739
*	*	1.962456016	0.114361739
*	*	1.957246878	0.112486957
*	*	1.955170958	0.112486957
*	*	1.940761907	0.108737391
*	*	1.927570949	0.106862609
*	*	1.872739944	0.119986087
*	*	1.867049647	0.118111304
*	*	1.858578744	0.116236522
*	*	1.850184361	0.116236522
*	*	1.848329229	0.116236522
*	*	1.843707636	0.114361739
*	*	1.83819214	0.114361739
*	*	1.831798958	0.112486957
*	*	1.828165638	0.110612174
*	*	1.825450092	0.110612174
*	*	1.820942066	0.108737391
*	*	1.80401274	0.104987826

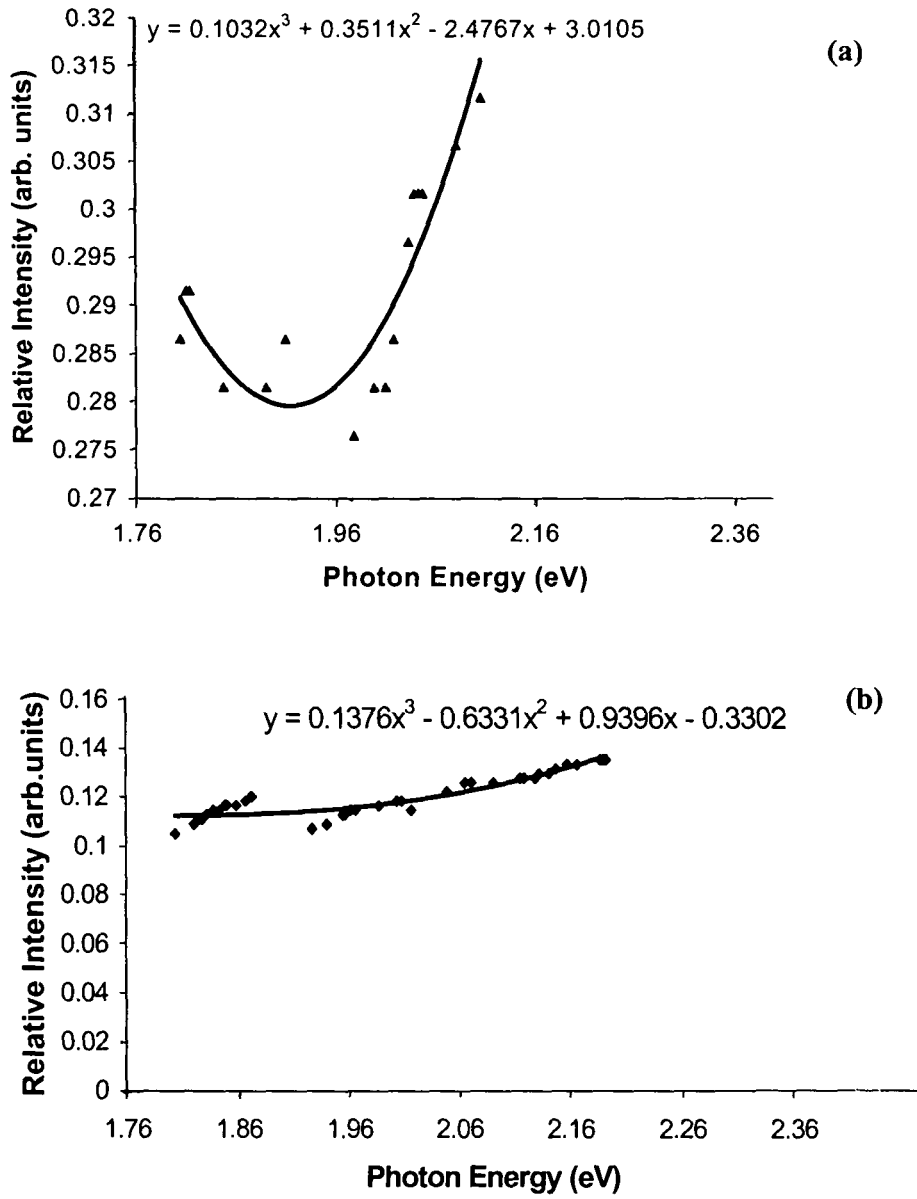


Figure 40. Third order nonlinearity observation in irradiated (a) 5×10^{11} and (b) 1×10^{13} ions/cm² CdS/PVOH quantum dots

6.2 Nonlinear optical phenomena and third order susceptibility of quantum dots

Nonlinear effects are observed when intensity of the light falling onto the semiconductor reaches high levels, such as when high power laser beams are used. Although, there already exists an extensive literature on the subject of nonlinearity, and in particular third order nonlinearity $\chi^{(3)}$ of semiconductor microcrystallites, there are gaps while realizing the figure of merit for possible practical applications. To emphasize the improvement of our experimental results over existing reports, we have highlighted in this section some of the ideas that have been proposed by several workers. The nonlinear optical phenomena as a subject of interest has been discussed in various general texts [214-216]. Schmitt-Rink et al. [199] have shown that the reduction in dimensionality of the systems from 3D (bulk) to 0D for semiconductors can in certain conditions lead to enhanced nonlinearity which is determined by the electron and hole states of these ultra small crystallites.

We are here concerned with the effects of intense beams on the optical absorption coefficient α or refractive index n for semiconductor with dielectric constant ϵ . As the semiconductor responds to the oscillating electric field of the light beam in its passage through the sample, the electric field may be written as

$$E = E_{\omega}(z, t) = E_0 \cos(kz - \omega t) \quad (60)$$

for the plane wave propagation, where E_0 is the amplitude of the field, t the plane wave propagation time, k the wave vector magnitude, with $k = 2\pi / \lambda = n\omega / c$, ω being the frequency, λ the wavelength, c the velocity of light and z the direction of the incident light. The phase velocity is $v = c / n$, and kz is the relative phase of the wave. For low light intensities, and therefore for small optical fields, we are concerned with linear optics, and the bound electrons of the semiconductor can be treated as harmonic oscillators with small displacements. For large intensities and optical fields, the electron motion becomes anharmonic, leading to nonlinear optical effects.

The practical applications of nonlinear optical effects [217,218] have arisen as a direct consequence of the invention of the laser. The very high intensities of lasers have enabled several theoretical predictions to be actually observed and exploited. In order to explain nonlinear effects [218] it is normally assumed that the nuclei and associated electrons of the atoms in the solid form electric dipoles. The electromagnetic radiation interacts with these dipoles causing them to oscillate which, by the classical laws of electromagnetism, results in the dipoles themselves acting as sources of electromagnetic radiation. If the amplitude of vibration is small, the dipoles emit radiation of the same frequency as the incident radiation. As the intensity of the radiation increases, the relationship between intensity and amplitude of vibration becomes nonlinear resulting in the generation of harmonics of the frequency of the radiation emitted by the oscillating dipoles.

Thus, frequency doubling or second harmonic generation and indeed higher order frequency effects have become possible.

Then, the bulk electric polarization \bar{P} (dipole moment per unit volume) induced in the medium can be represented by a Taylor series of the form:

$$\bar{P} = \epsilon_0(\chi^{(1)}(\bar{E}) + \chi^{(2)}(\bar{E}) + \chi^{(3)}(\bar{E}) + \dots) \quad (61)$$

where E is the optical field amplitude, $\chi^{(1)}$ is the first order (linear) optical susceptibility, and $\chi^{(2)}$ and $\chi^{(3)}$ are the nonlinear second and third order optical susceptibilities. In general,

$$\chi^{(1)} \gg \chi^{(2)} \gg \chi^{(3)} \quad (61')$$

and nonlinear terms $\chi^{(2)}$, $\chi^{(3)}$ are important when intense light sources are used, and optical electrical fields greater than 10^6 V/m are generated. For low light levels, where \bar{E} is only of the order of hundreds of volt per meter, it is only the linear term $\chi^{(1)}$ becomes significant [218].

At optical frequencies, $\chi^{(1)}$ is related to the refractive index \mathbf{n} by the relation

$$\mathbf{n}^2(\omega) = 1 + 4\pi\chi^{(1)}(\omega) = \epsilon(\omega) \quad (62)$$

As \mathbf{n} is complex, it contains both real and imaginary terms, i.e., $\mathbf{n} = n + iK$, where K is the extinction coefficient. The real parts of $\epsilon(\omega)$ and \mathbf{n} relates to refraction, while the imaginary part iK relates to the absorption of light. In the linear case involving $\chi^{(1)}$, the normal refractive index n , as well as k and ν are independent of the optical electric field strength E and therefore of I .

For simplicity, we consider only time dependent terms given by

$$E = E_0 \cos(\omega t) \quad (63)$$

For the modulation effects resulting from the effect of the optical field on both n and α , the polarization $\bar{P}(\omega)$ can be represented by

$$\bar{P} = \chi^{(1)} E_0 \cos(\omega t) + \chi^{(2)} [E_0 \cos(\omega t)]^2 + \chi^{(3)} [E_0 \cos(\omega t)]^3 + \dots \quad (64)$$

Expanding $\cos^2(\omega t)$ and $\cos^3(\omega t)$ and rearranging gives

$$\begin{aligned} \bar{P} = & \frac{1}{2} \chi^{(2)} E_0^2 + \chi^{(1)} E_0 \cos(\omega t) + \frac{3}{4} \chi^{(3)} E_0^3 \cos(\omega t) + \\ & \frac{1}{2} \chi^{(2)} E_0^2 \cos(2\omega t) + \frac{1}{4} \chi^{(3)} E_0^3 \cos(3\omega t) + \dots \end{aligned} \quad (65)$$

Since second order nonlinear interactions involving $\chi^{(2)}$ only take place in non-centrosymmetric crystals having no inversion symmetry, we can ignore the terms in $\chi^{(2)}$, since most of the systems with which we are concerned have a symmetric structure and inversion symmetry with $\chi^{(2)} = 0$. In symmetric materials [217,218], an applied electric field produces polarizations of the same magnitude but of opposite sign according to whether the electric field is positive or negative and there is no net polarization. Consequently, the coefficients of even powers of \bar{E} in equation-61 are zero. Thirdorder interactions involving $\chi^{(3)}$ occur in all materials and this is the process of interest here. Thus, for the term in equation-64 containing $\chi^{(3)}$; $(1/4)\chi^{(3)} E_0^3 \cos(3\omega t)$ represents the response at frequency 3ω resulting from an applied field at frequency ω , which leads to

third harmonic generation. The third harmonic generation in nanoparticle systems have been reported by several experimentalists [219].

Two regimes that are concerned with nonlinear responses, are the 'resonant' and 'non-resonant' cases. This depends on whether the incident photon energy (single photon resonance, or a multiple thereof, that is, two and three photon resonances) lies close to an optical absorption edge, or to features such as excitons, for the resonant case. For the non-resonant case, the incident photon energy is on the lower energy side of the absorption edge, and it involves small absorption coefficients, and little dispersion in the normal refractive index.

The response times for the resonant regime are relatively slow, of the order of a nanosecond, but $\chi^{(3)}$ values can be enhanced by exciton effects to near 10^{-9} e.s.u, although values as high as 10^{-4} e.s.u have been reported [9]. The penalty for working in this mode is the loss in transmitted light due to the high α values (10^5 - 10^6 cm^{-1}) which limits possible practical applications. Non-resonant response times are faster and ideally should be in the region of a picosecond. The other advantage of concentrating on this regime is the damping factor due to low α values, thus avoiding attenuation of the optical signal. Working in this region therefore involves only the real part of Δn , and since $\chi^{(3)}$ values are smaller, the signals are weaker than for the resonant case.

The total polarization of the semiconductor can be represented by the general relation

$$\bar{P}_\omega^{total} = \chi_{eff} \bar{E}(\omega) \quad (66)$$

where

$$\chi_{eff} = \chi^{(1)} + \chi^{(2)} E(\omega) + \chi^{(3)} E^2(\omega) + \dots \quad (67)$$

Since we are not concerned with the terms containing $\chi^{(2)}$, we may write

$$\chi_{eff} = \chi^{(1)} + \chi^{(3)} E^2(\omega) \quad (68)$$

Observing equations-65 & 68, where we are dealing with the terms that include the nonlinear polarization at the same frequency ω as the incident field, we have

$$\chi_{eff} = \chi^{(1)} + \frac{3}{4} \chi^{(3)} E^2(\omega) \quad (69)$$

while the intensity dependent refractive index is obtained from

$$\vec{P} = \chi^{(1)} \vec{E}_0 \cos(\omega t) + \frac{3}{4} \chi^{(3)} \vec{E}_0^3(\omega) \cos(\omega t) \quad (70)$$

Since $\mathbf{n} = n + iK$, and for the non-resonant case we are mainly concerned with the real part of the refractive index (n), we have

$$n^2 = 1 + 4\pi \chi_{eff} \quad \text{and hence,}$$

$$n^2 = 1 + 4\pi (\chi^{(1)} + \chi^{(3)} E^2) \quad (71)$$

$$n^2 - n_0^2 = 4\pi \chi^{(3)} E^2 \quad (72)$$

with n_0 being the linear (normal) or low intensity refractive index. Using simple algebra we obtain,

$$n = n_0 + \frac{2\pi}{n_0} \chi^{(3)} E^2 \quad (73)$$

$$\Delta n_{\chi^{(3)}} = n - n_0 = \frac{2\pi \chi^{(3)} E^2}{n_0} = \frac{2\pi \chi^{(3)} I}{n_0} \quad (74)$$

In general, then

$$\Delta n \propto \frac{\chi^{(3)} I}{n_0} \quad (75)$$

with the constant of proportionality depending on the units used. The validity of the above expression was confirmed by Cotter et al. [220].

In general, the relation is sometimes written in the form

$$n = n_0 + n_2 I \quad (76)$$

where n_2 represents the nonlinear refractive index, which for solid semiconductors can be written as [215,221]

$$n_2 = \frac{16\pi^2 \text{Re} \chi^{(3)}}{cn_0^2} \text{ e.s.u} \quad (77)$$

and $I = \left(\frac{cn_0}{8\pi} \right) E^2 \quad (78)$

6.2.1 Non-resonant transmission response of CdS quantum dots

The non-resonant case is far simpler to handle, since we are concerned with optical effects far removed from the optical absorption edge, that is, when the photon energy of the incident light $\hbar\omega$ (1.17 eV which corresponds to $\lambda = 1064$ nm of the pump beam) is less than the energy gap E_g (2.42 eV, the band gap energy of bulk CdS). This means that absorption coefficients are low, exciton effects and multiple-photon absorption are

absent, and the major factors to be considered are the local field and the anharmonicity of the electronic structure. In a similar way to the reported study [220] of the linear dependence of Δn and $\Delta\alpha$ on I for 3.5-6 nm CdSe-Te clusters dispersed in glass, we have investigated, band gap excitation (non-resonant) by observing optical nonlinearity of polyvinyl alcohol (PVOH) embedded CdS quantum dots (2-7 nm). Quantum dot concentrations are as low as $\sim 1.0 \times 10^{12} / \text{mm}^3$ and fills only about 4 vol % of the sample. Although the size range is from strong to weak confinements regimes ($0.4 - 3.5 a_B$) excitonic effects may come into picture. But such effects are of significant interest for resonant cases only. As excitation energy of pulsed laser (1.171 eV) is small by an amount 1.248 eV to start resonant process in CdS (2.42 eV), it means such excitations may disturb the fermi level which is at about half of band gap energy. The experimental arrangement for observing transmission is as depicted below (figure-41).

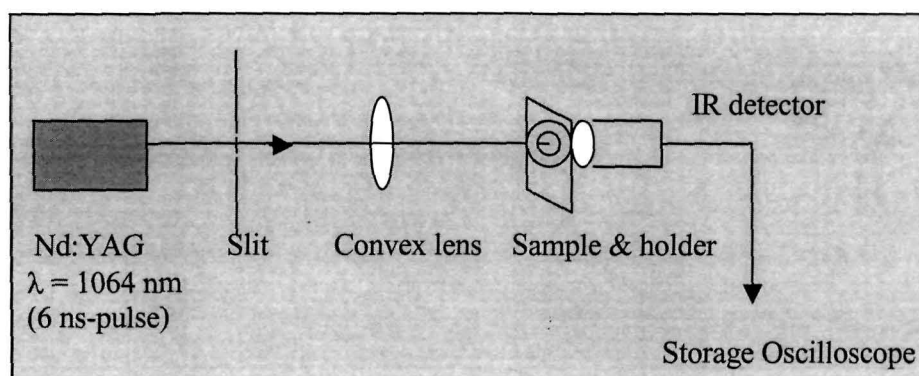


Figure 41. Set up for intensity dependent transmission response of CdS quantum dots

The Nd-YAG* laser was operated in Q-switching mode to obtain pulse train of width 6 ns. The beam is concentrated near the sample by means of lens and slit arrangement. Care was taken to focus the beam near the sample and not exactly over the sample to avoid unwanted heating/burning. A silicon infra-red (IR) sensitive photodiode (SFH 203 FA, UK) having power dissipation 100 mW, $\lambda_{\text{peak}} = 900 \text{ nm}$ and angle of acceptance 40° was placed in close proximity with the sample and aligned horizontally with the principal beam. The detector was fed to a 60 MHz digital storage oscilloscope. In order to get information only from embedded CdS quantum dots, at first PVOH sample was placed as a reference sample and then subsequent

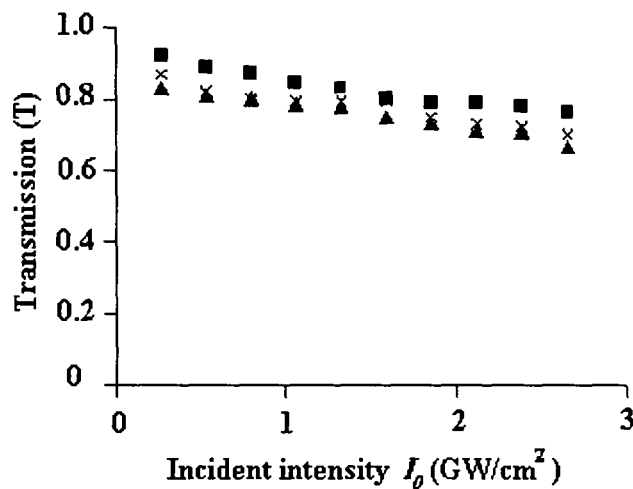


Figure 42. Transmission (T) vs incident power (I_0) for CdS quantum dot films of thickness (■) 0.092 μm , (x) 0.182 μm and (▲) 1.211 μm

* Appendix - 6

CdS/PVOH samples were tested. Laser power of single shot (pulse) was varied and corresponding information was stored in the oscilloscope.

The figure-42 is a plot of the intensity of incident 6 ns laser light to that of transmitted light obtained from oscilloscope graphs. It infers that transmission falls with incident power of the IR laser beam probably due to local field intensity enhancement in the samples. Of course, relative transmission is weaker in 1.21 μm sample due to thickness effect.

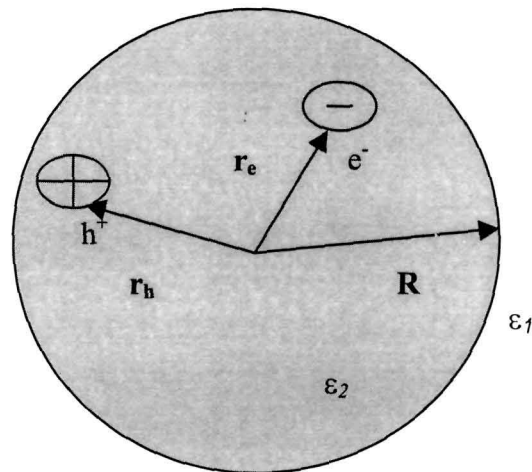


Figure 43. Schematic representation of CdS quantum dot (ϵ_2) embedded in PVOH polymer (ϵ_1)

A spherical quantum dot embedded in a matrix such as polymer for which $\epsilon_2 > \epsilon_1$ and $n_2 > n_1$ can have the local field in the cluster enhanced at the crystallite-polymer boundary, with ϵ_2 and ϵ_1 representing dielectric

constants of the cluster and the matrix respectively (figure-43). The reports are available with respect to local field intensity enhancement which can be characterized by a factor Q_{NF} , and this has been calculated as a function of R for different pump laser wavelengths [4,12].

6.2.2 Non-resonant non-degenerate four wave mixing phenomena of CdS/PVOH quantum dots

The third order process involves four photons and the fourth photon which is generated as a result of the process can have any of the previous frequencies. Figure-44 gives a schematic geometry of the experiment in which nonlinear mixing of four waves occur. The wave K_4 is the optical conjugate wave whose intensity is measured as a function of the intensities of the pump waves [38].

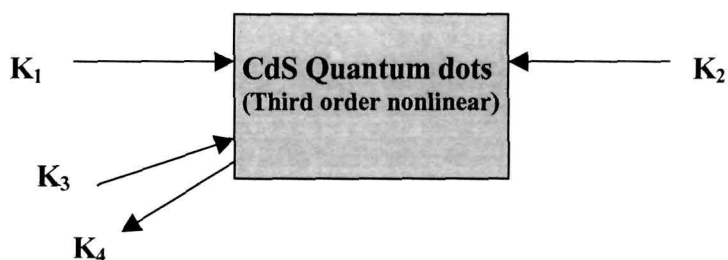


Figure 44. Schematic representation of four frequency mixing

Wave vector of pump waves: K_1, K_2

Wave vector of probe wave: K_3

Wave vector of phase conjugate wave: K_4

Four wave mixing is the classical technique and is especially useful for the determination of the magnitude of the third order susceptibility and the time dependence of the electronic modification to the nonlinear material induced by the incident laser light. In its most typical incarnation, the wave mixing is done at a single frequency, in which case it is referred to as degenerate four wave mixing (DFWM). In our case, the frequency of probe beam (He-Ne; $\lambda = 632.8 \text{ nm}$) is different from that of pump beam (Nd:YAG; $\lambda = 1064 \text{ nm}$) and so it is a case of non-degenerate four wave mixing (NDFWM).

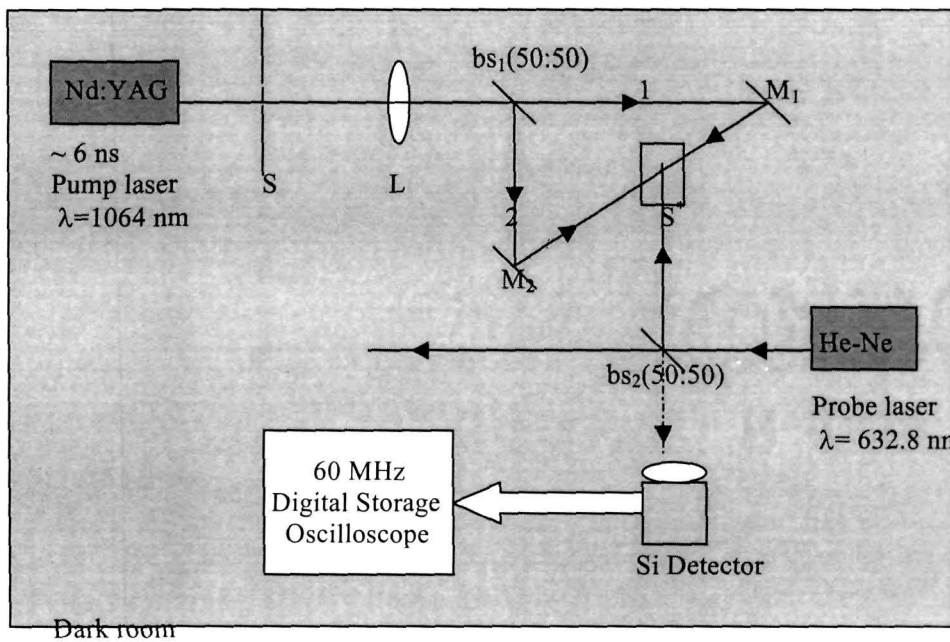


Figure 45. Non-degenerate four wave mixing (NDFWM) experimental setup

Our method was based on self diffraction for analyzing change in refractive index with respect to the incident intensity of light. To obtain an estimate for the refractive index change, the self-diffraction has been measured in a thin-grating approximation ($d \ll 2\Lambda^2/\lambda$, d thickness of the grating, Λ the grating constant and λ the wavelength of the light) [222]. In fact, the quantum dot sample, where the nanoparticles are embedded is supposed to fit under this approximation.

We have taken $d = 0.091 \mu\text{m}$, $\Lambda \approx 200 \text{ nm}$ and $\lambda = 632.8 \text{ nm}$ to satisfy the above conditions. The PVOH polymer is transparent to IR and the embedded quantum particles behave as a grating under pump beams. As shown in figure-45, the two coherent pump beams produced by a Nd:YAG laser and split by a 50:50 beam splitter, intersect on the sample. The two beams falling over the sample from opposite directions were adjusted to establish the arrangement of self diffraction experiment. The diffracted and transmitted orders are detected by time integrated movable Si-detector. The efficiency of a thin grating is correlated with the nonlinear change in the refractive index in simplest approximation by

$$\eta = \frac{I_1}{I_T} \approx \left| \frac{\pi \Delta n d}{\lambda} \right|^2 \quad (79)$$

where I_1 is the intensity of the first diffracted order, I_T the transmitted intensity of the pump beam (zeroth order intensity), d the thickness of the grating and λ the wavelength of the probing laser. Instead of incident intensity, use of the transmitted intensity allows us to take absorption losses

into account. Both I_1 and I_T were measured corresponding to different incident intensity I_0 . The plot-46 depicts change in refractive index Δn (10^{-4}) vs incident intensity I_0 (GW/cm^2).

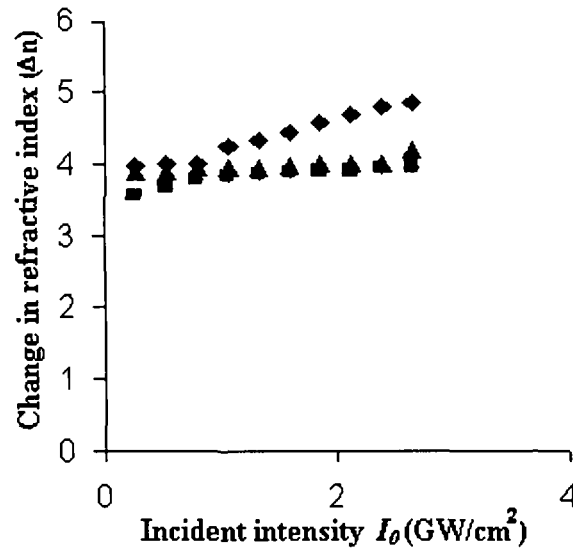


Figure 46. Change in refractive index Δn (10^{-4}) vs incident intensity I_0 (GW/cm^2) of CdS quantum dot films (thickness: (■) $1.211 \mu\text{m}$, (▲) $0.182 \mu\text{m}$ and (◆) $0.092 \mu\text{m}$)

Table 16. Thirdorder susceptibility of CdS quantum dots

Sample thickness (μm)	Slope: $\frac{\delta(\Delta n)}{\delta I_0}$ $10^{-4} (\text{cm}^2/\text{GW})$	$\chi^{(3)} = (\text{Slope}) \frac{n_0}{2\pi}$ $10^{-14} (\text{cm}^2/\text{W})$
0.092	0.4061	1.5096
0.182	0.1045	0.3885
1.211	0.0940	0.3494

The respective slopes $\delta(\Delta n) / \delta I_0$ are obtained from figure-46 for individual quantum dot samples and the equation-74 was used for the determination of third order susceptibility (table-16) taking linear refractive index of CdS to be 2.336 corresponding to $\lambda = 1.064$ nm. It is found that third order susceptibility of these system is 100 times more than the previous report [50], where degenerate four wave mixing was the method selected with respect to our non-degenerate case. Although relatively high values of $\chi^{(3)}$ have been reported [223-229] and reviewed [230,231] by using z-scan and four wave mixing, while considering band gap excitation as well as degenerate frequency mixing, as far as non-resonant excitation is concerned, we have been successful in observing appreciable amount of third order nonlinearity in polymer embedded CdS quantum dots. The probable cause of nonlinear response may be due to two components, a fast component due to the free carriers (tens of ps) and a slow component due to trapped carriers (tens of ns). Semiconductor doped host matrices contain both types of particles, that is, particles without traps that are responsible for the free carrier component and particles with traps that are responsible for the slow nonlinearity.

6.3 Frequency dependent current density and capacitance response of CdS/PVOH quantum dots

The problem associated with conventional devices is that as gate length shrinks to 0.1 μm and below, most of the physical effects comprise to make successful CMOS operation difficult. These include: hot electron effects, oxide tunneling, silicon tunneling, and drain induced barrier lowering etc. As device size shrinks, the capacitance of the interconnections become increasingly important if very small conductors are used. In fact, interconnections become the limiting factor in circuit speed. Power dissipation becomes a problem as size decreases, e.g. if we want to operate at 10 GHz dissipation becomes over 3 KW/cm^2 [232]. Most of the quantum devices operate in the ground state, so no energy is required for internal devices. Quantum devices can be incorporated in actual circuits and complete functional units such as a microprocessor of a supercomputer can be realized. Quantum mechanical coupling between nearest neighbours can replace physical wires that carry signal from one device to the next. The eliminations of physical interconnections results in unprecedented density and improved speed operation required by long distance telecommunications and transmission links [233,234].

Since quantum dots are of the order of a few atomic dimensions, direct electrical probing is a cumbersome job for practical applications. Of course, probing by nanolithographic process is under serious investigations and requires much more sophistication and complexities [235]. On the

otherhand, it is also very important to get frequency dependence information from current and capacitance measurements for a given quantum dot specimen, prior to device fabrications.

We have chosen 1.21 μm thick CdS/PVOH quantum dot films for investigation. They were shaped into a diameter of 0.83 mm (size of the holding plates). Schottky junctions were fabricated by means of thin Ag coating and the samples were placed in a specially designed flexible sample holder. The contact leads were taken from upper and lower plates by means of copper wires. Forward biased I - V measurements were performed by using Hikoi 3532-50 variable frequency LCR Hi-Tester. Capacitance-Voltage (C - V) measurements were carried out by using the above variable frequency LCR meter. Both I - V and C - V measurements were taken at 293⁰K.

6.3.1 Current-Voltage (I - V) characteristics

It was known that bulk-CdS/metal junctions drives at higher bias voltage with respect to nano-CdS/metal junctions [236]. We have studied I - V response of quantum dot CdS/Ag junctions at low (50 -700 Hz), medium (1 -50 KHz) and high (1.2 - 5 MHz) frequency ranges. It was observed that for low frequency range, the current density was around 150.41 A/m^2 which did not vary significantly while changing signal frequency from 50 Hz to 700 Hz.. Figure-47 depicts mid-frequency response which predicts that current establishment begins at 127.52, 62.6, 200.95, 129.86 and 31.63 mV corresponding to 1, 5, 10, 20 and 50 KHz, respectively. The rate of current

rise is maximum for an applied voltage of 31.6 mV and an A.C. signal of frequency 50 KHz (figure-47 and table-17). The linear rise of current growth indicates faster charge decay phenomena of quantum dots as signal frequency improves from 1 to 50 KHZ. Thus, at higher frequencies quantum dots behave as conducting channels for current conduction. The applied voltage corresponding to rapid increase of current is showing oscillatory nature possibly due to large inhomogeneity in CdS quantum dots.

Investigations in the high frequency (1.2 - 5 MHz) region showed that the current in the case of the quantum dot CdS/Ag junctions rises rapidly above 0.3718 mV at a frequency $f = 1.2$ MHz. On linear extrapolation of data

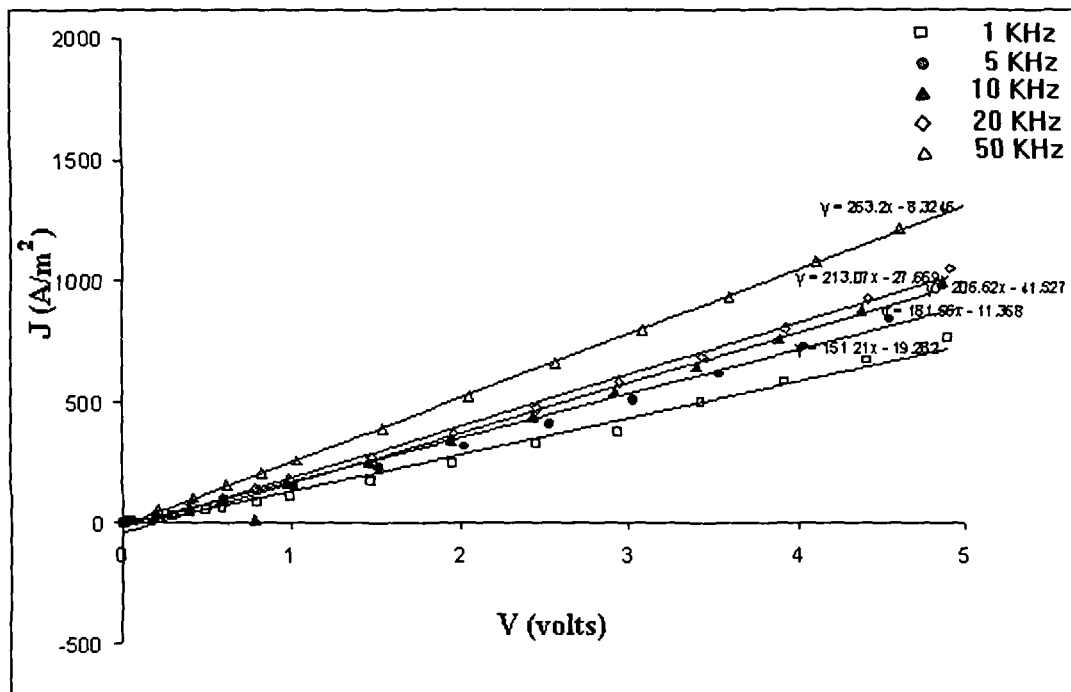


Figure 47. $I - V$ response of CdS/PVOH quantum dots ($f = 1- 50$ KHz)

Table 17. Frequency (MHz) dependent current growth of CdS/PVOH quantum dots

Frequency (KHz)	Rate of current growth (Ohm/m ²)	Applied voltage (Point of sharpest rise in current) (mV)
1.0	151.21	127.518
5.0	181.58	62.606
10.0	206.62	200.9486
20.0	213.07	129.8587
50.0	263.2	31.6284

points we obtain that for higher signal frequencies current is established even for negative potentials. The curve fitting gives us those values to be -0.1057, -0.9745, -0.3184, -1.5874, -2.2163 and -3.276 mV against frequencies 1.5, 2.2, 2.4, 3.5, 4.2 and 5.0 MHz, respectively. The maximum rise of current is found to be established at 3.5 MHz with a rate of 2733.2 (mho/m²) while least rate is 1063.8 (mho/m²) at a frequency $f = 1.2$ MHz. One important conclusion may be drawn by observing table-18 that for MHz ranges, current establishment can take place even if the quantum dot sample is under negative potential difference. This suggests carrier injection from the surface traps (which are inherent in quantum dots due to extremely high surface-to-volume ratio) plays a dominant role in establishing current at higher frequencies.

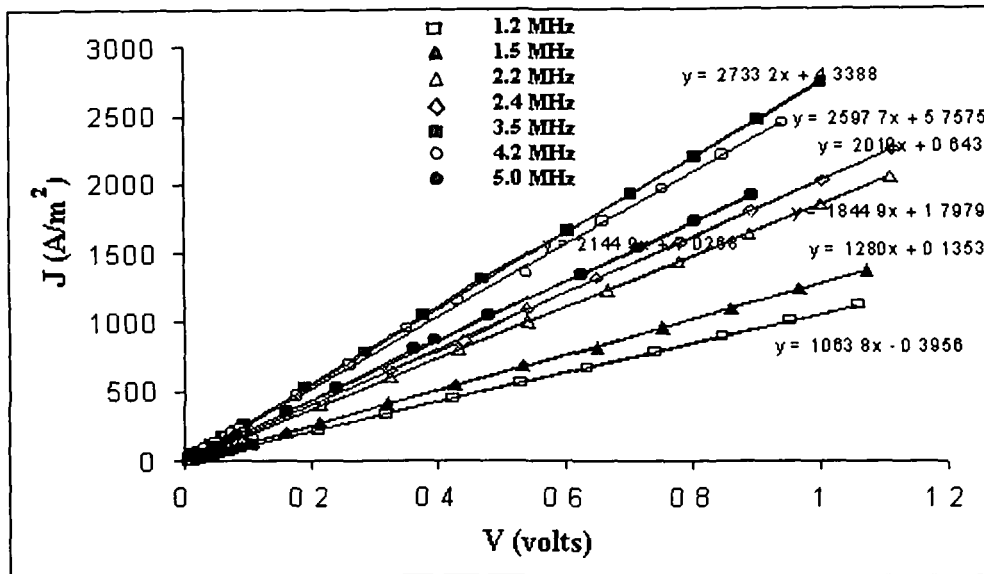


Figure 48. *I - V* response of CdS quantum dots ($f = 1.2$ to 5.0 MHz)

Table 18. Frequency (MHz) dependent current growth of CdS/PVOH quantum dots

Frequency (MHz)	Rate of Current Growth (Ohm/m ²)	Applied Voltage (Point of sharpest rise in current) (mV)
1.2	1063.8	0.3718
1.5	1280	-0.1057
2.2	1844.9	-0.9745
2.4	2019	-0.3184
3.5	2733.2	-1.5874
4.2	2597.7	-2.2163
5.0	2144.9	-3.276

6.3.2 Capacitance-Voltage ($C - V$) analysis

The $C - V$ characteristics of quantum dot CdS/Ag interfaces were studied and analyzed at low (50 - 700 Hz) frequency range, medium (1 - 50 KHz) frequency range and for high (1.2 – 5.0 MHz) frequency range. For low frequency values (50 - 700 Hz) capacitance of the junction increase steeply in consistency with earlier report for CdS/Au junctions [236].

Referring to figure-49, It is noticed that as frequency rises the steepness falls down significantly. In fact, (i) for higher forward bias, there is large contributions from high density of surface/interface traps, and (ii) for low bias values, imply only a small contribution from surface traps. A high density of surface traps may lead to injection of minority carriers into the neutral zone, which in turn gives additional diffusion capacitance besides the normal depletion layer contribution. Thus, the junction capacitance can be written as

$$C_j = C_{dep} + C_{diff} \quad (80)$$

Further, the rearrangement of these injected minority carriers do not take place instantaneously and also become frequency dependent. For frequencies above the characteristic frequency of the recombination processes, these injected excess minority carriers are probably not able to follow the a.c. signal and the C_{diff} contribution to C_j is mainly from the depletion layer. It can be noted that the contribution to C_j at 50 Hz in high forward bias regime, is significant but decreases with increasing frequency. At higher frequencies, C_j attains saturation implying that the domain

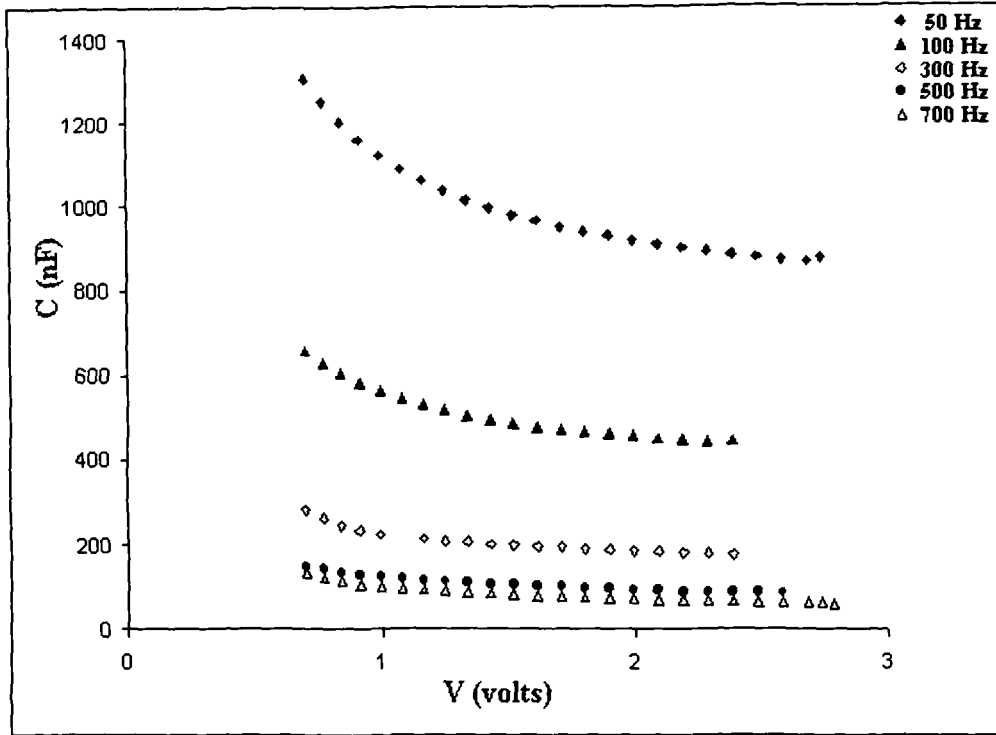


Figure 49. $C - V$ response of CdS/PVOH quantum dots (50 - 700 Hz)

contribution to C_j is from the depletion layer. The overall feature shows a frequency dispersion relation. Mott-Schottky hetero nanojunctions have been reported in case of metal-superconductor-semiconductors [237]. The frequency dispersion, can be discussed through the Mott-Schottky relation for a nano-CdS/Au junction given by [236,238]

$$\frac{1}{C_{dep}^2} = \frac{2}{q\epsilon_0\epsilon_s n_d} (V + V_{bi}) \quad (81)$$

where the quantities ϵ_0 , ϵ_s , n_d , V_{bi} and C_{dep} are permittivity of the free space, the dielectric constant of the semiconductor, the donor concentration (CdS is an n-type semiconductor), the built in potential and the depletion layer

capacitance, respectively. Therefore, one can go for Mott-Schottky response ($1/C_{dep}^2$ vs V) to obtain built in potentials.

Figure-50 represents $C - V$ response of the CdS quantum dot sample for mid frequency range (1 - 50 KHz). It is clear that contrary to low range frequency values, capacitance increases enormously with applied voltage. But the rate of increment drops as frequency rises and tends towards saturation at higher frequencies. For, 1 KHz, capacitance attains higher value due to charging of the quantum dots and thus, possess least value of current (table-17) with respect to higher frequencies. PVOH embedded CdS

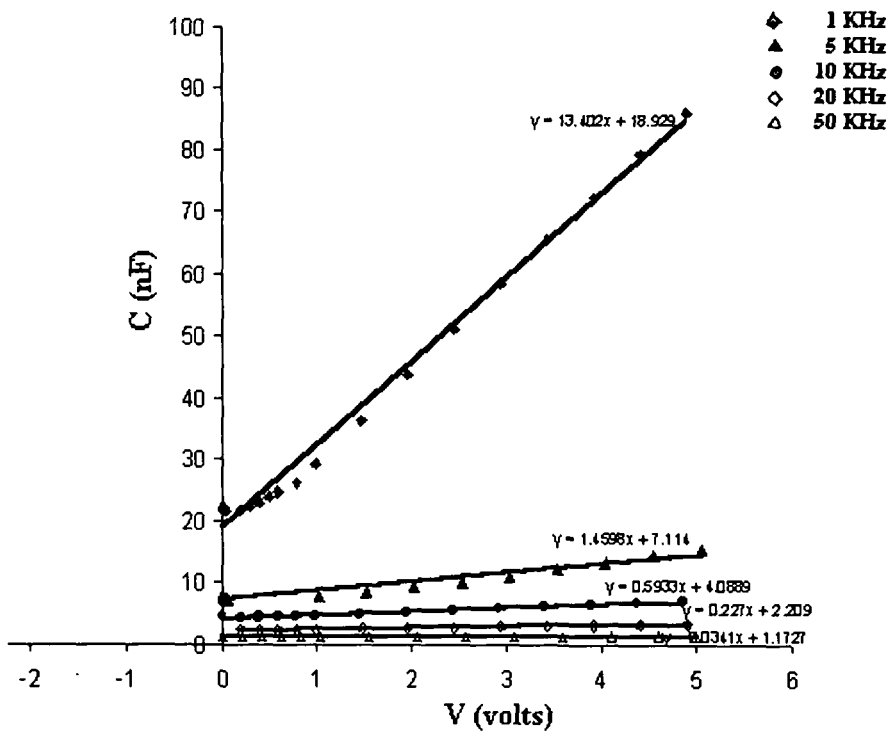


Figure 50. $C - V$ response of CdS/PVOH quantum dots (1-50 KHz)

quantum dots collectively behave as a capacitor to store charge, suppressing the chances of charge flow (current) from one terminal to the other. However, for the case of very large frequencies (1.2 - 5 MHz), the $C - V$ response shows a great extent of nonlinear patterns. Figure-51 explains that the $C - V$ response is nonlinear in the low forward bias regime and then becomes linear in the intermediate regime corresponding to frequencies 1.2, 1.5, 2.2 and 2.4 MHz. The nonlinearity starts rising from 2.4 MHz and attains a maxima corresponding to $f = 4.2$ MHz. It is important to quote that, inspite of observation of nonlinearity at both extremes, sample shows linear

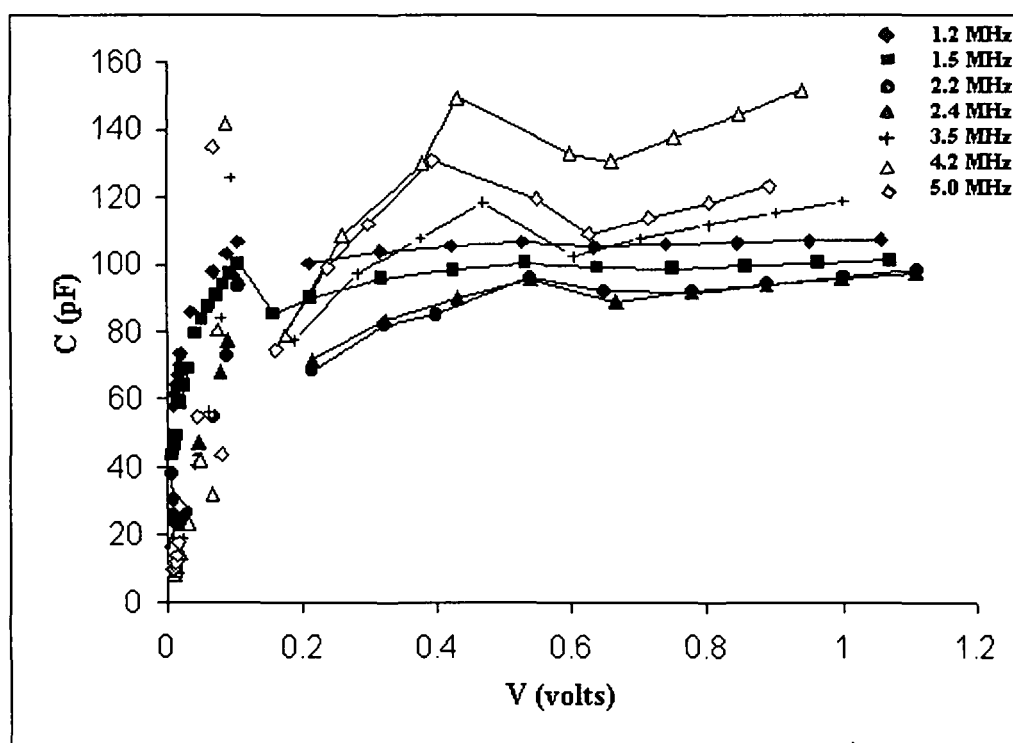


Figure 51. $C - V$ response of CdS/PVOH quantum dots (1.2 to 5 MHz)

$C - V$ response in the mid-frequency range of applied voltage. In other words, formation of Schottky barrier is complete at high frequency ranges.

The nonlinear nature corresponds to charging and discharging process within a given range of forward bias. Moreover, these nonlinearity ensures application in single electron device junction diodes etc. The increase in capacitance of the heterojunctions with increase in photon dose is due to increase in carrier concentration across the junction during photoexcitation has been reported. Thus far we have observed both for KHz and MHz ranges where charging starts even when applied voltage is of the order of a few millivolts. Hence, embedded CdS quantum dots can be used as passive elements e.g capacitors etc. to justify the name of men made charge droplets [23,239].

6.4 Photon induced charge transport phenomena in quasi-arrayed ZnS quantum dots

Electron transfer from confined structures like quantum film, quantum wire or quantum dot have been studied in conjunction with photo-excitation [240,241]. This section highlights upon photocurrent generation in the external circuit due to electron transport within the self organized ZnS quantum dots by means of tunneling through the thin dielectric polyvinyl matrix. Along with current decay characteristics, the nonlinear nature of charge transport as a function of bias voltage in presence of incident high power photons are discussed. As a possible application in single electron transistor (SET) we claim that the signature of coulomb blockade is observable within 19.5 mV for quasi-arrayed quantum dots (~ 50 nm) under pulsed photon induction.

6.4.1 Test bed to observe single electron effects

A 10 μm Cu mesh (usually used as grid in transmission electron microscope (TEM)) having 200 square loops was placed firmly over an insulating glass substrate. As shown (figure-52), one pin pointed end of 99.99% pure fine silver wire (diameter ~ 15 μm) was fixed into one arm of a single mesh with the help of a binocular polarizing microscope. By means of a syringe a single tiny drop of the quantum dot sample was gently placed over the respective mesh in such a way that the sample just spills over the opposite arm to build adequate microcontact. The specimen was dried

naturally to stick upon the grid. Then, another pin pointed Ag wire was fixed over the sample to the opposite (virtual) arm of the same mesh. Then, it was masked to protect the same from the environmental attack. The free ends of the probe wires are connected through a 1.2 K load and to a bias source followed by a current meter in series. The current meter was zero adjusted at every bias voltage before exposing the sample to laser pulses and sufficient time gap was allowed to avoid unwanted error due to fluctuations while making the biasing step. Care was taken to prevent undesired error in measuring current due to improper insulation of the wires or presence of

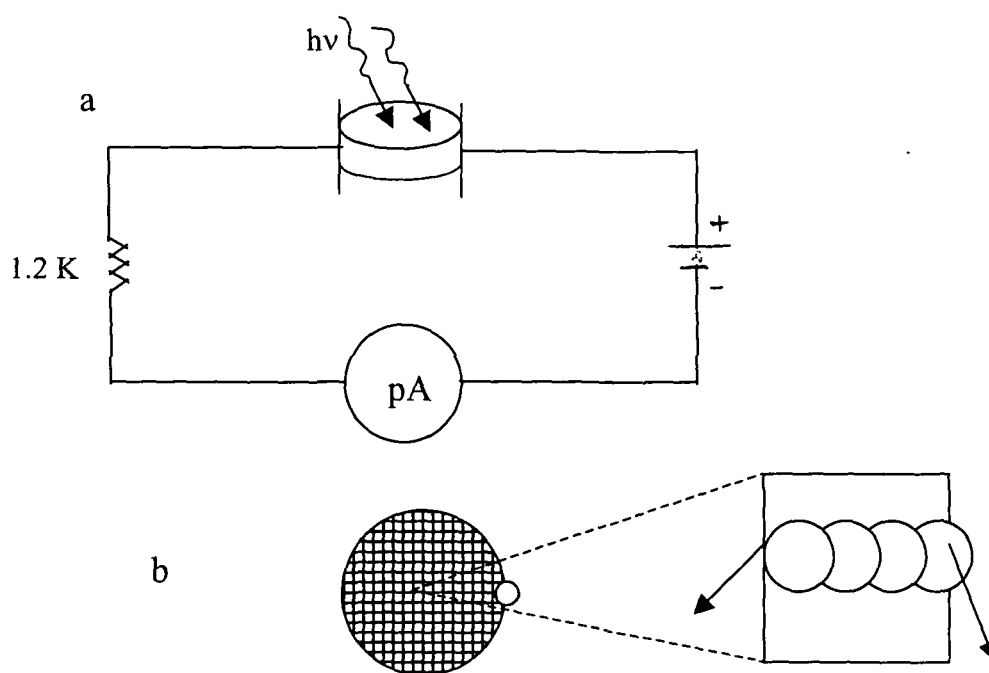


Figure 52. (a) Profile of a test bed and circuit to observe single electron effects (b) TEM grid used to hold ZnS quantum dots, arrow marks represent probe leads

other electromagnetic sources. The Nd:YAG laser ($\lambda = 1064$ nm) was used as the excitation source and the experiment was carried out using photons of ~ 6 ns pulse width and taking fourth harmonic beam ($\lambda = 266$ nm, $E = 4.67$ eV). The whole arrangement was made in a dust free, dark chamber to improve accuracy of the experimental setup.

6.4.2 Photocurrent generation due to carrier transport

Let us consider a regular quantum dot sample where quantum particles are supposed to be arranged like lattice atoms. It is noteworthy to mention here that the periodicity of the dots which is likely to be perturbed under the influence of continuous laser irradiation remains unaltered for pulsed photons. Now, when a high frequency pulsed light beam is allowed to fall over the sample which is micro-probed between two terminals then it tends to excite the first pair of electrons of a given quantum dot and under proper biasing, the electrons can be allowed to move through infinitely thin dielectric medium (figure-52,53). And so, one would expect photoelectric current due to photoelectron transfer from one terminal to the other. It has been established that when nanoparticles of different E_g are in contact, charge transfer is possible from the conduction band of the wider band gap material to that of narrow band gap material. A few representative examples are CdS/ZnO, CdS/Ag₂S, CdS/TiO₂, ZnS/ZnO [241].

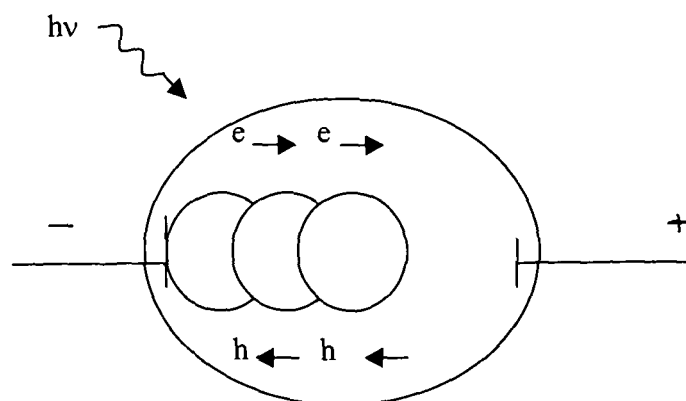


Figure 53. Schematic of photon induced carrier transport phenomena

In our case, because the single square loop of the mesh is of ~ 200 nm dimension so, a maximum of 4 quantum dots (each 51 nm, revealed from HRTEM) are expected to fill the mesh along the principal axis (figure-53). If there is any depart from this quasi-arrayed structure, then carrier transport due to single quantum dot linked to virtual arm would be feasible. The presence of surface states / traps are found to enhance the interfacial charge transfer in the nanocrystallite systems [241]. In our case, as the polymer matrix is a nonconducting polymer ($\rho \sim 10^{14}$ ohm-m) so total photo-generated current contribution is solely due to the inter quantum dot carrier transport through the dielectric matrix. Again, since the biasing energy gap structure is assumed to be slanted, the photo-excitation stimulate the transport process unto the external circuit.

We take energy of the laser to be $h\nu = E_{1e} + E_{1h} + E_{gap} - E_B$ and assume that at most two excitons can be created in the lowest energy state, while the higher states corresponding to $E_{n>1}$ stay empty ($E_g = 3.7$ eV and $h\nu = 4.67$ eV). The binding energy E_B includes the coulombic interaction between the electrons and the holes and may be regarded as a correction to the single particle states. For mathematical relevance one can assume identical dots arrayed along X-axis as shown in figure-53.

Quantum dots are devices capable of holding or releasing charges [23]. When relatively high potential barriers separate the dot from a source and drain the number of electrons on the dot, N , is a well defined integer. When the sample is being excited by a pulse one exciton per dot is created. Any electron movement to the dot requires the number to be changed by one. A finite amount of energy is required to add an electron against e-e coulombic repulsive force. According to constant interaction model [23] Coulomb interaction between the electrons is independent of the number of dots i.e. N and is described by the capacitance C of the dot. The additional energy required to add an electron to a quantum dot is given by

$$\begin{aligned} E_{add} &= (N + 1) e^2 / C - Ne^2 / C + \Delta E \\ &= e^2 / C + \Delta E \end{aligned} \quad (82)$$

where ΔE is the energy difference between two quantum states. One can obtain capacitance C of identical dots by putting $E_{add} = eV = e^2 / C + \Delta E$. After irradiating the sample with pulse $h\nu$,

$$h\nu + E_{add} = e^2 / C + \Delta E + E_B \quad (83)$$

$$1/C = 1/e^2 [hv + E_{add} - E_B - \Delta E]$$

or, $1/C = 1/e^2 [E - \Delta E]$ (84)

where $E = hv + E_{add} - E_B$ defines the net energy supplied to each quantum dot per nanosecond pulse at a given bias voltage. Considering exciton formation at the lowest energy state so that $\Delta E = 0$, and putting exciton binding energy E_B for ZnS to about 40 meV we have estimated average capacitance of the individual quantum dots. C vs E plot (figure-54) illustrates that the C value drops appreciably with respect to rise in biasing voltage (as only biasing energy affects E in the equation-84). In otherwords, when higher bias voltage value is considered, then the quantum dots are unable to hold more charges (that is why capacitance falls) and becomes conducting channel for smooth carrier conduction. The same event is shown by high value of current in current decay plot (figure-54).

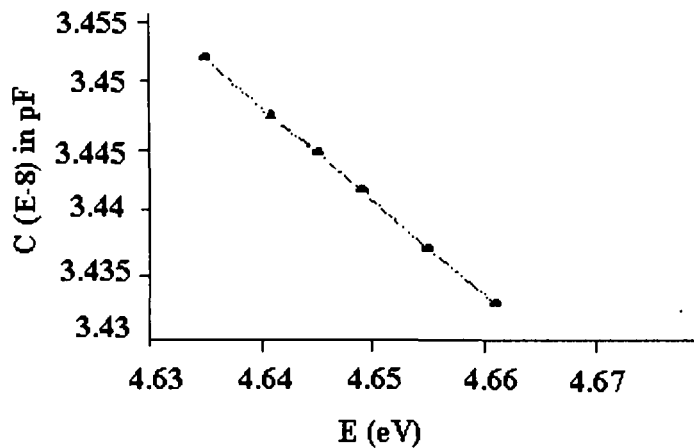


Figure 54. Capacitance vs energy supplied to quantum dots

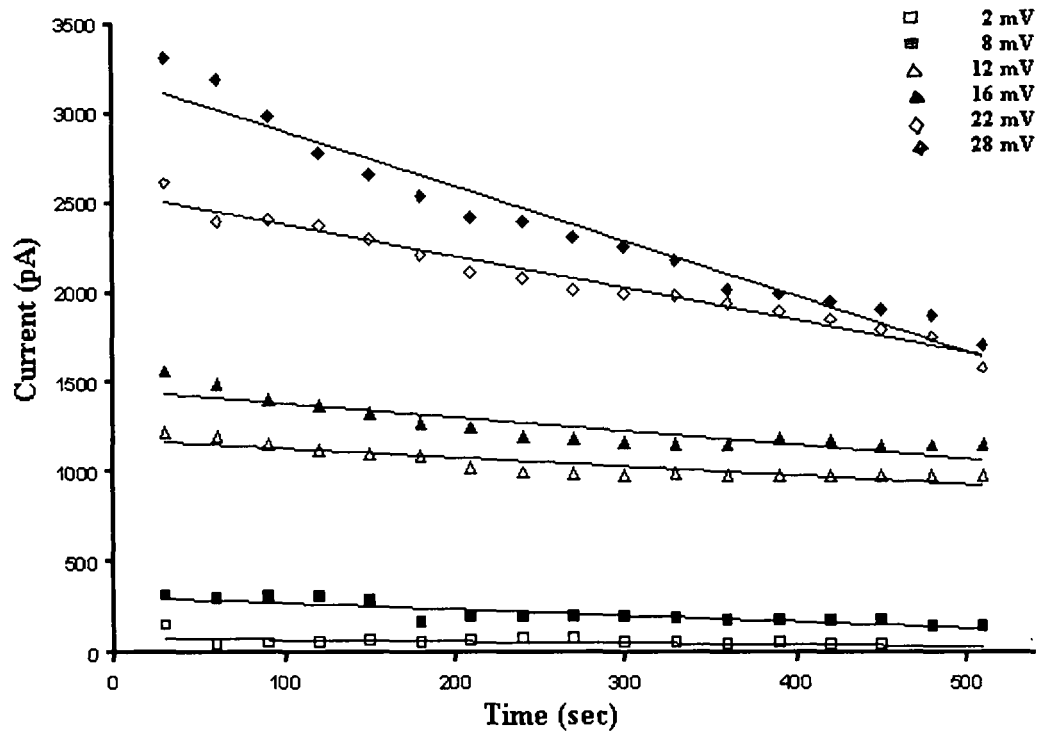


Figure 55. Current decay response of ZnS quantum dot sample

Moreover, it describes the stability nature of the current through the sample over significantly large range of time. The readings of photocurrent were taken after every 30 sec. time interval. It was observed that with increase in bias voltage to the sample circuit there is significant rise in photogenerated current which decays with time in each step. But, the nature of decay depends upon the amount of supplied bias voltages. It means, sample's photoconductivity property is suppressed due to perturbation in the periodicity of the regular quantum dots. Moreover, it is evident from the plots that for lower bias voltages upto 12 mV, photo-generated currents show

stabilized signature upto several hundreds of seconds. In these case of bias voltages decay and growth both compete each other to give stabilized signatures and conversely, at high bias values (for 22 and 28 mV) decay is dominating over growth no matter how one applies pulse at any subsequent step of time. We believe that the presence of internal field due to the presence of excited electrons (which do not take part in the transport process but have finite mobility in the external field direction) stabilize the charge transportation for a significantly large time period. Moreover, low bias situations reveal that all the electrons participate in the process of transport phenomena and so there is sharp fall in current with respect to the preceding bias step.

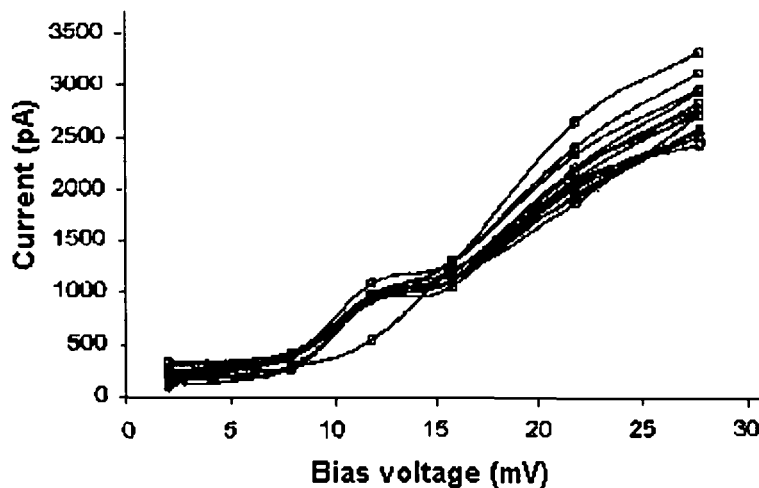


Figure 56. Nonlinear $I - V$ response of photon induced ZnS quantum dots

Figure-56 shows nonlinear response of $I - V$ characteristics. Due to highly asymmetric barriers, the voltage mainly drop across one of the barriers and current changes appear in the $I - V$ plot as pronounced steps; a situation described as Coulomb staircase reported by earlier workers [242,243]. A close look at the plot explains that as one goes on rising bias value, conductance falls rapidly and is maximum for the highest value i.e. 28 mV. Therefore, we claim that the polymer embedded ZnS quantum dot sample is able to work in the stable conductance zone over a large period of time shown by the linear regime of the same plot.



CHAPTER-7

CONCLUSION & FUTURE DIRECTIONS

CHAPTER-7

CONCLUSION AND FUTURE DIRECTIONS

We are successful in embedding various II-VI semiconductors namely CdS, ZnS and ZnO on polymer matrices. We notice formation of extremely small particle range down to ~ 2 nm in case of CdS quantum dots on polyvinyl alcohol. ZnS quantum dots bearing average size ~ 50 nm and so interparticle separation is unusually small. The average size of quantum dots was measured by using Scherrer formula to X-ray diffraction patterns and were confirmed from TEM images. Next, we have surveyed role of surface states in suppressing the recombination emission through thermo luminescence study. The optical absorption spectra provides information of blue shift and gives strength to formation of particles in nanoscale range. We took CdS: PVOH into different molar ratio and found that 3:1 ratio is more appropriate to notice a number of excitonic transitions (table-4). Again, CdS quantum dots ensures high fluorescence activation to an amount of 92% which is less in contrast to ZnS where the efficiency is only ~ 15%. Also, we observe for Mn doped ZnS there is significant yellow emission due to delocalized electrons of Mn^{+2} in consistency with earlier workers [124].

We have made an extensive study over CdS quantum dots while encountering for the existence surface phonons. We have noticed presence of unusually high value of coupling constant 'S' i.e. ~ 11 (table-5) and argue that there might be stronger electron phonon coupling in nanoparticle

systems with respect to their bulk counter parts. Asymmetrically broadened Raman peaks indicate possibility of confinement of phonons in addition to electron confinement. We expect the cause of asymmetry due to inhomogeneity of particles or presence of surface modes which generally exist in the low frequency of the longitudinal optical modes (LO). Therefore, to get exact information we have digitized the Raman spectra as it is and found that even surface phonons are confined due to existence of a few discrete modes, which are in close approach to those of standard theory of surface modes. We also highlight why such SO modes disappear when the specimen is in air or in aqueous form.

Swift heavy ions are the means to form ion tracks in materials (polymer, semiconductor, superconductor etc.). But when a semiconducting particle is in embedded form what physical phenomena would come to the forefront ? To explore this we have selected chlorine beam of energy 100 MeV for irradiation experiments. Chlorine ion was chosen for bleaching action over unwanted impurities. We found strong redshift in the absorption spectra of ion induced ZnO/PVOH and CdS/PVOH quantum dots which is stronger with respect to increase in ion fluence and expect that there might be grain growth due to ostwald ripening under ion irradiation. However, for CdS/SBR we found grain bursting effect and predict that SBR being a flexible polymer (elastomer with cis- trans states) dissipates the heat caused by ion irradiation into whole sample faster than the case of PVOH matrix. Moreover, photoluminescence of Mn doped ZnS depicts with increase in ion

fluence there is significant enhancement in the fundamental emission which normally observable at $\lambda = 480$ nm for ZnS quantum dots. With Mn doping, it shifts to 405 nm and shifts upto 375 nm for heavily irradiated quantum dots. As with increase in ion fluence, grain growth occurs (table-12) and therefore, luminescence on higher energy scale could not be possible due to size quantization (energy gap increases with size reduction). As irradiation leads to surface smoothing which in turn reduces number of surface traps, contribution from widely separated deep traps may be one of the cause of luminescence improvement. The exact cause needs further investigation. The fundamental emission shifts towards blue keeping yellow emission (due to Mn doping) almost unperturbed.

A few of the quantum dot samples are applied to explore nonlinear optical and electronic properties in view of future prospects.

First, we have noticed remarkable fluorescence activation in ion irradiated samples but could not obtain information related to energy values due to fast scanning rate of the machine. Therefore, we had digitized the FL-spectra of virgin and irradiated CdS quantum dot samples and found that there exist significant amounts of thirdorder nonlinearity in the fluorescence activation process corresponding to the irradiated quantum dots.

Next, we have observed the transmission through CdS quantum dots which drops linearly with respect to incident intensity of 6 ns high power pulsed laser ($\lambda_{ex} = 1064$ nm). Also, we are successful in performing non-resonant non-degenerate four wave mixing and receiving phase conjugate

signals. We have determined existence of third order susceptibility $\chi^{(3)}$ of CdS/PVOH quantum dots even in the non-resonant case which is of the order of $10^{-14} \text{ m}^2/\text{W}$. Thus, exploiting the intensity-dependent change in the refraction coefficient, third order nonlinearities could be determined by non-resonant non-degenerate four wave mixing. Already extensive study on obtaining third order nonlinearity due to Raman and Brillouin scattering and degenerate four wave mixing [215] have been found in literatures.

Controlling single electron tunneling phenomena in nanostructured materials is gaining interest, because of its importance in developing extremely small electronic devices with high speed and low power consumption. When the size of the junction becomes small enough to have extremely small capacitance, C , the charging energy resulting from a single electron at the junction, $w = q^2/2C$, becomes larger than the thermal energy $k_B T$, thus preventing additional electron injection to the junction [243]. Assembling a semiconductor junction using $\sim 1\text{-}2 \text{ nm}$ nanoparticles results in the construction of single electron devices that can be operated at room temperature [201,202]. Alivisatos [244,245] has reported interesting results showing the future possibility of applying colloidal semiconductors to single electron transistors.

In this context, we propose that photo-electron transfer study could be an idealized study to probe nanoparticles when they are separated by thin dielectric wall under proper biasing condition. We have chosen quasi-arrayed

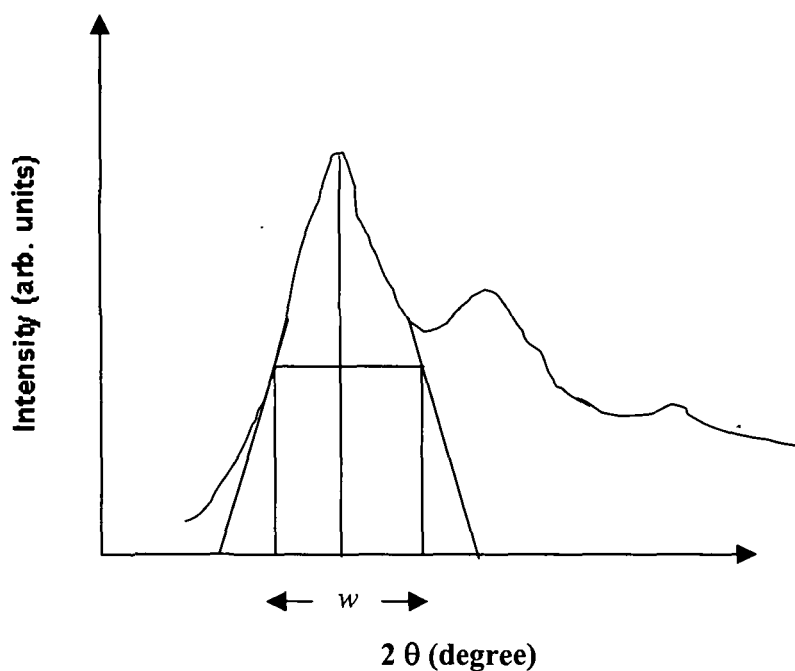
ZnS quantum dots for investigations having interparticle separation about 4 nm only and quantum dot size is relatively large (~ 50 nm). It was observed that one could generate uniform photocurrent in the external circuit at sufficiently low bias values and pulsed photon induced defect study may be suggested at higher bias voltages. In addition to environmental stability, charge holding capacity of the quantum dot sample is an important issue for potential applications in passive and active electronic devices. In this connection, photocurrent generation due to ultrashort pulses and their nature of decay has been discussed. The nonlinear carrier transport through quantum dots was viewed in $I - V$ characteristics. Thus, photon induced single electron effects are experimentally observed at room temperature when quantum dots are quasi-arrayed and separated by thin dielectric wall. Single electron devices e.g. single electron transistor works on the basis of single electron effects and such events are observable in extraordinary circumstances (low temperatures). Single electron transport expected from the lateral confinement of quantum dots by electric fields might be a promising basis for binary logic operation and all optic switching interconnects [246-248]. When, one exploits the nonlinear change of absorption or refraction, an optical Kerr shutter or Q-switch may be realized [222]. So, an intensive discussion is required for the practical implementation of semiconductor quantum dots, for example, as passive and active elements in integrated optics. The search for 'figures of merit' for the different materials to facilitate the best choice from a multitude of suitable substances

and, on the other hand, the development of entire device concepts favouring new materials, which are promising in the permanent competition with the advances in silicon technology. Special interest is dedicated to the role of quantum confinement and its influence on the nonlinear optical properties which could bring new application feasibilities. Because in comparison with other compound semiconductors, II-VI semiconductors possess high value exciton binding energies (and that is why excitonic absorption can be visible at room temperature) and therefore, further research is called for in the areas of single electron devices, fast optical switching, wave guiding and lasing with tenability over a wide spectral range etc.



APPENDIX

APPENDIX-1



Scherrer formula:

$$d = \frac{0.9\lambda}{w \cos\theta}$$

where w is full width half maxima (FWHM) of XRD pattern shown above, d is average size of the particles, θ is diffraction angle and λ is wave length of the x-ray source used.

~~~~~

## APPENDIX-2

### Digitization process used

The optical absorption spectra (OAS) plots and fluorescence spectra (FL) plots and Resonance Raman spectra plots are scanned in a scanner. The scanned image is opened by a standard imaging software, Adobe PhotoDeluxe<sup>®</sup>. The image is converted to a negative so that now the black plot on white paper background becomes a white plot on a black background. A rectangular area of the image is cut out and saved. The bottom edge of this rectangle exactly coincides with the x-axis of the plot and the left edge coincides with the y-axis. The saved image is opened in MATLAB<sup>®</sup>, which converts the image into a rectangular matrix, where the value of each matrix element represents the intensity value of the corresponding picture element of the rectangular image. Obviously the bright points representing the plotted line in the rectangular image yield high values in the corresponding matrix elements. The distances from these high value points to the bottom edge of the rectangular image are taken as the parameters for digitization. The following MATLAB<sup>®</sup> routine does this digitization and writes the digital data in an output data file. The data can then be analyzed by opening the data file by any spreadsheet software like Microsoft Excel<sup>®</sup>.

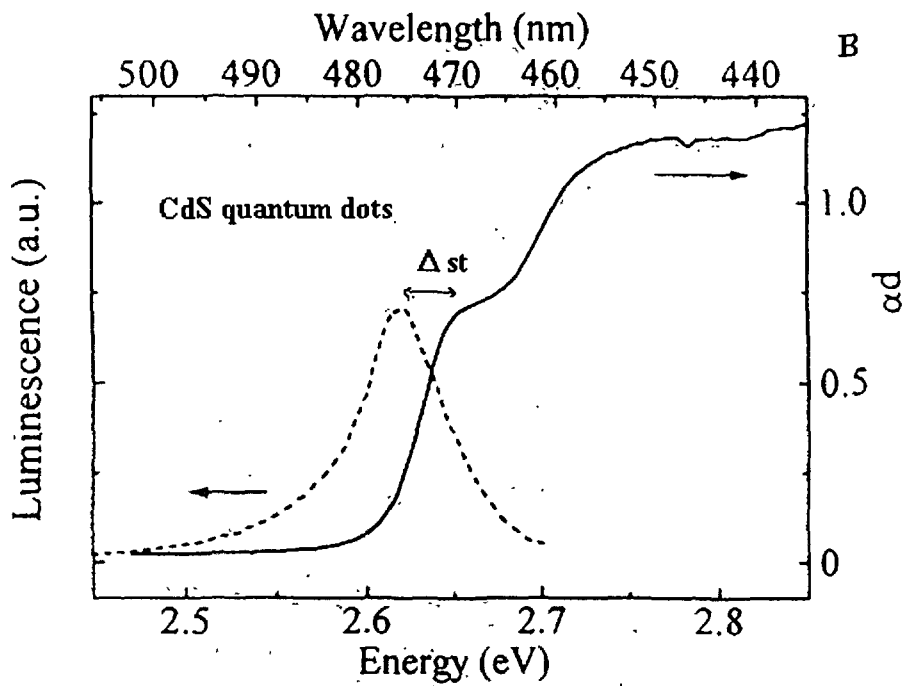
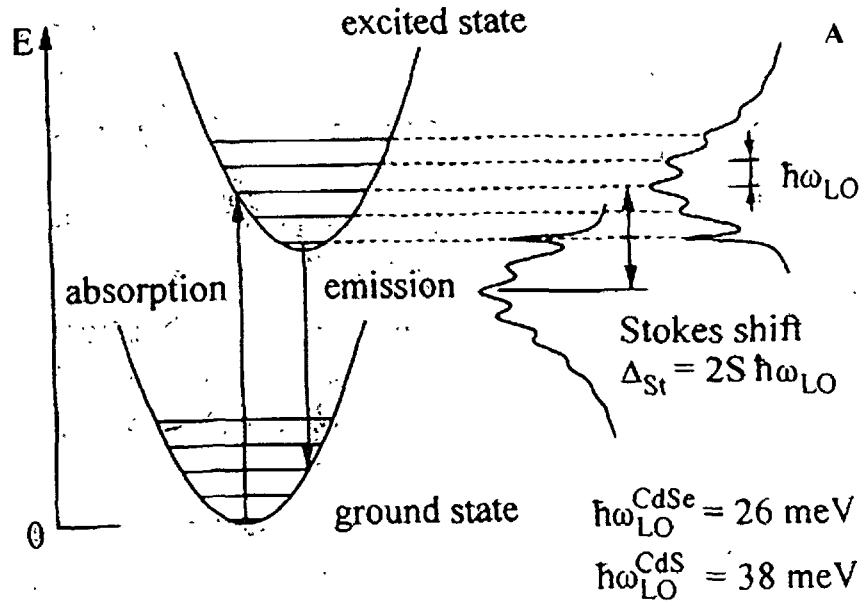
```
clear
a1=(531:-1:1);
a1=a1';
b1=a1;
for n=1:912
    b1=[b1 a1];
end
c1=imread('dp1.bmp','bmp');
c1=im2bw(c1,0.4);
```

```
c1=[c1];  
c1=double(c1);  
d1=b1.*c1;  
e1=max(d1,[],1);  
etemp=max(e1);  
e1=[e1./etemp];  
e2=e1';  
wk1write('c:\mydocu~1\dw1',e2)
```

The parameters in the program that are to be rewritten for every image digitized are the image name, matrix row and column numbers and the output data filename. The size of the matrix is found by using the MATLAB<sup>®</sup> command `imfinfo (image name)`. In the above case, the number of columns of the image , that is 531, is entered in line 2, the number of rows are entered in line 5, the image name is entered in line 8 and the output data filename is entered in line 17.

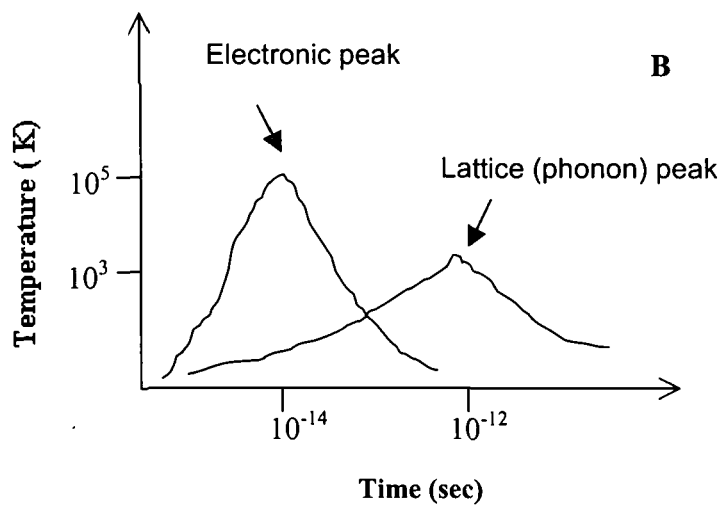
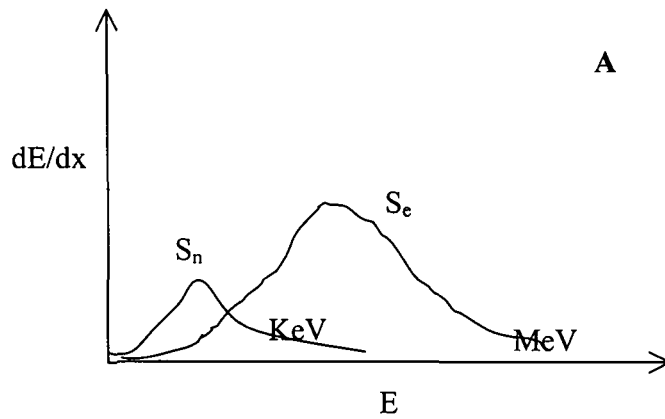
~ ~ ~

### APPENDIX-3



- A) Scheme of the Franck-Condon model
- B) Emission and absorption response of CdS quantum dots [222]

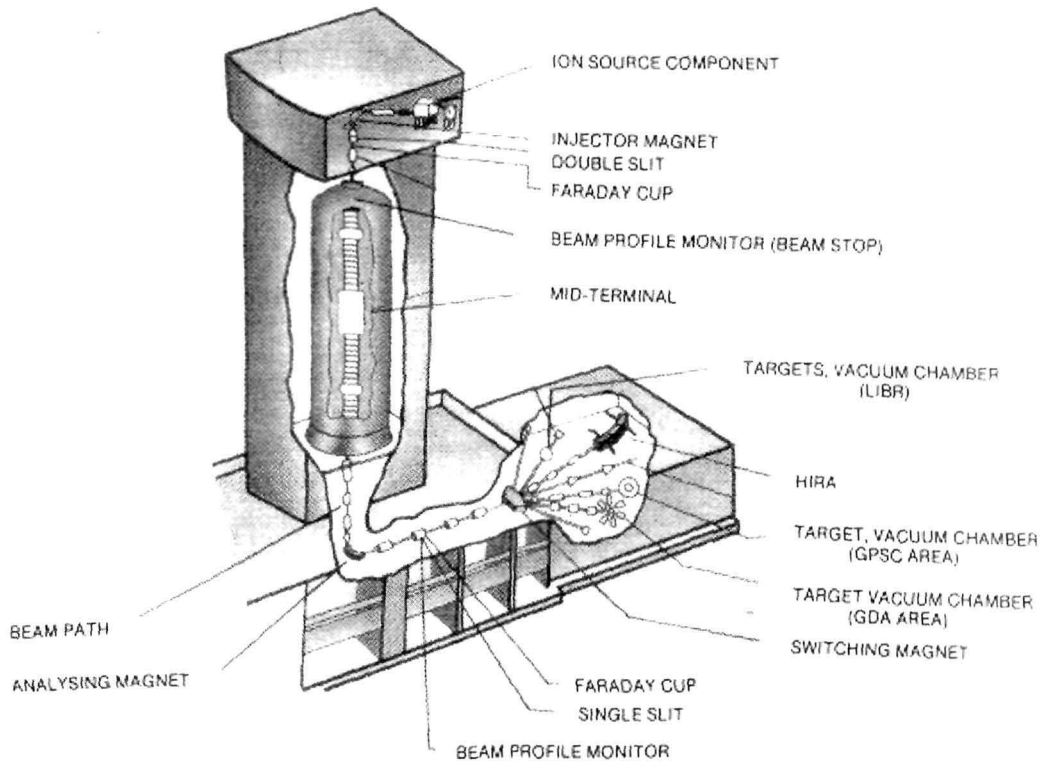
## APPENDIX-4



- A) Electronic energy loss ( $S_e$ ) and nuclear energy loss ( $S_n$ ) response of swift heavy ions through matter (not to scale)
- B) Evolution of electronic and lattice temperature rise with time (not to scale)

~~~~~

APPENDIX-5



SCHEMATIC OF ION IRRADIATION CHAMBER AND ION TRAJECTORY (Nuclear Science Centre, Aruna Asaf Ali Road, New-Delhi-110 067)

Chamber used: Material science

Ion Used: Chlorine

Charge state: +9

Current: ~ 1 pA (particle nano-Ampere)

Energy: 100 MeV

Fluence: 1×10^{11} , 5×10^{12} , 5×10^{12} and 1×10^{13} ions/cm²

Calculation of critical fluence (ϕ_c) : The knowledge of critical fluence is important in the sense that over dose irradiation might spoil the sample on hand , while low dose would not provide appreciable change in characteristics. It has been known that with electronic energy loss beyond nuclear energy loss ($S_e > S_n$) heavy ions in materials form ion tracks of radius ~ 5 nm. And so one can determine ϕ_c for a sample of 1×1 cm².

Area exposed per ion:

Total area to be exposed:

$$a = \frac{\pi}{4} \times 25 \times 10^{-18} \text{ m}^2$$

$$A = 10^{-4} \text{ m}^2$$

So, if N be number of ions required to expose the whole specimen then,

$$N = \frac{A}{a} = \frac{4 \times 10^{-4}}{\pi \times 25 \times 10^{-18}} \approx 5 \times 10^{12} \text{ ions}$$

Therefore, ϕ_c must have a value of $5 \times 10^{12} \text{ ions/cm}^2$ and our natural choice would be slightly higher or lower than this value to expose the whole area of the samples and thus to obtain better information out of the samples.

The selected fluences: 1×10^{11} , 5×10^{12} , 5×10^{12} and $1 \times 10^{13} \text{ ions/cm}^2$

Relation between enA and pnA:

enA is electrical nano-Ampere where as *pnA* is particle nano-Ampere.

$$1 \text{ pnA} \sim 6.25 \times 10^9 \text{ particles / sec}$$

e.g. $enA = 1 \text{ nA}, q^+ = 1$

then,

$$pnA = \frac{enA}{q^+} = \frac{10^{-9} \text{ Coul / sec}}{1.6 \times 10^{-19} \text{ Coul}} \approx 6.25 \times 10^9 \text{ particles / sec}$$

$$\text{Counts} = \frac{Dqe}{S^*}, \text{ where}$$

$D \rightarrow$ dose

$q \rightarrow$ charge state

$e \rightarrow$ electronic charge ($1.6 \times 10^{-19} \text{ Coul}$)

$S^* \rightarrow$ scale of the counting machine

~~~

## **APPENDIX-6**

### **Specifications of the hi-power laser used for wave mixing phenomena**

*Laser used:* Quanta-Ray INDI (Spectra Physics)

*Umbilical length:* 3 m

*Operating voltage:* 190-260 V, single phase, 50/60 Hz

*Electrical service:* 10 Hz = < 12 A; 20 Hz = <15 A

*Output characteristics:-*

*Pulse width:* 6-7 ns

*Divergence:* 0.5 mrad

*Beam diameter:* < 10 mm

*Beam pointing ( $\pm \mu\text{rad}$ ):* 100

*Timing jitter ( $\pm \text{ns}$ ):* 0.5

*Energy stability ( $\pm \%$ ):* 2

*Power drift ( $\pm \%$ ):* 3

*Energy (max) :* 25 mJ

*Fundamental beam ( $\lambda$ ):* 1064 nm

### **Specifications of the silicon photodetector (photodiode)**

*Model:* SFH 203 FA

*Body length:* 8.6 mm

*Lead spacing:* 2.54 mm

SFH 203 / 203 FA are high speed photodiodes with SFH 203 FA combining an integral day light cut-off filter.

$V_R$ : 50 V

$I_{sc}$ : 25  $\mu A$

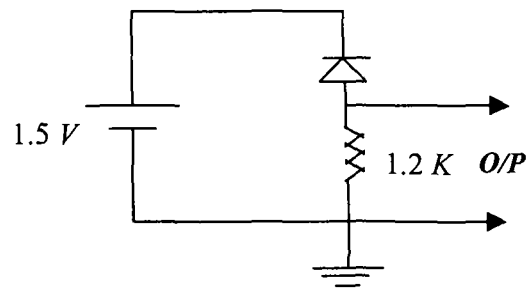
Power dissipation: 100 mW

Peak wavelength: 900 nm

Acceptance angle:  $40^\circ$

Operating temp.:  $-55^\circ C$  to  $+100^\circ C$

Rise/fall time: 5 ns



# REFERENCES

## REFERENCES

- 1 Drexler K E, *Engines of creation*, Oxford, 1990, UK; *Nanosystems*, John – Wiley & Sons, Inc. (1992)
- 2 Henglein A, *Topics in current chemistry*, 143 (1998) 113
- 3 Brus L E, *Appl. Phys. A* 53 (1991) 465
- 4 Wang Y and Herron N, *J. Phys. Chem.* 95 (1991) 525
- 5 Weller H and Angew A, *Chem. Int. Ed. Engl.* 32 (1993) 41
- 6 Weller H, *Adv. Mater.* 5 (1993) 88
- 7 Special issues on quantum dots, *Isr. J. Chem.* 33 (1993)
- 8 Henglein A, Bunsenges B, *Phys. Chem.* 99 (1995) 903
- 9 Yoffee A D, *Adv. Phys.* 42 (1993) 173
- 10 Kamat P V, *Prog. Inorg. Chem.* 44 (1997) 273
- 11 Alivisatos A P, *J. Phys. Chem.* 100 (1996) 273
- 12 Wang Y, *Acc. Chem. Res.* 24 (1991) 133
- 13 Bawendi M G, Steigerwald M L, Brus L E, *Annu. Rev. Phys. Chem.* 41 (1990) 477
- 14 Tolbert S H, Alivisatos A P, *Annu. Rev. Phys. Chem.* 46 (1995) 59
- 15 Gratzel M, *Heterogeneous photochemical electron transfer processes*, CP press: Boca Raton, FL (1989) p-87
- 16 Miller R J D, McLendon G L, Nozik A J, Schmickler W and William F, *Surface electron transfer processes* VCH:New-York (1995) p-31
- 17 Schmid G, (ed.) *Clusters & Colloids*; VCH:New-York (1994)
- 18 Kouwenhoven Leo, *Transport of electron waves and single charges in semiconductor nanostructures*, Ph. D thesis (1992)

- 19 Fukuda M, *Optical semicond. devices*, John Wiley & Sons, Inc. New York (1999) p-83
- 20 Ogawa T and Kanemitsu Y, *Optical properties of low dimensional materials*, World Scientific, Singapore (1995)
- 21 Scholl E, *Theory of transport properties of semiconductor nanostructures*, Chapman & Hall, London (1998)
- 22 Ashori R, *Electrons in artificial atoms*, *Nature* 379 (1996) 413-419
- 23 Kouwenhoven L and Marcus C, *Physics World*, (June-1998) p-35
- 24 Vander-Vaart N C, *Resonant tunneling through two discrete energy states*, *Phys. Rev. Lett.* 74 (1995) 4702-4705
- 25 Livermore C, *The coulomb blockade in coupled quantum dots*, *Science* 274 (1996) 1332
- 26 Blick R, *Phys. Rev. B* 53 (1996) 7899-7902
- 27 Fujisawa T and Tarucha S, *Superlattices & microstructures* 21 (1997) 247
- 28 Fujisawa T and Tarucha S, *Jpn. J. Appl. Phys.* 36 (1997) 4000-4003
- 29 Oosterkamp T H, *Artificial atoms and molecules on manybody effects & coherence in semiconductor quantum dots*, Ph. D. Thesis (1999)
- 30 Banyai L and Koch S W, *Semiconductor quantum dots: series on atomic, molecular and optical physics*, Vol-2, World Scientific, Singapore (1993).
- 31 Kayanuma Y, *Phys. Rev. B* 38 (1998) 9797
- 32 Efros Al L and Efros A L, *Fiz. Tekh. Poluprovodn.* 16 (1982) 1209 [*Sov. Phys. Semicond.* 16 (1986) 2555]
- 33 Henneberger F, Puls J, Spiegelberg Ch, Schulzgen A, Rossman H,

- Jungnickel V and Ekimov AI, *Semicond. Sci. Technol.* 6 (1991) A41-A50
- 34 Nanda J and Sarma D D, *J. Appl. Phys.* 90(5) (2001) 2504
- 35 Ram S et al. *Proce. of 10th Int. workshop on Physics of semiconductor devices* (1999) 1065-1068
- 36 Chemseddine A and Weller H, *Bunsenges Ber, Phys. chem.* 97 (1993) 636
- 37 Murray C B, Norris D J and Bawendi M G, *J. Am. Chem. Soc.* 115 (1993) 8706
- 38 Murti Y V G S, Nandakumar P and Vijayan C, *Physics Education*, Oct-Dec.(1999) p-229
- 39 Leobandung E, Guo L, Wang Y, and Chou S Y, *Appl. Phys. Lett.* 67 (1995) 938
- 40 Muranaka T, Jiang C, Ito A and Hasegawa H, *Thin Solid Films*, 380 (2000)189
- 41 Matsumoto K, Ishii M, Segawa K, Oka Y, Vartanian B J ,Harris J S, *Appl. Phys. Lett.* 68 (1996) 34
- 42 Sahu S N, Patel B, Behera S N and Nanda K K, *Indian J. Phys.* 74A(2) (2000) 93-97
- 43 Mahamuni S, Borgohain K, Bendre B S, Leppert V J and Risbud S.H, *J. Appl. Phys.* 85(5) (1999) 2861-2865
- 44 Edelstein A S, *Nanophase materials*, G C Hadjipanagis and R W Siegel (ed.) Kluwar Academic Publishers (1994) 73-80
- 45 Ramaswamy S, *Proce. of the Solid-state Physics Sympo.* 41 (1998) 30
- 46 Mandal S K, Chaudhury S and Pal A K, *Indian J. Phys.* 74A(2) (2000) 143-146
- 47 Pal A K, *Bull. Mat. Sci.* 22(3) (1999) 341-351

- 48 Song T K, Kim J and Kwyn S I, *Solid State Commun.* 97 (1996) 143
- 49 Hoon Sik Kim, Jae Hee Ryu, Binoy Jose, Byung Gown Lee, Byung Sung Ahn and Yong Soo Kang, *Langmuir* 17 (2001) 5817
- 50 Pokhrel M R, Janik K and Bossmann S H, *Macromolecules* 33 (2000) 3577
- 51 Yoon T S, Kwon J Y, lee D H, Kim K B, Min S H, Chae D H, Kim D H, Lee J D, Park B G, Lee H L, *J. Appl. Phys.* 87 (5) (2000) 2449
- 52 Classen W A P and Bloem J, *J. Electrochem. Soc.* 127 (1980) 194
- 53 Kato M, Sato T, Murota J and Mikoshiba N, *J. Cryst. Growth* 99 (1990) 240
- 54 Herron N, Wang Y and Eckett H, *J. Am. Chem. Soc.* 112 (1990) 1322
- 55 Mei G, *J. Phys: Condens. Matter* 4 (1992) 7521
- 56 Canham L T, *Appl. Phys. Lett.* 59 (1991) 3168
- 57 Maeda Y, Tsumkamato M A, Yazawa Y, Kanemitsu Y and Matsumoto Y, *Appl. Phys. Lett.* 59 (1999) 3168
- 58 Umehera A, Nitta S, Furukawa H and Nonomura S, *Appl. Surface Sci.* 119 (1997) 176
- 59 Melendres C A, Narayanasamy, Marani V A and Siegel R W, *J. Mater. Res.* 4 (1989) 1246
- 60 Fukui T, Ando S, Tokura Y and Toriyama T, *Appl. Phys. Lett.* 58 (1991) 2018
- 61 Kumakura K, Motohisa J and Fukui T, *J. Cryst. Growth* 170 (1997) 700
- 62 Lebens A, Tsai C S, Vahala K J and Kuech T F, *Appl. Phys. Lett.* 56 (1990) 2642
- 63 Fukui T, Nakajima F, Kumakura K, Motohisa J, *Bull. Mater. Sci.*



- 22(3) (1999) 531
- 64 Kirk P G and Polman A, *J. Appl. Phys.* 88 (2000) 1992
- 65 Matsuara D, Kanemitsu Y, Kushida T, White C W, Budai J D, Meldrum A, *Appl Phys. Lett.* 77 (2000) 2289
- 66 Meldrum A, White C W, Boatner L A, Anderson L M, Zuhr R A, Sonder E, Budai J D, Henderson D O, *Nucl. Instr. and Meth. B* 148 (1999) 957
- 67 Bonafos C, Garrido B, Lopez M, Romano-Rodriguez A, Gozalez-Varona O, Perez-Rodriguez A and Morante J R, *Appl. Phys. Lett.* 72 (1998) 3488
- 68 Meldrum A, Zuhr R A, Sonder E, Budai J D, white C W, Boatner L A, Ewing R C, Henderson D O, *Appl. Phys. Lett.* 74 (1999) 697
- 69 Takeda Y, Gritsyna V T, Umeda N, Lee C G and Kishimoto N, *Nucl. Instr. and Meth. B* 148 (1999) 1029
- 70 Liu Z, Li H, Feng X, Ren S, Wang H, Liu Z and Lu B, *J. Appl. Phys.* 84 (1998) 1913
- 71 Gangopadhyaya P, Kesavamoorthy R, Nair K G M and Dhandapani R, *J. Appl. Phys.* 88 (2000) 4975
- 72 Bhattacharya R S and Rai A K, *J. Mat. Res.* 2 (2) (1996) 211
- 73 Milosavljevic M, Shao G, Bibic N, McKinty C N, Jeynes C, Homewood K P, *Nucl. Instru. and Meth. B* 188 (2002) 166
- 74 Das A K, Ghose S K, Dev B N, Kuri G and Yang T R, *Appl. Surf. Sci.* 165 (2000) 260
- 75 He G, Atwar H A, *Nucl. Instru. and Meth. B* 106 (1995) 126
- 76 Chakravarti S K and Vetter J, *Nucl. Instru. and Meth. B* 62 (1991) 109
- 77 Martin C R, *Science* 266 (1994) 1961
- 78 Chakravarti S K and Vetter J, *J. Microchem. and Microeng.* 3 (1993) 57

- 79 Herron N, Wang Y, Eddy M M, Stucky G D, Cox D, Moller K and Bein T, *J. Am. Chem. Soc.* 11 (1989) 350
- 80 Choi K M and Shea K J, *J. Phys. Chem.* 98 (1994) 3207
- 81 Mathieu H, Richard T, Allegre J, Lefebvre P, Arnaud G, Granier W, Boudes L, Marc J L, Pradel A and Ribes M, *J. Appl. Phys.* 77 (1995) 287
- 82 Steigerwald M L and Brus L E, *Acc. Chem. Res.* 23 (1990) 183
- 83 Pileni M P, Motte L and Petit C, *Chem. Mater.* 4 (1992) 338
- 84 Zhao X K, Barai S, Orlando R and Fendler, *J. Am. Chem. Soc.* 110 (1988) 1012
- 85 Mahler W, *Inorg. Chem.* 27 (1988) 435
- 86 Spanhel L, Hasse H, Weller H and Henglein A, *J. Am. Chem. Soc.* 109 (1987) 5649
- 87 Smotkin E S, Brown R M, Rahenberg L K, Salomon, Bard A J, Campion A, Fox M A, Mallouk T E, Webber E S and White J M, *J. Phys. Chem.* 94 (1990) 7453
- 88 Helsinki E, Lucas P and Wang Y, *J. Chem. Phys.* 89 (1988) 3435
- 89 Wang Y, Suna A, Mahler W and Kasowski R, *J. Chem. Phys.* 87 (1987) 7315
- 90 Mahler W, *Inorg. Chem.* 27 (1988) 435
- 91 Taylor A, *X-ray Metallography*, Wiley, New-York (1961)
- 92 Spanhel L and Anderson M A, *J. Am. Chem. Soc.* 113 (1991) 2826
- 93 Tan M, Cai W and Zhang L, *Appl. Phys. Lett.* 71 (25) (1997) 3697
- 94 Brus L E, *J. Chem. Phys.* 79 (1983) 5566
- 95 Efros Al L and Efros A L, *Sov. Phys. Semiconduct.* 16 (1982) 772

- 96 Schmitt-Rink S, Miller D A B and Chemla D S, *Phys. Rev. B* 35 (1987) 8113
- 97 Pal R, Bhattacharyya D, Maity A B, Chaudhuri S and Pal A K, *Nanostruct. Mater.* 4 (1994) 329
- 98 Borgohain K and Mahamuni S, *Semicond. Sci. Technol.* 13 (1998) 1154
- 99 Bube R H, *Photoelectron properties of semiconductors*, Cambridge University Press, Cambridge (1992)
- 100 Levy P W, *The encyclopedia of physics*, 2<sup>nd</sup> edition, VCH publishers Inc., New York (1991) p-1264
- 101 Randall J T and Wilkins M H F, *Proc. Roy. Soc. London* 184 (1945a) 366 and (1945b) 390
- 102 Garlick G F J and Gibson A F, *Proce. Roy. Soc., London* A 60 (1948) 574
- 103 Ranjan V and Singh V A, *Phys. Rev. B* 58 (1998) 2085
- 104 Sengupta A, Jiang B, Mandal K C and Zhang J Z, *J. Phys. Chem. B* 103 (1999) 3128
- 105 Zhang Z, *J. Acc. Chem. Res.* 30 (1997) 423
- 106 Zhang J Z, O' Neil R H and Roberti T W, *J. Phys. Chem.* 9 (1994) 3859
- 107 Mittleman D M, Schoenlein R W, Shiang J J, Colvin V L, *Phys. Rev. B: Cond. Matt.* 49 (1994) 14435
- 108 Sengupta A, Jiang B, Mandal K C and Zhang J Z, *J. Phys. Chem. B* 104 (2000) 9396
- 109 Henglein A, *Chem. Rev.* 89 (1989)1861
- 110 Huntley D J, Godfrey-Smith D L and Thewalt M L W, *Nature*

- 313 (1985) 105
- 111 Pradhan A S, Bhuwan Chandra and Bhatt R C, *Radiat. Prot. Dosim.* 5 (1983) 159
- 112 Allen P and McKeever S W S, *Radiat. Prot. Dosim.* 33 (1990) 19
- 113 Nanto H, Murayama K, Usada T, Taniguchi S and Takeuchi N, *Radiat. Prot. Dosim.* 47 (1993) 281
- 114 Chestnoy N, Harris T D, Hull R and Brus L E, *J. Phys. Chem.* 90 (1986) 3393
- 115 Chen W, Wang Z G, Lin Z J and Lin L Y, *J. Appl. Phys.* 82 (1997) 3111
- 116 Brus L, *IEEE, J. Quantum Electronics* QE-22 (1986) 1909
- 117 Ozin G A, *Adv. Mater.* 4 (1992) 612
- 118 Eychmuller A, Hasselbarth A, Katsikas L and Weller H, *Ber. Bunsenges, Phys. Chem.* 95 (1991) 79
- 119 Tomita M and Matsuoka M, *J. Opt. Soc. Am. B* 7 (1990) 1198
- 120 Wang Y and Herron N, *J. Phys. Chem.* 92 (1988) 4988
- 121 Klimov V I, *J. Phys. Chem.. B* 104 (2000) 6112
- 122 Rohatgi - Mukherjee K K, *Fundamentals of Photochemistry*, Wiley Eastern Ltd. New Delhi (1978)
- 123 Weller H and Eychmuller A, *Adv. Photochem.* 20 (1995) 165
- 124 Bhargava R N, Gallagher D, Hong X and Nurmikko A, *Phys. Rev. Lett.* 72 (3) (1994)
- 125 Woggon U, *Optical Properties of Semiconductor Quantum Dots*, Springer-Verlag, Berlin (1997)
- 126 Conwell E, *High field transport in semiconductors*, Academic press,

New-York (1967)

- 127 Huang K and Rhys, *Proc. Roy. Soc. London*, ser A 204 (1950) 406
- 128 Koch F, Petrova-Koch V and Muschik T, *J. Lumin.* 57 (1993) 273
- 129 Klein M C, Hache F, Ricard D and Flytzanis C, *Phys. Rev. B* 42 (1990) 11123
- 130 Nomura S and Kobayashi T, *Phys. Rev. B* 45 (1992a) 1305
- 131 Banyai L, Gilliot P, Hu Y Z and Koch S W, *Phys. Rev.* 45 (1992) 14136
- 132 Alivisatos A, Harris T, Carrol P, Steigerwald M and Brus L, *J. Chem. Phys.* 90 (1989) 3463
- 133 Siang J, Risbud S and Alivisatos A, *J. Chem. Phys.* 98 (1993) 8432
- 134 Champagnon B, Andrianasolo B and Duval E, *J. Chem.. Phys.* 94 (1991) 5237
- 135 Rajalakshmi M, Sakuntala T and Arora A K, *J. Phys: Condens. Matter* 9 (1997) 9745.
- 136 Rodden W S O, Torres C M S and Ironside C N, *Semicond. Sci. Technol.* 10 (1995) 807
- 137 Champagnon B, Andrianasolo B, Ramos A, Gandais M, Allais M and Benoit J-P, *J. Appl. Phys.* 73 (1993) 2775
- 138 Tamura A, Higeta K and Ichinokawa T, *J. Phys. C: Solid state Phys.* 15 (1982) 4975
- 139 Duval E, Boukenter A, Champagnon B, *Phys. Rev. Lett.* 56 (1986) 2052
- 140 Rousset J L, Boukenter A, Champagnon B, Dumas J, Duval E, Quinson J F and Serughetti J, *J. Phys.: Condens. Matter* 2 (1990) 8445
- 141 Rousset J L, Duval E and Boukenter A, *J. Che. Phys.* 92 (1990) 2150
- 142 Efros Al L, Ekimov A I, Kozlowski F, Petrova-Koch V, Schmibauer H

- and Chumilovs, *Solid state Commun.* 78 (1991) 853-856
- 143 Kittel C, Introduction to Solid state Physics, John-Wiley & Sons Inc., New York (1971)
- 144 Licari J J and Evard R, *Phys. Rev. B* 15 (1977) 2254
- 145 Mori N and Ando T, *Phys. Rev. B* 40 (1989) 6175
- 146 Nanda K K, Sahu S N, *Appl. Surf. Sci.* 119 (1997) 50-54
- 147 Kiang C H, Goddard W A, Beyers R and Bethune D S, *J. Phys. Chem.* 100 (1996) 3749
- 148 Ajayan P M, Ravikumar V and Charlier J C, *Phys. Rev. Lett.* 81 (1998) 1437
- 149 Toulemonde M, Dufour C and Paumier E, *Phys. Rev. B* 46 (1992) 14362
- 150 Wang Z G, Dufour C, Paumier E and Toulemonde M, *J. Phys.: Cond. Mat.* 6 (1994) 6733
- 151 Lesueur D and Dunlop A, *Radiat. Eff. Def. Solids* 126 (1993) 163
- 152 Fleischer R L, Price P B and Walker R M, (eds.) *Nuclear Tracks in Solids*, University of California Press, Berkely, CA (1975)
- 153 Mehta G K and Patro A P, *Nucl. Instru. and Meth. A* 268 (1988) 334.
- 154 Kanjilal D, Chopra S, Narayanan M M, Iyer I S, Jha V, Joshi R and Datta S K, *Nucl. Instru. and Meth. A* 238 (1993) 97.
- 155 Zeigler J F, *The stopping range of ions in matter*, SRIM-97 (NY:IBM Research) p.1-28
- 156 Koch U, Fojtikn A, Weller H and Henglein A, *Chem. Phys. Lett.* 122 (1985) 507

- 157 Bahnmann D W, Kormann C and Hoffmann M R, *J. Phys. Chem*  
91 (1987) 3789
- 158 Kamat P V and Patrick B, *J. Phys. Chem.* 96 (1992) 6829
- 159 Hasse M, Weller H and Henglein A, *J. Phys. Chem.* 92 (1988)  
482
- 160 Hoyer P, Eichberger R and Weller H, *Ber. Bunsenges, Phys.*  
*Chem.* 97 (1993) 630
- 161 Berthelot A, Hemon S, Gourbilleau F, Dufour E, Paumier E,  
*Nucl. Instru. and Meth. B* 146 (1998) 437
- 162 Grinberg M, Legowski S and Meczynska H, *Phys. Status Solidi B* 130  
(1985) 325.
- 163 Brus L E, *J. Chem. Phys.* 80 (1984) 4403
- 164 Wang L W and Zunger A, *J. Phys. Chem B* 102 (1998) 6449
- 165 Gleiter H, *Prog. Mat. Sci.* 33 (1989) 223
- 166 Norris D J and Bawendi M G, *Phys. Review B* 53 (1996) 16338
- 167 Heimer, *Nature* 408 (2000) 531
- 168 Biro L P, Szabo B, Mark G I, Gyulai J, Havancsak K, Kurti J,  
Dunlop A, Frey L, Ryssel H, *Nucl. Instru. and Meth. B* 148 (1999)  
1102
- 169 Singh J P, Singh R, Mishra N C, Ganesan V and Kanjilal D, *Nucl.*  
*Instru. and Meth. B* 179 (2001) 37
- 170 Salata O V, Dobson P J, Hull P J, Hutchison J L, *Thin Solid*  
*Films* 251 (1994) 1-3

- 171 Johnson R E and Brown W L, *Nucl. Instr. and Meth. B* 198 (1982) 103
- 172 Toulmonde M, Costantini J M, Dufour Ch., Metftah A, Paumier E, Studer F, *Nucl. Instr. and Meth. B* 116 (1996) 37
- 173 Hemon S, Chailley V, Dooryhee E, Dufour Ch, Gourbilleau F, Levesque F and Paumier E, *Nucl. Instr. and Meth. B* 122 (1997) 563
- 174 Dufour Ch., Hemon S, Gourbilleau F, Paumier E and Dooryhee E, *Materials Science Forum* 248-249 (1997) 21
- 175 Hemon S, Dufour Ch, Gourbilleau F, Paumier E, Dooryhe E and Begin-Collin S, *Nucl. Instr. and Meth. B* 146 (1998) 443
- 176 Mohanta D, Nath S S, Bordoloi A, Dolui S K, Mishra N C and Choudhury A, *J. of Appl Phys*, 92 (12) (2002) 7149-7152
- 177 Neugebauer C A in: (ed.) Maissel L I and Glang R, *Hand book of Thin Film Technology*, Mc Graw Hill Inc. New York (1970)
- 178 Heinig K H, Schmidt B, Strobel M and Brnas H, *Mat. Res. Soc. Proc.* 650 (2001) R9.6.1 and 647 (2001) O14.6
- 179 Stampfli P, *Nucl. Instru. and Meth. B* 107 (1996) 138
- 180 Akkermann A, Levinson J, Ilberg D and Lifzhitz Y and R Baragiola (eds.), *Ionization of solids by Heavy particles*, NATO Advanced Study Institutes Series 306, Plenum, New York (1992) p- 431
- 181 Schiwietz G, Luderer E, Xiao G and Grande P L, *Nucl. Instr. and Meth. B* 175 (2001) 1-11
- 182 Schoos D, Mews A, Eychmuller A and Weller H, *Phys. Rev. B* 49 (1999) 17072



- 183 Bhargava R N, Gallagher D and Welker T, *Proce. Of Int. Conf. on Luminescence*, Storrs, CT (1994)
- 184 Balandin A, Wang K L, Kouklin N and Bandyopadhyay S, *Appl. Phys. Lett.* 76(2) ( 2000) 137
- 185 Dinsmore A D, Hsu D S, Qadri S B, Cross J O, Kennedy T A, Gray H F and Ratna B R *J. Appl. Phys.* 88(9) (2000 ) 4985
- 186 Qadri S B, Skelton E F, Dinsmore A D, Hu J Z, Kim W J, Nelson C and Ratna B R, *J. Appl. Phys.* 89(1) (2001) 115
- 187 Dyer John R, *Applications of absorption spectroscopy of organic compounds*, NJ:Prentice-Hall Inc. (1994)
- 188 Virk H S, Chandi P S and Srivastava A K, *Bull. Mat. Sci* 24 (5) (2001) 529
- 189 Virk H S, Chandi P S and Srivastava A K, *Radiat. Effects & Defects in Solids* (2001) (In Press)
- 190 Ogawa S, *Japan. J. Phys.* 16 (1960) 1488
- 191 Rao B S and Murthy M R, *J. Polymer science part B: Polymer Physics* 25 (1987)1897
- 192 Abraham R J and Whiffen D H, *Trans. Faraday Soc.* 54 (1958) 1291
- 193 Mohanta D, Nath S S, Mishra N C, Choudhury A, *Bull. Mat. Sci.* 26 (4) (2003) (In press)
- 194 Brus L E , *Nanostruc. Mater* 1 (1992 ) 71
- 195 Gumlich H E , *J. Lumin.* 23 (1981) 73
- 196 Busse W, Gumlich H E, Meissner B and Theis D, *J. Lumin.* 12 (1976)

693

- 197 Benisty H, Sotomayor-Torres C and Weisbuch C, *Phys. Rev. B* 44 (1991) 10945
- 198 Tomanek D and Schluter M, *Phys. Rev. Lett.* 56 (1986) 1055
- 199 Schmitt-Rink S, Chemla D S and Miller D A B, *Phys. Rev. B* 32 (1985) 6601
- 200 Soldatov E S, Khanin V V, Trifonov A S, Gubin S P, Kolesov V V, Presnov D E, Iakovenko S A, Khomutov G B, Korotkov A N, *Physics-Uspekhi* 41(2) (1997) 202
- 201 Andres R P, Bein T, Dorogi M, Feng S, Henderson J I, Kubiak C P, Mahoney W, Osifchin R G and Reifenberger R, *Science* 272 (1996) 323
- 202 Andres R P, Datta S, Dorogi M, Gomez J, Henderson J I, Jones D B, Kolagunta V R, Kubiak C P, Mahoney W and Osifchin R G, *J. Vac. Sci. Technol. A* 14 (1996) 1178
- 203 Schmolke R, Scholl E, Nagelle M and Gutowski J, *J. Cryst. Growth* 138 (1994) 213
- 204 Erel S and Uluer I, *Indian J. Phys.* 75A (3) 263-265
- 205 Danhauser T, O'Neil M, Johansson K, Whitten D and McLendon G, *J. Phys. Chem.* 90 (1986) 6074
- 206 Neil M, Marhon J and McLendon G, *J. Phys. Chem.* 94 (1990) 4356
- 207 Bawendi M G, Carroll P J, Wilson W L and Brus L E, *J. Chem. Phys.* 96 (1992) 946
- 208 Nirmal M, Murray C B, Norris D J and Bawendi M G, *Z. Phys. D* 26

- (1993) 361
- 209 Hoheisel W, Colvin V L, Johnson C S and Alivisatos A P, *J. Chem. Phys.* 101 (1994) 8455
- 210 Weller H and Eychmuller A, *Adv. Photochem.* 20 (1995) 165
- 211 Duntan D E, Hagfeldt, Almgren M, Siegbahn H O G, and Mukhtar E, *J. Phys. Chem.* 94 (1990) 6797-6804
- 212 Neuhauser R G, Shimizu K T, Woo W K, Empedocles S A and Bawendi M G, *Phys. Rev. Lett.* 85 (2000) 3301-3304
- 213 Empedocles S A and Bawendi M G, *Science* 278 (1997) 2114-2117
- 214 Boyd R W, *Nonlinear Optics*, Academic Press, New-York (1982)
- 215 Gibbs H M, *Optical bistability, Controlling light with light*, Academic Press New York (1985)
- 216 Prasad P N and Williams D J, *Introduction to Nonlinear effects in Molecules and Polymers*, Wiley, New York
- 217 Sauter E G, *Nonlinear Optics*, John Wiley, New York (1996)
- 218 Wilson J, Hawkes J F B, *Optoelectronics: An introduction*, Prentice Hall International Ltd., UK, (1992)
- 219 Lap-Tak Cheng, N Herron and Wang Y, *J. Appl. Phys.* 66 (1989) 3417
- 220 Cotter D, Burt M G and Manning R J, *Phys. Rev. Lett.* 68 (1992) 1200
- 221 Astill A G, *Thin Solid Films*, 204 (1991) 1
- 222 Woggon U, *Optical Properties of semiconductor quantum dots*, Springer-Verlag, Berlin, Heidelberg (1997)
- 223 Olbright G R and Peyghambarian N, *Appl. Phys. Lett.* 48 (1986) 1186

- 224 Sheik-Bahae M, Said A A, Wei T, Hagan D J and Van Stryland E W,  
*IEEE J. Quantum Electron* 26 (1990) 760
- 225 Sheik-Bahae M, Wang J, Desalvo R, Hagan D J, and Van Stryland E  
W, *Opt. Lett.* 17 (1992) 258
- 226 Sheik-Bahae M, Wang J, and Van Stryland E W, *IEEE J. Quantum  
Electron* 30 (1994) 249
- 227 Stegeman G I, Seaton C T, Chilwell J and Smith S D, *Appl. Phys. Lett.*  
44 (1984) 9
- 228 Vaynberg B, Matusovsky M, Petrikov V and Lipovskii A, *Opt. Commun.*  
132 (1996) 307
- 229 Jain R K and Lind R C, *J. Opt. Soc. Am.* 73 (1983) 647
- 230 Beecroft L L and Ober C K, *Chem Mater.* 9 (1997) 1302
- 231 Vijayalakshmi S and Gebel H, *Nonlinear optical properties of  
nanostructures* in (ed.) Nalwa H S, *Hand book of Nanostructured  
Materials and Nanotechnology*, Vol 4 (2000)
- 232 Sharma K K, Mainuddin, *J. Optics*, (1999) p-12
- 233 Kao K C and Hockham G A, *Dielectric surface waveguides for optical  
freq., Proce. IEE* 133 (July,1966) 1151-1158
- 234 Li T, *Advances in Optical Fiber Commun.-an historic perspective, IEEE  
J. on Selected Areas in Commun.* SAC-1(3) (April 1983) 356-372
- 235 Keyser U F, Schumacher H W, Zeitler U, Hang R J and Eberl K,  
*Physica Status Solidi* (b)22493) 681(2001)
- 236 Sahu S N, Patel B, Behera S N and Nanda K K, *Indian. J. Phys.*

- 74A(2) (2000) 93-97
- 237 Shivagan D D, Shirage P M and Pawar S H, *Pramana*, 58(5&6) (2002) 1183
- 238 Maruska H P, Namavar F and Kalkhoran N H, *Appl. Phys. Lett.* 61 (1338) 1992
- 239 Ashoori R C, *Nature* 371 (1996) 413
- 240 Hummel R E and Wissmann P, *Hand book of Optical Properties* Vol. I and II, CRC press, New York (1997)
- 241 Meisel D, Kamat P V, *Semiconductor Nanoclusters, Studies in Surface Sciences and Catalysis* 103 (1997) 79
- 242 Grabet H and Devoret M H, *Single Charge Tunneling: Coulomb Blockade Phenomna in Nanostructures*, Plenum Press, London (1992).
- 243 Averin D V and Likharev K K, *Quantum effects in small disordered systems* (ed.) Altshuler B, Lee P, Webb R, Elsevier, Amsterdam (1991)
- 244 Klein D L, McEuen P L, Katari J E B, Rothand R Alivisatos P and *Appl. Phys. Lett.* 68 (1996) 2574
- 245 Vinodgopal K, Bedja I and Kamat P V, *Chem. Mater.* 8 (1996) 2180
- 246 Amlani I, Orlov A O, Snider G L, Lent C S and Bernstein G S, *Appl. Phys. Lett* 72 (17) (1998) 2179
- 247 Kasai S, Amemiya Y and Hasegawa H, *Tech. Dig.2000 IEEE IEDM* (2000) 585
- 248 Marrahchi A, *Photonic switching and interconnects*, Marcel Dekker, Inc. New York (1994)

# **PUBLICATIONS**

## PUBLICATIONS

1. Defect modified suppression of recombination emission in CdS quantum dots stimulated by thermal means, *Proceedings of the 2<sup>nd</sup> Regional conference on physics research, PANE, Cotton College, October 28, 2000; p-21.*
2. Production of semiconductor quantum dots on polymer matrix by chemical method and their size control, *Indian J. Physics*, **75A(1)** (2001) 53-56.
3. Optical absorption study of 100-MeV chlorine ion irradiated hydroxyl free ZnO semiconductor quantum dots, *J. Appl. Phys.*, **92** (12) (2002) 7149-7152
4. Ion irradiation response of semiconductor nanoparticles embedded in polymer matrix, *Annu. Report 2001-2002, Nuclear Science Centre, p-116.*
5. Size estimation and luminescence enhancement of II-VI semiconductor quantum dots, *Asian J. Physics*, **12(1)** (2003) 57-62
6. Irradiation induced grain growth and surface emission enhancement of ZnS:Mn/PVOH semiconductor nanoparticles by  $\text{Cl}^{+9}$  ion impact, *Bull. Mat. Sci.*, **26** (3) (2003) ( *In press*)
7. SHI induced grain growth and grain fragmentation effect of polymer embedded CdS quantum dot system, *J.Chem. Phys.* (Communicated)
8. Spectroscopic investigations of carrier confinement and surface phonon detection in polymer embedded CdS quantum dot systems, *Solid State Commun.* (Communicated)
9. Non-resonant non-degenerate frequency mixing response of embedded cadmium sulfide quantum dots, *Appl. Phys. Lett.* (communicated).

# **ADDENDA**



## Production of semiconductor quantum dots on polymer matrix by chemical method and their size control

D Mohanta<sup>†</sup>, S K Dolui\* and A Choudhury\*

Department of Physics\* and Department of Chemical Sciences\*

Tezpur University Assam-784 028 India

E-mail best@agnigarh tezuernet in

---

**Abstract** Zero dimensional (0D) non linear optical materials will have revolutionary implications in the future generation of optical information systems. As a source of 0D media quantum dots in the form of nanometer sized crystallites (nano crystals – Ncs) embedded in dielectric polymer matrices are found to be less expensive chemical routes over molecular beam epitaxy (MBE) methods. Of course semiconductor clusters of few nanometers in size have attracted special attention because of their unique size dependent properties which include optical and physico chemical properties. Of all semiconductors CdS has been used most frequently from a view point of the quantum size effect. In semiconductor quantum dots a continuous energy spectrum of electrons and holes inherent in a bulk crystal is reduced to a number of discrete levels. Accordingly a set of absorption bands arises with the position controlled by the dot size. A finite size distribution in real quantum dot ensembles as well as variations in potential barriers and defect concentrations in local environment result in homogeneous broadening of the optical absorption and emission spectra. In this realm the present paper focuses on the chemical route of production of CdS quantum dots on polymer matrix and consequent control of crystallite sizes. The quantum dots thus prepared are examined by X ray diffraction and optical spectra studies. The consequent linking of the experimental observations to a theoretical model is also attempted in this paper. Our investigations have shown that diffusion treatment of hydrogen sulphide is much more reliable over direct treatment in controlling the size of the nano crystallites.

**Keywords** Nano crystallites semiconductor quantum dot diffusion treatment

**PACS Nos** 81 20 Ka 85 30 Vw 85 30 Wx

---

### 1. Introduction

As a promising source of device application *e.g.* photonic switching, single electron transistor (SET) and other optical communication applications, optical studies of quantum dots have provided very interesting results. The physical effects are dominant in quasi zero-dimensional semiconductor nano-structures. High quality structures which are crowded with quantum dots for optical studies have become available by a number of different technologies. Apart from highly expensive and complex molecular beam epitaxy preparation technique, chemical routes also provide nano-crystallites as efficient as molecular beam epitaxy method. Semiconductor quantum dots in glass and polymer matrices have been the subject of many theoretical and experimental investigations [1-4]. Previously, several kind of thiols functional group like mercaptoethanol (HOCH<sub>2</sub>CH<sub>2</sub>SH), mercaptoethylamine (H<sub>3</sub>NCH<sub>2</sub>CH<sub>2</sub>SH) *etc*

were found to act as additive elements to control the size of CdS nano particles [5]. The present paper outlines a brief theory and our recent efforts to prepare CdS quantum dots in new polymer films in view of relevant chemical methods of producing highly concentrated quantum dots of controlled sizes. The corresponding optical absorption and energy shift were studied by UV and Raman spectra respectively.

### 2. Experimental

Aromatic solids like polyvinyl alcohol, being good solutes for water, were chosen as polymer matrices. In the aqueous (2%) solution of polyvinyl alcohol, cadmium chloride was added with varying concentrations (1,2,3 wt%) under a high stirring rate (200 rpm) condition. The constant temperature was maintained upto 70°C for 3 hours. The sample under preparation was kept whole night for complete dissolution to get a transparent solution. Again stirring condition was maintained at least upto 1 hour for the said temperature and kept undisturbed for slow

---

<sup>†</sup> Corresponding Author

cooling process. To this solution,  $H_2S$  gas was passed directly upto its maximum absorbance. The CdS films were cast over glass substrates and allowed to dry in a closed chamber at room temperature and thus kept ready for subsequent experimentation. For another set, the films were cast at first then kept in an enclosed vessel and allowed to stay in semi-dry condition followed by  $H_2S$  diffusion reaction. The samples were kept undisturbed for 2-3 days for completion of the chemical reactions. The CdS films were now ready for successive experimentation.

In another technique, a mixture of styrene, acrylic acid (95:5), benzoyl peroxide (0.5% on monomer weight) and methanol were taken in a stoppered conical flask. The contents are then flushed with dry nitrogen gas. Polymerization of the co-polymer was carried out at the chosen temperature ( $65^\circ C$ ). After the completion of the experiment the films were cast using the same co-polymer. The films were dried in a vacuum oven at  $40^\circ C$  followed by neutralisation with ammonia and washed repeatedly with distilled water and dried in the same environment. The polymer was treated with  $CdCl_2$  (1.5% approx.) solution overnight. It was further washed repeatedly with distilled water and dried. Finally, passivation and exposure to hydrogen sulphide gas yields nano-crystallites of CdS. All the parameters and conditions of preparation in the various steps have been optimized by trial and error.

### 3. Results and discussion

X-ray diffraction studies indicated that the CdS nanoparticles crystallized in the cubic  $\beta$ -phase in contrast to the bulk material (Figure 1). The average dimension of the crystallites as

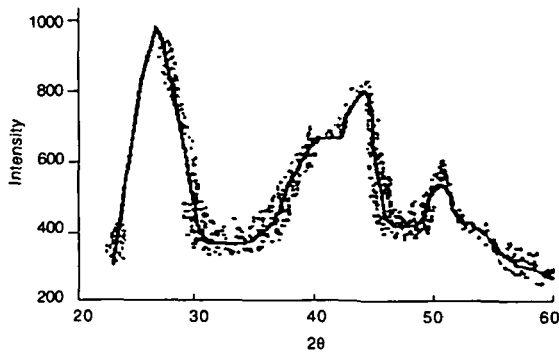


Figure 1. X-ray diffraction pattern of CdS in Polymer matrix

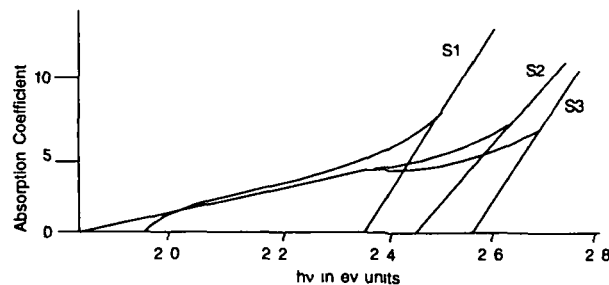


Figure 2. Absorption spectra of CdS in and near UV regime

determined by Scherrer formula ( $d = \lambda / W \cos \theta$ ,  $W$  being the full width at half maxima,  $\theta$  the Bragg angle) are 8 nm, 2 nm, 1.5 nm respectively. The optical absorption spectra taken in the visible and near UV range show a considerable shift of the onset of absorption from the band edge of bulk CdS (Figure 2). The absorption edges exhibit the characteristic blue shift. This is a clear evidence of the shifts in the energy levels of the electrons and holes caused by the strong confinement in the quantum dots.

One can interpret the cause of blue shift with the help of a simple model. The semiconductor particles of high refractive index were supposed to be assembled in a medium of comparatively low refractive index (polymer matrix) so that the particles remove light from the incident light beam both by scattering and absorption. However, absorption dominates over scattering. Moreover, when the radius of the bound electrons in these semiconductor crystallites approach the Bohr excitonic radius ( $\sim 5$  nm), their electronic and optical properties start changing. This is the so-called quantum size effect [6]. In general, when the energy of the incident light is larger than the band gap, the electrons can be excited into conduction band leaving behind holes in the valence band. The energy levels of the electron or hole can be obtained for a spherical quantum dot of radius  $r$ , with infinite barrier at the dot-polymer interface. These are given by

$$E_{nl}^h = -\frac{0.0382}{(m_h/m_0) R^2} \alpha_{nl}^2,$$

for the hole and

$$E_{nl}^e = \frac{0.0382}{(m_e/m_0) R^2} \alpha_{nl}^2 + E_g, \quad (1)$$

for the electron

The energy values as given above are expressed conveniently in units of eV with  $R$  in units of nm for quantum states characterized by the quantum numbers  $(n, l)$ ,  $n = 1, 2, 3, 4$  and  $l = 0, 1, 2, 3$  and  $\alpha_{nl}$  is the Spherical Bessel function of order unity,  $m_h$  and  $m_e$  are effective band masses of the hole and electron respectively,  $m_0$  is the free electron mass and  $E_g$  is the energy band gap of the semiconductor. Selection rules permit transitions satisfying  $\delta n = 0$  and  $\delta l = 0$ . The blue shift spectral behaviour according to this model follows the  $1/R^2$  behaviour. The absorption spectra here shows a blue shift with particle size ( $R$ ) decreasing (samples  $S_1, S_2, S_3$ ) and a large component of irregular broadening of the peaks found due to small cluster sizes (Figure 1).

Mie has formulated the theory of optical absorption for the small conducting spheres in the colloids [7]. In our case, we believe that the nano-crystallites as small conducting spheres positioned somewhere in the polymer matrix. The formulation could give a satisfactory description of the absorption behaviour.

in the UV and near visible range. The reciprocal absorption length  $\alpha$  satisfies the relation

$$\alpha hv = \text{const} (hv - E_g)^n, \quad (2)$$

where  $n$  assumes the value 0.5 for a direct transition and 2 for an indirect one. As a consequence, the threshold excitation requires a contribution of lattice phonons in order to compensate for the change in the wave vector during the transition [8]. This theory is valid for extinction spectrum in the absence of quantum size effects. For CdS, the reciprocal absorption length near the band edge showed exponential dependence on photon energy as  $\alpha = \exp(\beta hv / kT)$ ,  $\beta$  has a value 2.1 for single crystals [9]. Now one might think of independent scatterers as small and randomly oriented spheres, the mean separation of which is larger than the wave length of incident light and particle dimensions are much smaller than the incident light ( $R \ll \lambda$ ). We define the complex dielectric constant as

$$\varepsilon = (n_p + ik_p)^2 = n_p^2 - k_p^2 + i(2k_p n_p), \quad (3)$$

where  $n_p$  and  $k_p$  are the refractive index of the particle and the absorption index which is proportional to the reciprocal absorption length  $\alpha_p$  within the particle for light related with the wavelength,  $k_p = \alpha_p \lambda / 4\pi$ . The imaginary part of the dielectric constant is a direct measure of the light absorption by the particles. It increases steeply near the fundamental absorption edge.

The effects arising from the spatial confinement of charge carrier in semiconductors have also been the subject of intensive investigations [10, 11]. Earlier observations of confinement effects in these systems concerned small CdS particles in glass matrices [12, 13]. Quantum size effects are expected to occur when the Bohr radius of the first exciton in semiconductor becomes comparable with or larger than that of the particle. The Bohr radius  $r_B$  depends on the dielectric constant  $\varepsilon$  as per the relation

$$r_B = \hbar^2 \varepsilon_0 \varepsilon / (e^2 \pi m^{eff}) \quad (4)$$

Considering  $\varepsilon$  as its real part, the contribution from eq (3) in the case of CdS is found to be 8.9 and  $m^{eff} = m_e^-$  yielding for the

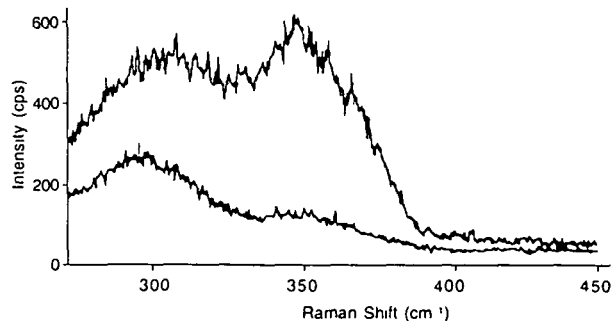


Figure 3 Raman spectra of CdS films prepared from 1:4 CdCl<sub>2</sub> and Polyvinyl alcohol for 1 and 3 wt% CdCl<sub>2</sub> solution for diffusion H<sub>2</sub>S

Bohr radius of the electron  $\sim 24 \text{ \AA}$ . Charge carrier confinements should become noticeable when CdS particle radius decreases below this value.

For the samples prepared by H<sub>2</sub>S diffusion, it is found that for the stoichiometric ratio 1:4 of CdCl<sub>2</sub> and polyvinyl alcohol, the maximum shift (peak) is 295 cm<sup>-1</sup> corresponding to normalised intensity  $\sim 300$  cps, whereas for 1:15 ratio, the maximum peak is observed at 349 cm<sup>-1</sup> for normalised beam intensity  $\sim 3200$  cps. It clearly shows that the particle dimension being smaller, unable to scatter light at the low energy regime (Figures 3 and 4).

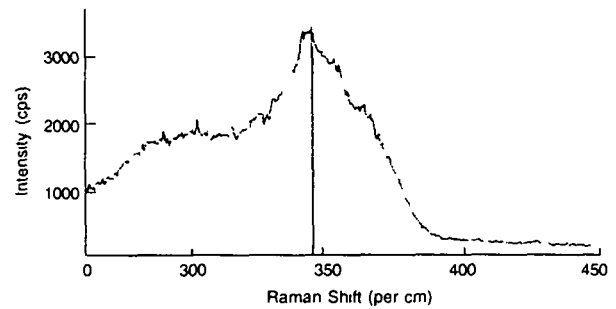


Figure 4 Raman spectra of CdS film prepared from 1:15 CdCl<sub>2</sub> and polyvinyl alcohol 1 wt% solution of CdCl<sub>2</sub> for diffusion H<sub>2</sub>S

Again, there is a considerable shift of peak from 295 to 348 found for minor change in CdCl<sub>2</sub> concentration, claiming optimum value for controlled crystallites. However, for the samples prepared by direct H<sub>2</sub>S treatment, there is no significant variation of peak which confirms that the diffusion treatment may have wide scope of controlling the dimension of the quantum dots assembled in the polymer host matrix compared to those prepared by direct treatment as assessed from Figure 5.

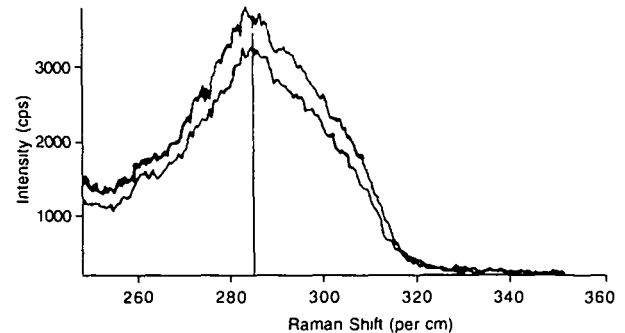


Figure 5 Raman spectra of CdS samples prepared from 1:4 CdCl<sub>2</sub> and Polyvinyl alcohol for 1 and 3 wt% CdCl<sub>2</sub> solution in direct H<sub>2</sub>S treatment

#### Acknowledgment

The authors express their sincere thanks to the Head, USIC Gauhati University for providing XRD facility. The authors would like to extend hearty gratitude to the Head, NEHU-RSIC, Shillong for effective help in taking Raman Spectra. Also, the authors are thankful to their colleagues for valuable help and support at various steps to complete the work.

## References

- [1] A I Ekimov and A A Onuschenko *Soviet Phys Semicond* **16** 775 (1982)
- [2] S V Nair, L M Ramananaiah and K C Rustagi *Phys Rev* **B45** 5969 (1992)
- [3] P Nandakumar, C Vijayan, Y V G S Murti, K Dhanalaxmi and Sundararajan *Bull Mater Sci* **20** 579 (1997)
- [4] P Nandakumar, A R Dhobale, Y Babu, M D Sastry, C Vijayan, K Dhanalaxmi, G Sundararajan and Y V G S Murti *Solid State Commun* **106** 193 (1998)
- [5] Y Nosaka, K Yamaguchi, H Miyama and H Hayashi *Chemical Lett* **605** (1988)
- [6] Y Wang and N Herron *Phys Rev* **B42** 7253 (1990)
- [7] M Born and E Wolf *Principles of Optics* 6th edn (New York: Pergamon) (1980)
- [8] M Gratzel, F L Baton Rouge *Heterogeneous Photochemical Electron Transfer* (Finland: CRC Press) (1988)
- [9] D Dutton *Phys Rev* **112** 785 (1985)
- [10] L L Chang, L Esaki, W E Howard, R Ludeke *J Vac Sci Tech* **10** 11 (1973)
- [11] D S Chemla, D A B Miller *J Opt Soc Am B Opt Phys* **2** 1155 (1985)
- [12] G V Taeckel *Z Tech Phys* **7** 301 (1926)
- [13] J K Inamu, A M Mraz and W A Weyl *Solid Luminescent Materials* (New York: Wiley) p 182 (1948)

## Optical absorption study of 100-MeV chlorine ion-irradiated hydroxyl-free ZnO semiconductor quantum dots

D Mohanta,<sup>a)</sup> S S Nath, A Bordoloi, and A. Choudhury  
*Department of Physics Tezpur University, P.O. Napaam, Assam-784 028, India*

S K Dolui  
*Department of Chemical Sciences, Tezpur University, P.O. Napaam, Assam-784 028, India*

N C Mishra  
*Nuclear Science Centre Aruna Asaf Ali Road, P.O. Box 10502, New Delhi 110 067 India*

(Received 30 April 2002, accepted 12 September 2002)

We report here synthesis and optical absorption study of energetic ion-irradiated hydroxyl-free ZnO semiconductor quantum dots. Quantum dot samples were synthesized by a quenching technique and 100-MeV chlorine ion was selected for the irradiation experiment with doses  $1 \times 10^{11}$ ,  $5 \times 10^{11}$ ,  $5 \times 10^{12}$ , and  $10^{13}$  ions/cm<sup>2</sup>. With an increase in fluence, the optical absorption spectra of irradiated quantum dots reveal redshift of the energy-gap parameter with respect to unirradiated (virgin) quantum dots. The narrowing of the energy gap of nanoparticles indicate particle growth under ion irradiation which is confirmed from transmission electron microscope images. The possible reason for such variations was encountered using an effective-mass approximation model which fits well for small effective mass and high-dielectric constant ( $\epsilon_0$ ). © 2002 American Institute of Physics [DOI: 10.1063/1.1518751]

During recent years, fabrication of quantum, sized crystallites (quantum dots) by various methods has been an emerging area of research for various optical, electronic, magnetic, and spectroscopic applications. Synthesis of CdE, ZnE ( $E=S, Se, Te, \text{etc}$ ) quantum dots by expensive molecular-beam epitaxy techniques as well as by simple chemical routes have been found in literature.<sup>1-6</sup> Previously, fabrication details of electronic oxide semiconductor nanoparticle systems (e.g., ZnO, etc.) in the presence of reaction byproducts, unreacted species and dispersing media were discussed elsewhere.<sup>6-12</sup> To prepare semiconducting quantum particles, chemical routes are attractive because of manifold interests like easy method of preparation, use of cost-effective chemicals, and large-scale productions, etc. So, quantum dots synthesized by chemical methods receive more and more attention to study either charge transportation process<sup>13</sup> or ion bombardment effect upon them. Recently, swift heavy ion irradiation-induced grain splitting and even disappearance of nanometric grains of SnO<sub>2</sub> powder was reported by Berthelot *et al.*<sup>14</sup> Their observation of the fragmentation of larger grains into smaller ones in particular has been explained by thermal spike-induced internal pressure inside the grains.

In the present article, we report the synthesis of ZnO quantum particles by using a quenching method. Then, they were irradiated by 100-MeV <sup>35</sup>Cl ions at four different fluences  $1 \times 10^{11}$ ,  $5 \times 10^{11}$ ,  $5 \times 10^{12}$ , and  $1 \times 10^{13}$ . The irradiated samples were analyzed by ultraviolet-visible optical absorption spectra and high-resolution transmission electron micrographs. The respective energy shifts with fluence variations, computed using effective-mass approximation (EMA)

model after testing its validity, revealed redshift of the energy-gap parameter of the irradiated samples with respect to the unirradiated quantum dots. The narrowing of the energy gap of the nanoparticles of ZnO indicates particle growth under ion irradiation. This is contrary to the irradiation-induced fragmentation of nanoparticles observed earlier.<sup>14</sup>

Polyvinyl alcohol (PVOH) was chosen as the matrix for embedding quantum particles. 5-gm-mole ZnO powder (99.99% pure, Merck) was sintered upto  $\sim 900$  °C for at least 5 h and then quenched into 10 wt% aqueous PVOH matrix kept at ice-cold temperature followed by moderate magnetic stirring ( $\sim 200$  rpm). The ZnO quantum dot samples were developed on the laboratory glass slides by placing a few drops of an as-prepared sample on a clean slide and stretching over it by another clean slide to cast very fine films. The samples of size  $1 \times 1$  cm<sup>2</sup> were made for the ion irradiation experiment. To compare with irradiated samples, one of the samples was reserved as unirradiated (virgin) specimen. The irradiation experiment was carried out on four identical samples. The quantum dot samples were mounted on a vacuum shielded vertical sliding ladder having four rectangular faces. They were irradiated in the Material Sciences chamber under high vacuum ( $4.6 \times 10^{-6}$  Torr) by using the 100-MeV <sup>35</sup>Cl ion beam with an approximate beam current of 1.0 pA (particle nanoampere), available from the 15UD tandem pelletron accelerator at NSC, New Delhi, India.<sup>15,16</sup> The ion-beam fluence was measured by integrating the ion charge on the sample ladder, which was insulated from the chamber. The fluence was varied in the range  $10^{11}$ – $10^{13}$  ions/cm<sup>2</sup>. In order to expose the whole target area, the beam was scanned in the x-y plane over the sample. The projectile range of the incident ion, as estimated by the

<sup>a)</sup>Electronic mail: best@tezu.ernet.in

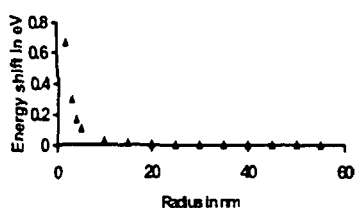


FIG 1  $\Delta E$  vs  $R$  plot for ZnO nanoparticle system

SRIM program<sup>17</sup> was found to be more than the thickness of the sample film (10.5  $\mu\text{m}$  as determined by the microbalance method). The ion-beam energy and the thickness of the target was so chosen that only the modification due to electronic energy loss ( $S_e$ ) affects the exposed sample. The ion-beam-induced effect was analyzed in terms of absorption spectra obtained by using UV-visible spectrophotometer in the range 200–800 nm. The machine was operated at a low-photon count rate to obtain all natural peaks.

ZnO is a direct band-gap semiconductor with bulk band-gap 3.35 eV at 300 K. So, bulk ZnO has got an absorption threshold corresponding to  $\lambda = 371$  nm. It is well known that when the electron has a small effective mass and the material dielectric constant is large, the mean distance of the electron from the trapping center (ionized donor or hole) is large. In other words, orbital frequency of the  $e-h$  pair about their center of mass will be slower than (or, approximately equal to) the frequency of the lattice vibrations. Then, the appropriate value to be considered is static dielectric constant, i.e.,  $\epsilon_0$ . In our representative ZnO nanomaterial system, if it would be accountable to the EMA model, then experimental redshifts with ion fluences must satisfy well even for the determination of average quantum dot size. The EMA with static dielectric constant is used to calculate a scaled binding energy

$$E_b = E_{RY} m^* / \epsilon_0^2 m_e \quad (1)$$

where  $E_{RY}$  is the Rydberg energy (13.6 eV) in the hydrogen atom model. Now for ZnO,  $m^* = 0.27m_e$  and  $\epsilon_0 = 8.5$  and so,  $E_b \sim 51$  meV  $< 100$  meV. Therefore, the combination of a small effective mass and large dielectric constant makes the EMA a relevant subject of consideration for the static dielectric constant.<sup>18</sup> A simple expression for the change in the band-gap energy when an uncorrelated  $e-h$  pair being generated is given by<sup>19</sup>

$$\Delta E = (\hbar^2 \pi^2 / 2R^2) (m_e^{*-1} + m_h^{*-1}) - 1.8 (e^2 / \epsilon R) + \text{pol} \quad (2)$$

where  $R$  is the average radius of the quantum particles,  $m^*$  being the respective effective masses for electron and hole,  $\epsilon$  is the dielectric constant, and pol represents polarization terms. This approach generally predicts an increase in the band-gap energy with decreasing particle size. The Plot of  $\Delta E$  versus  $R$  in case of ZnO is shown in Fig 1. The average size of irradiated quantum dots was estimated using the same plot (Table 1).

Earlier, band-gap widening in CdO<sup>19</sup> and in other semiconductor oxide nanoparticle systems have been reported elsewhere. Again, it has been studied that thermally stimu-

TABLE I Energy shift and size effect due to ion fluence variations

| Irradiation fluence (ions/cm <sup>2</sup> ) | Absorption edge (nm) | Band gap energy | $\Delta E$ shift | $R$ (nm) |
|---------------------------------------------|----------------------|-----------------|------------------|----------|
| Bulk                                        | 371                  | 3.350           | 0                |          |
| 0                                           | 260                  | 4.770           | 1.420            | 1.3      |
| $1 \times 10^{11}$                          | 285                  | 4.361           | 1.011            | 1.8      |
| $5 \times 10^{11}$                          | 315                  | 3.945           | 0.595            | 2.3      |
| $5 \times 10^{12}$                          | 335                  | 3.710           | 0.360            | 4.0      |
| $1 \times 10^{13}$                          | 370                  | 3.359           | 0.009            | 50.0     |

lated luminescence of ZnO and related semiconductor quantum dots<sup>20,21</sup> show flat response due to the suppression of recombination emission possibly due to large density surface states ( $s/v > 1$ ). Luminescence in the group of electronic oxide solids such as ZnO, MgO, SiO<sub>2</sub>, and Al<sub>2</sub>O<sub>3</sub> have already been reported<sup>22,23</sup> and the result suggests that the point defect impurity complexes are primarily responsible for light emission. Specifically, oxygen and oxygen-related vacancies are thought to play a significant role in the luminescence properties. Synthesis of ZnO by the quenching method was adopted to obtain hydroxyl-free quantum particles and chlorine ion was selected for irradiation which accounts for double interests. First the bleaching action upon the unwanted species, if any, attached to the ZnO quantum dots to obtain extra-pure ZnO quantum particles. And so, one may go for off-line characterizations to deal with information obtained only from extra-pure ZnO nanoparticles. Secondly, as our ZnO nanoparticles are embedded in the PVOH polymer matrices and polymer easily gets amorphized through evolution of ion tracks even at low-ion energies henceforth a light ion like oxygen/chlorine is preferable to notice appreciable irradiation-induced effects upon the embedded nanoparticles.

The projectile range of 100 MeV <sup>35</sup>Cl ion beam upon ZnO embedded into PVOH film was estimated to be around 18.6  $\mu\text{m}$  (using SRIM code) which is more than 1.5 times the thickness of the sample, i.e., 10.5  $\mu\text{m}$ . The grain-boundary problem is a severe problem found in almost all continuous nanocrystalline films. In our samples, where quantum particles are embedded, one should expect grain characteristics only which may help in better understanding of various models of ion-matter interactions (e.g., ion spike model,<sup>24</sup> thermal spike model<sup>25,26</sup>). The energy lost by the ions in a solid is mainly dominated by two mechanisms known as electronic and nuclear stopping. The electronic energy loss is dominant for ions possessing high energy (of million electron volt range) and involves the energy transfer to atoms in the target due to inelastic ion-electron interaction. The electronic stopping power of the beam  $S_e$  is 553 eV/A<sup>0</sup>. The irradiation leads to energy deposition at four different doses without implantation of chlorine ions into the samples.

UV-visible spectroscopy, which provides useful information regarding optical band gap is being treated as an important tool for material investigations. The optical absorption spectra of virgin and irradiated ZnO quantum dot samples are shown in Fig 2. For the unirradiated sample, free exciton absorption at around  $\sim 260$  nm was noticed. The excitonic peak becomes pronounced and sharper up to threshold dose, i.e.,  $5 \times 10^{12}$  ions/cm<sup>2</sup>. In the spectrum of the second dose,

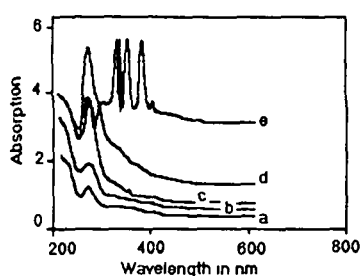


FIG 2 Optical absorption spectra of (a) virgin and irradiated samples with fluences (b)  $10^{11}$  (c)  $5 \times 10^{11}$  (d)  $5 \times 10^{12}$  and (e)  $10^{13}$  ions/cm<sup>2</sup>

the nearby band was seen around the main peak which is possibly due to second exciton creation corresponding to the same  $n=1$  level. While for the third dose, in addition to  $n=1$ ,  $n=2$  excitonic absorption was noticed which was not noticeable in the case of the virgin sample. Again, the band edge was found to be shifted strongly towards red, illustrating the fact that ion bombardment leads to modification of quantum particle behavior. The possible cause may be due to C-C bond breakage of the polymer. Fast ion beam melts the quantum particles and rapid quenching leads to aggregation into bigger clusters within a time of about  $10^{-12}$  sec. But, it is reasonable to say after a close look at the absorption plot that the nature of particle aggregation depends upon ion fluence, energy, and target type as we had observed long tailing with increasing fluences. Obviously, long tailing was due to large inhomogeneity of nanocrystallites with respect to the virgin sample. Therefore, nanoparticles have not actually been damaged but they were modified in size and in structure under ion irradiation as revealed from (HRTEM) depicted in Fig 3. Beyond a threshold dose, polymer was supposed to be amorphized completely. The quantum particles thus lose their support in the polymeric matrix and they coalesce into bigger clusters. At the highest fluence, the larger-sized quantum dots ( $\sim 50$  nm calculated by using EMA) behave as free-standing particles. We thus observe growth of the nanoparticles under energetic ion irradiation, whereas Berthelot

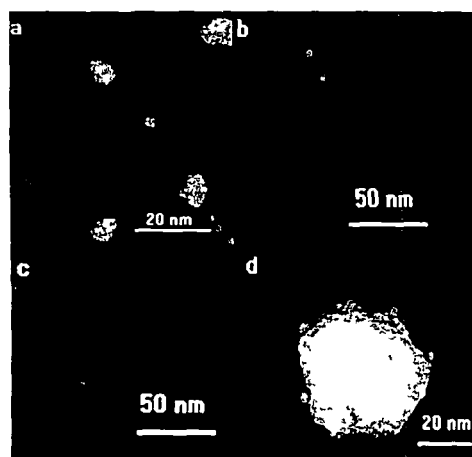


FIG 3 HRTEM of (a) virgin and irradiated ZnO quantum dots with fluences (b)  $5 \times 10^{11}$  (c)  $5 \times 10^{12}$  and (d)  $10^{13}$  ions/cm<sup>2</sup>

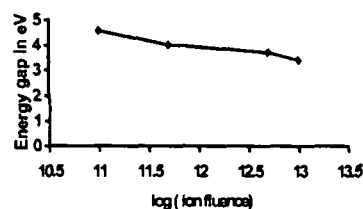


FIG 4 Energy shift  $\Delta E$  vs log of ion fluences

*et al*<sup>14</sup> have seen particle fragmentation. Though both the effects are produced due to the electronic energy loss of the SHI in the medium, the details of the microstructure and actual energy deposited by the ion differ in both cases. Another interesting feature observed in the spectrum of the highest dose selected so far, was an unexpected signature of free carrier excitonic absorption corresponding to  $n \geq 2$  levels. The other in between subsidiary peaks that arise may be due to the excitons bound to the neutral donors. If the excitons collide with impurities such as donors or acceptors, they are bound to them, and afterwards are annihilated exhibiting luminescence. The logarithmic response of the energy gap with ion fluence is depicted in Fig 4. The negative slope representing suppression of the energy-gap parameter of ion exposed samples with respect to unirradiated one.

Although EMA is still in a controversial place to describe energy shift as a function of size for various semiconductors, with justification we have fitted it for measuring ZnO quantum dot size after the ion irradiation study. The optical absorption study shows redshift of the onset with respect to virgin. Again, the evolution of free exciton absorption to higher levels ( $n \geq 2$ ) are suggested for the ion dose beyond critical value. The highest dose shows pure ZnO behavior of which the size is estimated to be 50 nm, consistent with transmission electron micrographs.

The authors thank ISRO, Bangalore for sponsoring quantum dot project under respond. The authors are thankful to the NSC for providing chlorine beam against Project BTR No 30109/2001. The authors extend sincere thanks to Dr A. Sarma for providing UV-visible spectrophotometer and Head, RSIC, Shillong for providing HRTEM.

<sup>1</sup> R. Passler, E. Gnebl, G. Lautner, S. Bauer, H. Preis, W. Gebhardt, B. Buda, D. Schikora, K. Lischka, K. Papagelis, S. Ves, *J Appl Phys* **86**(8) 4403 (1999).

<sup>2</sup> C. B. Murray, D. J. Norris, and M. G. Bawendi, *J Am Chem Soc* **115** 8706 (1993).

<sup>3</sup> J. Nanda, D. D. Sarma, *J Appl Phys* **90**(5) 2504 (2001).

<sup>4</sup> J. D. Budai, C. W. White, S. P. Withrow, R. A. Zuhr, and J. G. Zhu, *Mater Res Soc Symp Proc* **452** 89 (1997).

<sup>5</sup> C. W. White, J. D. Budai, A. Meldrum, S. P. Withrow, R. A. Zuhr, E. Sonder, A. Puretzky, D. B. Geohegan, J. G. Zhu, and D. O. Henderson, *Mater Res Soc Symp Proc* **504** (In Press).

<sup>6</sup> C. Bonafos, B. Garrido, M. Lopez, A. Romano, Rodriguez, O. Gonzales, V. Anan, A. Perez, Rodriguez, and J. R. Morante, *Appl Phys Lett* **72** 3488 (1998).

<sup>7</sup> U. Koch, A. Fojtik, H. Weller, and A. Henglein, *Chem Phys Lett* **122** 507 (1985).

<sup>8</sup> D. W. Bahnemann, C. Kormann, and M. R. Hoffmann, *J Phys Chem* **91** 3789 (1987).

<sup>9</sup> P. V. Kamat and B. Patrick, *J Phys Chem* **96** 6829 (1992).

- <sup>10</sup>L. Spanhel, H Weller, and A Henglein, *J Am Chem Soc* **109**, 6632 (1987)
- <sup>11</sup>M. Hasse, H Weller, and A Henglein, *J Phys Chem* **92**, 482 (1988)
- <sup>12</sup>P. Hoyer, R Eichberger, and H Weller, *Ber Bunsenges Phys Chem* **97**, 630 (1993)
- <sup>13</sup>D. Meisel, *Semicond Nanoclust Stud Surf Sci Cataly* **103**, 79 (1996)
- <sup>14</sup>A. Berthelot, S Hemon, F Gourbilleau, E Dufour, and E Paumier, *Nucl Instrum Methods Phys Res B* **146**, 437 (1998)
- <sup>15</sup>G. K. Mehta, A. P. Patro, *Nucl Instrum Methods Phys Res A* **268**, 334 (1988)
- <sup>16</sup>D. Kanjilal, S. Chopra, M. M. Narayanan, I. S. Iyer, V. Jha, R. Joshi, and S. K. Datta, *Nucl Instrum Methods Phys Res A* **238**, 97 (1993)
- <sup>17</sup>J. F. Ziegler, SRIM-97, *The Stopping Range of Ions in Matter* (IBM Research, NY 1997), p 1
- <sup>18</sup>M. Grinberg, S. Legowski, H. Meczynska, *Phys Status Solidi B* **130**, 325 (1985)
- <sup>19</sup>L. E. Brus, *J Chem Phys* **80**, 4403 (1984)
- <sup>20</sup>N. Ueda, H. Maeda, H. Hosono, and H. Kawazoe, *J Appl Phys* **84**(11) 6174 (1984)
- <sup>21</sup>D. Mohanta, S. S. Nath, A. Bordoloi, S. K. Dolui, and A. Choudhury, *Asian J Phys* **11**(1), (In press)
- <sup>22</sup>S. Datta, M. Boswarval, and D. Holt, *J Phys Colloq* **C6** 22 (1980)
- <sup>23</sup>K. Lohner, M. Hastenrath, L. J. Balk, and E. Kubalek, *Inst Phys Conf Ser* **60**, 179 (1981)
- <sup>24</sup>R. L. Fleischer, P. B. Price, and R. M. Walker, *J Appl Phys* **36** 3645 (1965)
- <sup>25</sup>M. Toulemonde, C. Dufour, and E. Paumier, *Phys Rev B* **46**, 14 362 (1992)
- <sup>26</sup>Z. G. Wang, C. Dufour, E. Paumier, and M. Toulemonde, *J Phys Condens Matter* **6**, 6733 (1994)



# Irradiation induced grain growth and surface emission enhancement of chemically tailored ZnS : Mn/PVOH nanoparticles by $\text{Cl}^{+9}$ ion impact

D MOHANTA\*, S S NATH, N C MISHRA<sup>†</sup> and A CHOUDHURY<sup>‡</sup>

Department of Physics, Tezpur University, P.O Napaam, Assam 784 028, India

<sup>†</sup>Department of Physics, Utkal University, Bhubaneswar 751 004, India

<sup>‡</sup>Department of Physics, University of Florence, Via Sansone 50019 Sesto, Firentino, FI, Italy

MS received 8 October 2002; revised 24 April 2003

**Abstract.** Manganese doped zinc sulfide nanoparticles are fabricated on polyvinyl alcohol dielectric matrix. They are bombarded with energetic chlorine ions (100 MeV). The size of the crystallites is found to increase with ion fluence due to melting led grain growth under ion irradiation. The increased size as a result of grain growth has been observed both in the optical absorption spectra in terms of redshift and in electron microscopic images. The photoluminescence (PL) study was carried out by band to band excitation ( $\lambda_{\text{ex}} = 220 \text{ nm}$ ) upon ZnS : Mn, which results into two emission peaks corresponding to surface states and  $\text{Mn}^{+2}$  emission, respectively. The ion fluence for irradiation experiment so chosen were  $1 \times 10^{11}$ ,  $5 \times 10^{11}$ ,  $5 \times 10^{12}$  and  $10^{13} \text{ Cl/cm}^2$ .

**Keywords.** Quantum dot; irradiation; redshift.

## 1. Introduction

Semiconductors with dimensions in the nanometer realm are important because their electrical, optical and chemical properties can be tuned with particle size. During recent years, fabrication of nanosized crystallites in the form of capping (Mahamuni *et al* 1993), coating and embedding in glass (Borelli *et al* 1987; Yan and Parker 1989; Tanaka *et al* 1992) as well as in polymer matrix (Wang *et al* 1987, 1990; Henglein 1988; Deki *et al* 1999) by various methods have been reported. Interest in properties of sulfide nanocrystals stems from their potential use in nonlinear optical devices (Norris and Bawendi 1996). A large number of reports relating to structural, spectroscopic and luminescence properties (Bhargava and Gallagher 1994; Bhargava *et al* 1994; Wang and Zunger 1998; Schoos *et al* 1999; Nanda *et al* 1999; Balandin *et al* 2000; Dinsmore *et al* 2000; Qadri *et al* 2001) are available for both Mn-doped and undoped metal sulfide nanoparticle systems. Synthesis of ZnS, CdS etc. by ion implantation have been reported by various workers (Budai *et al* 1997; Bonafos *et al* 1998; Meldrum *et al* 1999). On the other hand, understanding ion–matter interaction is an important issue in materials science because of nature of electronic and nuclear energy losses. Accordingly, two models viz. ion spike model and thermal spike model are in balance. Grain evaporation and grain fragmentation have been observed in nanometric powder systems (Berthelot *et al* 1998), whereas radiation resistant

behaviour was noticed in case of Sr-ferrite nanoparticle system (Shinde *et al* 1998). In this context, ion impact on embedded nanoparticle system is interesting due to suppression of weak link boundaries which is inherent in case of nanostructured films. Recently, we have investigated optical absorption study of ion irradiated ZnO quantum dots (Mohanta *et al* 2002) and matrix dependent grain growth and grain fragmentation effects in CdS systems (Mohanta *et al*, to be published).

After growing Mn doped zinc sulfide nanoparticles in a aliphatic polymer viz. polyvinyl alcohol, we have irradiated them with 100 MeV chlorine beam at doses  $1 \times 10^{11}$ ,  $5 \times 10^{11}$ ,  $5 \times 10^{12}$  and  $10^{13} \text{ Cl/cm}^2$ . The intention of Mn doping was to correlate luminescence response with ion fluence. Optical absorption spectra of pristine and exposed samples were analysed in consistency with high resolution scanning and transmission micrographs. Photoluminescence was carried out to reveal surface emissions and size dependent emission spectra.

## 2. Experimental

The polymers being useful materials for the protection of nanosized particles against agglomeration and precipitation (Hirari and Toshima 1986), we have selected an aliphatic polymer to embed ZnS nanoparticles. First, an aqueous solution of 0.15 M  $\text{ZnCl}_2$  and 0.0045 M  $\text{MnCl}_2$  was made such that the molar ratio of Mn to Zn was 3 : 100. The aqueous solution was mixed into as prepared 2.5 wt.% transparent polyvinyl alcohol (PVOH) matrix under  $\sim 200 \text{ rpm}$  stirring condition. Temperature was

\*Author for correspondence

**Table 1.** Stopping energies and projectile range of energetic chlorine beam through ZnS : Mn/PVOH.

| Energy (MeV) | Electronic energy loss, $S_e = (dE/dx)_e$ (eV/Å) | Nuclear energy loss $S_n = (dE/dx)_n$ (eV/Å) | Projectile range, $R$ (μm) |
|--------------|--------------------------------------------------|----------------------------------------------|----------------------------|
| $10^{-2}$    | 11.19                                            | 63.32                                        | $1.02 \times 10^{-2}$      |
| $10^{-1}$    | 33.02                                            | 58.21                                        | $7.82 \times 10^{-2}$      |
| 1            | 249.0                                            | 20.08                                        | $7.63 \times 10^{-1}$      |
| 10           | 502.5                                            | 3.92                                         | 3.30                       |
| 100          | 553.0                                            | 0.58                                         | 18.07                      |

maintained to 65°C. Into this, dropwise injection of Na<sub>2</sub>S solution led to growth of ZnS quantum particles in PVOH matrix. Also, the ZnS nanoparticles are synthesized by grinding as received ZnS powder (99% pure, Lab Chem) mechanically, followed by sintering (~900°C) and finally quenching into ice-cold PVOH matrix. Colourless or faint milky coloured Mn doped ZnS samples were developed on the laboratory glass slides. The samples of size 1 × 1 cm<sup>2</sup> were made for irradiation experiment.

For each sample type, one sample was reserved as virgin to compare with irradiated sample. The irradiation was carried out on four identical samples. The nanoparticle samples were mounted on a vacuum shielded vertical sliding ladder having four rectangular faces. They were irradiated in the Mat. Sc. chamber under high vacuum ( $6.0 \times 10^{-6}$  Torr) by using the 100 MeV Cl<sup>+9</sup> beam with approximate beam current of 1.0 pA (particle nano-ampere), available from the 15UD tandem Pelletron Accelerator at NSC, New Delhi (Mehta and Patro 1988; Kanjilal *et al* 1993). The ion beam fluence was measured by integrating the ion charge on the sample ladder, which was insulated from the chamber. The fluence was varied in the range  $10^{11}$ – $10^{13}$  ions/cm<sup>2</sup>. In order to expose whole target area the beam was scanned over the x–y plane. The energy of the beam was chosen in such a way that the projectile range of the incident ion (as computed by SRIM program, Zeigler *et al* 1997) exceeds thickness of the sample films. Again, the ion beam energy and thickness of the target were selected so that modification due to electronic energy loss ( $S_e$ ) affects the exposed sample. The nature of the ion beam induced modification has been analysed by using UV-VIS spectrophotometer in the range 200–800 nm and electron microscopy images. The photoluminescence spectra beyond band gap excitation show evolution of intense surface emission with fluence variations.

### 3. Results and discussion

The characterizations of pristine and ion irradiated embedded zinc sulfide nanoparticle samples include high resolution scanning electron microscopy (HRSEM), high resolution transmission electron microscopy (HRTEM), optical absorption spectroscopy (OAS) and photolumi-

**Table 2.** Energy deposition with ion dose and nanoparticle grain growth.

| Irradiation dose (ions/cm <sup>2</sup> ) | Absorbed energy (Joules) | Absorption edge (nm) | Avg. grain size (nm) |
|------------------------------------------|--------------------------|----------------------|----------------------|
| 0                                        | 0                        | 310                  | 11                   |
| $1 \times 10^{11}$                       | 0.539                    | 314                  | 14                   |
| $5 \times 10^{11}$                       | 2.698                    | 320                  | –                    |
| $5 \times 10^{12}$                       | 26.976                   | 325                  | 32                   |
| $1 \times 10^{13}$                       | 53.952                   | 326                  | 41                   |

nescence (PL). The energy of the beam was so selected so as to travel through the samples without stop. In other-words, sample thickness (6.5 μm) was kept sufficiently lower than the projectile range i.e. 18.06 μm (table 1). As shown in the table for 100 MeV chlorine beam, electronic energy loss is predominant over nuclear energy loss and so we had to consider energy deposition due to the former cause. The electronic stopping power ( $S_e$ ) of the beam was 553 eV/Å. The irradiation doses deposited in embedded Mn : ZnS/PVOH samples at four different fluences are calculated to be 0.539, 2.698, 26.98, and 53.95 joules, respectively. The amount of heat deposition as a function of fluence results into melting followed by grain growth (table 2).

#### 3.1 Optical absorption studies

Optical absorption spectroscopy has become an important tool to observe size quantization effect in terms of blue shift and excitonic absorption (Brus 1992). As shown in figure 1, there is significant redshift of the onset of absorption of the ion irradiated ZnS : Mn nanoparticle samples. As the amount of energy shift is size dependent for a particular material and the size of the nanoclusters alters with fluence we believe there has been significant grain growth of nanoparticles under ion irradiation. It was known that the compounds with oxygen and nitrogen (containing non-bonding electrons) are capable of displaying characteristic absorption in the UV region (Virk *et al* 2001a,b) due to promotion of electrons in  $\sigma$ ,  $\pi$  orbitals (Dyer 1994). It was proposed that due to the presence of imide group (NC=O), absorption spectra possess transition peaks in UV regime. Although in aliphatic alcohols,

the hydrogen atom was reported to be removed by interaction of radiation yielding  $\alpha$ -hydroxy alkyl radical which has already been investigated (Abraham and Whiffen 1958; Ogawa 1960; Rao and Murthy 1987) polyvinyl alcohol is aliphatic and it has neither element like 'N' nor double bonds to facilitate carrier transition in the ultra-violet regime.

In addition to redshift of the onset of absorption, we see absorption band at around 300 nm, corresponding to exciton absorption of the particles, which has been studied extensively (Brus 1991; Yoffe 1993) in case of undoped ZnS systems. It has been reported in representative ZnS nanoparticle systems (Chen *et al* 1997) that surface states are mainly responsible for evolution of second broad band in the long wavelength ( $\sim 500$  nm) region. Moreover, they say that the second band disappears for capped in comparison to uncapped ZnS nanoparticles because of relatively less number of surface states in capped nanoparticles. We do not see any second absorption band in the virgin and low dose exposed samples. But interestingly, for the samples irradiated with high fluences a second band emerges at around  $\sim 400$  nm (figure 1). We believe appearance of such a band in the absorption spectra possibly due to the presence of surface states of ZnS : Mn nanoparticles which are now free from matrix encapsulation. Thus, even if ZnS : Mn nanoparticles have grown from an average size of 11 nm to 41 nm (table 2) due to ion impact, we observe recovery of the second band due to the surface states when the nanoparticles are free from matrix encapsulation.

### 3.2 Illustration of electron microscopic images

Although red shift in the absorption threshold in the absorption spectra is the first hand signature of signifi-

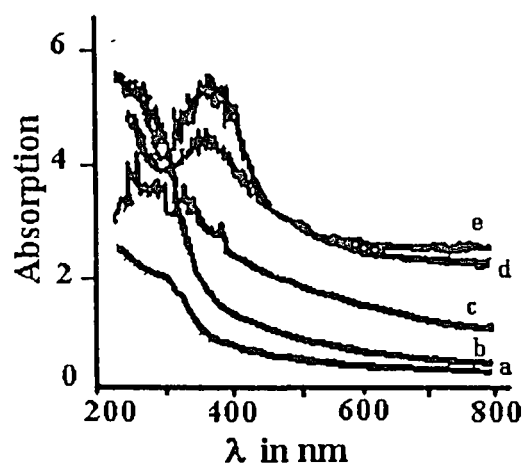


Figure 1. Optical absorption spectra of a. virgin and irradiated, b.  $1 \times 10^{11}$  ions/cm<sup>2</sup>, c.  $5 \times 10^{11}$  ions/cm<sup>2</sup>, d.  $5 \times 10^{12}$  ions/cm<sup>2</sup> and e.  $1 \times 10^{13}$  ions/cm<sup>2</sup> Mn : ZnS polymer embedded nanoparticles.

cant grain growth, high resolution electron microscopic images provide the best of informations relating to irradiation-led modification in nanoparticle systems. As depicted in figure 2, the electron micrographs show modified behaviour of ion irradiated nanograins with respect to virgin. Figure 2a represents high resolution SEM image of Mn : ZnS nanoparticles in the form of assembly embedded in PVOH whereas TEM image of individual nanograins of size about 11 nm is shown in figures 2b. Swift ion irradiation leads to deposition of huge amount of energy which causes rise in electronic temperature ( $\times 10^5$  °K) and afterwards ( $10^3$  s) cause lattice temperature rise ( $\times 10^3$  °K). The enormous rise in temperature (which exceeds melting point of ZnS i.e. 2100°K) within a time scale of  $10^{-12}$  s melts easily, all nearby particles along with the matrix represented in figures 2c. Rapid quenching gives rise to recrystallization as if grains have grown independently into definite sizes. The process of grain growth is a combined result of heat deposition and pressure effect. For the samples irradiated with highest dose ( $1 \times 10^{13}$  ions/cm<sup>2</sup>), we obtained well developed regular nanoclusters of average size 41 nm (figure 2d). The cluster of grains is displayed in a cross sectional view in figure 2c. They are supposed to be freestanding as already the polymer matrix has been damaged by complete amorphization. The complete amorphization was confirmed by no weight loss observation of the heavily exposed sample.

### 3.3 Photoluminescence (PL) studies

The PL study is important as it provides information relating to different energy states available between valence band and conduction band responsible for radiative recombination. It has been studied that the photoluminescent efficiency of coated ZnS : Mn nanocrystals is higher than the powder samples due to passivation of surfaces (Bhargava *et al* 1994). The ZnS nanoparticles have a weak PL emission relative to Mn doped system. The band to band excitation in ZnS has been used to excite the Mn<sup>+2</sup> emission. The subsequent transfer of electron and hole into the electronic level of the Mn ion leads to the characteristic emission of Mn<sup>+2</sup> in ZnS (Brus 1986). In consistency with these reports, we have noticed yellow-orange emission for ZnS : Mn nanoclusters with peak wavelength  $\sim 582$  nm. It is attributed to transitions involving d-electrons of the Mn<sup>+2</sup> ions (Busse *et al* 1976; Gumlich 1981). The Mn<sup>+2</sup> ion d-electron states act as efficient luminescent centres while interacting strongly with s-p electronic states of host ZnS nanocrystal into which external electronic excitation is normally directed. In an undoped quantum dot system, the external band edge as well as impurity related luminescent efficiency at room temperature is too low to be of any practical consequence (Benisty *et al* 1991). We also do not expect such emission for undoped ZnS system (figure 3a).

With increase in ion dose, there is no significant shift of the emission peaks arising out of  $Mn^{+2}$ . It is well known that when PL emission peak energies are less than the band gap energy of the material, these bands correspond to transitions involving donors, acceptors, free electrons and holes. The appearance of the PL peaks at energies substantially lower than the band gap suggests that transitions from energy states in the band gap are being favoured for the luminescence process in these nanocrystalline ZnS films (Pal 1999). As depicted in figure 3, the first emission peak position shifts towards blue with increase in ion dose. We recognize these peaks as a result of trapped luminescence, which were reported

in the form of broad bands in the PL spectra (Eychmuller 1991). Such peaks were attributed to the presence of surface states in nanocrystals. The surface emissions become more intensive with ion dose because the extent of free standing ZnS: Mn depends on degree of amorphization of the polymer matrix.

The shift of surface emission due to size variation has already been discussed (Chestnoy *et al* 1986). However, in case of second emission peak arising from  $Mn^{+2}$  site, particle size does not significantly affect the emission wavelength (Dinsmore *et al* 2000). As shown in table 3, in consistency with our observations, the shifting of surface emission peak towards blue is due to grain size

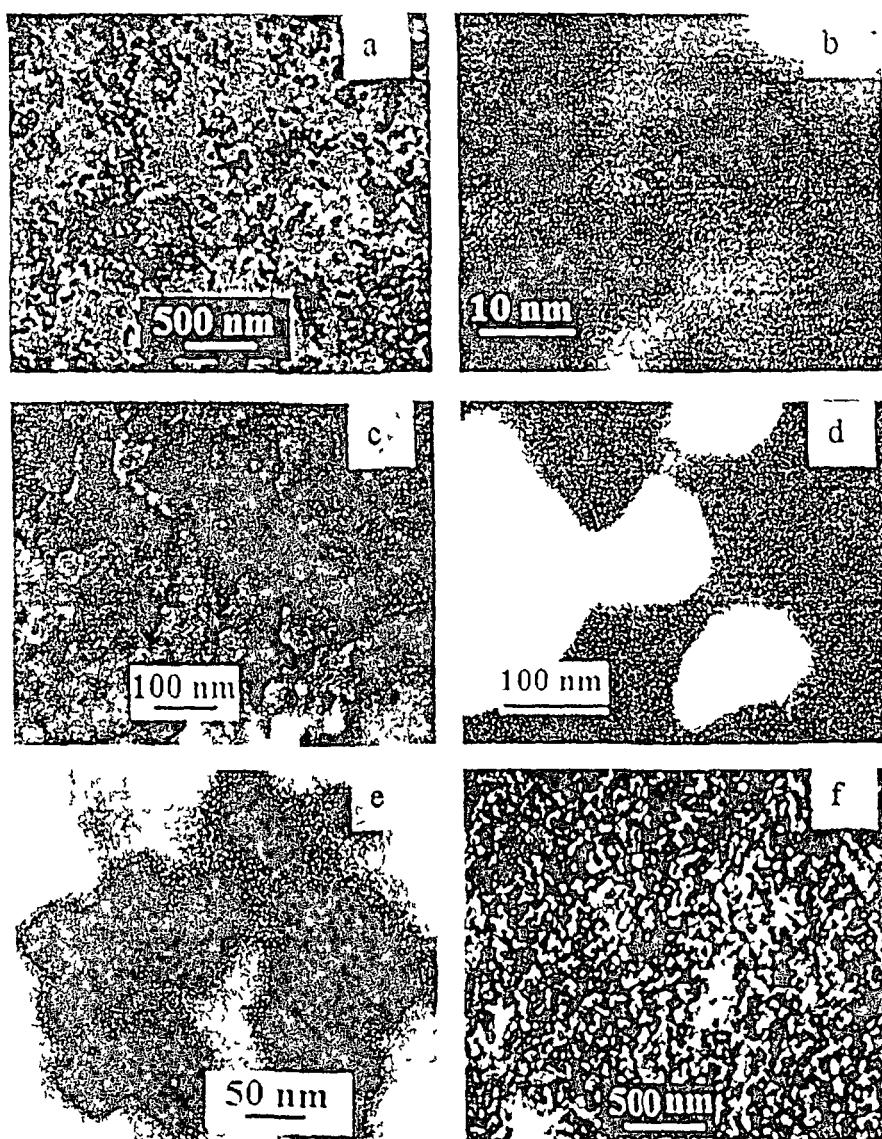


Figure 2. a. HRSEM and b. bright field TEM image of virgin, c. melting of the ion irradiated ( $5 \times 10^{11}$  ions/cm<sup>2</sup>), d. a cluster of individual grains grown as a result of irradiation ( $1 \times 10^{13}$  ions/cm<sup>2</sup>) and e. a cross sectional view of the heavily exposed polymer embedded  $Mn^{2+}$  ZnS nanoparticle sample

Table 3. Photoluminescence emission of virgin and irradiated Mn : ZnS nanoparticles.

| Samples         | Excitation wave-length ( $\lambda$ ) | $\lambda_1$ | Peak positions (nm) |             |        |
|-----------------|--------------------------------------|-------------|---------------------|-------------|--------|
|                 |                                      |             | Energy              | $\lambda_2$ | Energy |
| ZnS             | 220                                  | 480         | 2.576               | —           | —      |
| Mn : ZnS- $D_0$ | 220                                  | 405         | 3.179               | 580         | 2.131  |
| Mn : ZnS- $D_2$ | 220                                  | 382         | 3.236               | 582         | 2.124  |
| Mn : ZnS- $D_3$ | 220                                  | 375         | 3.296               | 582         | 2.124  |

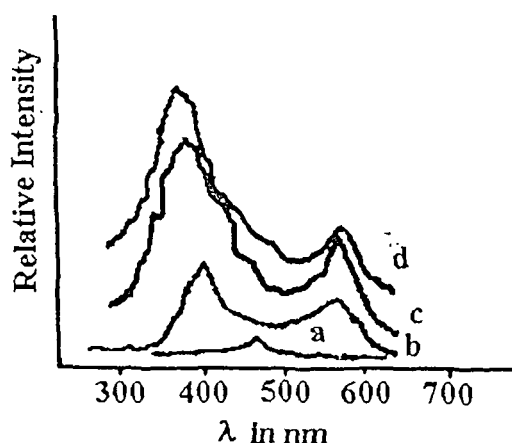


Figure 3. PL spectra of unirradiated a. polymer embedded undoped ZnS, and b. Mn doped ZnS, and ion irradiated c.  $5 \times 10^{11}$  ions/cm<sup>2</sup> and d.  $5 \times 10^{12}$  ions/cm<sup>2</sup> Mn doped ZnS nanoparticles.

effect studied for different substrate conditions (Pal *et al* 2000). The resulting intense emission may be suggested as net luminescence contributed by all the surface states, when the particles become fully free standing (for highest dose). Because for heavily dosed samples, the nanoparticles are supposed to be free from matrix encapsulation.

#### 4. Conclusion

In conclusion, we claim that embedded polymer system is advantageous to observe regular grain growth process under ion irradiation. The size of the grains can be tuned by selecting proper ion fluence. The samples irradiated with highest dose are free standing and that is why strong surface emissions are visible in PL spectra which arise from the surface states. The surface emission energy are calculated to be 3.179 eV, 3.236 eV and 3.296 eV for fluences 0,  $5 \times 10^{11}$  and  $5 \times 10^{12}$  ions/cm<sup>2</sup>, respectively. Moreover, the Mn<sup>2+</sup> emission peak of irradiated samples does not shift appreciably but intensity improves because heavily exposed nanoparticles overcome barrier encapsulation. However, surface emission shifts towards blue due to size effect. Therefore, sensitivity of the optical sensors supposed to be made of ion irradiated and doped semiconductors can be tuned by proper choice of ion dose.

#### Acknowledgements

The authors thank NSC, New Delhi, for providing chlorine beam. Also, they would like to thank USIC, JU; RSIC, NEHU; Physics Department HU for HRSEM, HRTEM and PL measurements, respectively.

#### References

- Abraham R J and Whiffen D H 1958 *Trans. Faraday Soc.* 54 1291
- Balandin A, Wang K L, Kouklin N and Bandyopadhyay 2000 *Appl. Phys. Lett.* 76 137
- Benisty H, Sotomayor-Torres C and Weisbuch C 1991 *Phys. Rev.* B44 10945
- Berthelot A, Hemon S, Gourbilleau F, Dufour E and Paumier E 1998 *Nucl. Instrum. & Meth.* B146 437
- Bhargava R N and Gallagher D 1994 *Phys. Rev. Lett.* 72 416
- Bhargava R N, Gallagher D and Welker T 1994 in *Proceedings of the international conference on luminescence* (Storrs: CT)
- Bonafos C, Garrido B, Lopez M, Romano-Rodriguez A, Gonzales-Varona, Perez-Rodriguez A and Morante J R 1998 *Appl. Phys. Lett.* 72 3488
- Borelli N F, Hall D W, Holland H J and Smith D W 1987 *J. Appl. Phys.* 61 5399
- Brus L E 1986 *IEEE J. Quantum Electron.* QE-22 1909
- Brus L E 1991 *Appl. Phys.* 53 45
- Brus L E 1992 *Nanostruct. Mater.* 1 71
- Budai J D, White C W, Withrow S P, Zuhr R A and Zhu J G 1997 *Mater. Res. Soc. Symp. Proc.* 452 89
- Busse W, Gumlich E, Meissner B and Theis D 1976 *J. Lumin.* 12 693
- Chen W, Wang Z G, Lin Z J and Lin L Y 1997 *J. Appl. Phys.* 82 3111
- Chestnoy N, Harris T D, Hull R and Brus L E 1986 *J. Phys. Chem.* 90 3393
- Deki S, Sayo K, Fujita T, Yamada A and Hayashi S 1999 *J. Mater. Chem.* 9 943
- Dinsmore A D, Hsu D S, Qadri S B, Cross J O, Kennedy T A, Gray H F and Ratna B R 2000 *J. Appl. Phys.* 88 4985
- Dyer J R 1994 *Applications of absorption spectroscopy of organic compounds* (NJ: Prentice-Hall Inc.)
- Eychmuller A, Hasselbarth A, Katsikas L, Weller H and Ges B 1991 *J. Phys. Chem.* 95 79
- Gumlich H E 1981 *J. Lumin.* 23 73
- Henglein A 1988 *Topics in current chemistry* 143 113
- Hirari H and Toshima N 1986 in *Tailored metal catalysts* (ed.) Y Iwasawa (Dordrecht: Reidel)

- Kanjilal D, Chopra S, Narayanan M M, Iyer I S, Jha V, Joshi R and Datta S K 1993 *Nucl Instrum & Meth* A238 97
- Mehta G K and Patro A P 1988 *Nucl Instrum & Meth* A268 334
- Mahamuni S, Khosravi A A, Kundu Manisha, Kshirsagar A, Bedekar A, Avasare D B, Singh P and Kulkarni S K 1993 *J Appl Phys* 73 5237
- Meldrum A, White C W, Boatner L A, Anderson I M, Zuhr R A, Sonder E, Budai J D and Henderson D O 1999 *Nucl Instrum & Meth* B148 957
- Mohanta D, Nath S, Bordoloi A, Dolui S K, Choudhury A and Mishra N C 2002 *J Appl Phys* 92 7149
- Mohanta D, Nath S, Choudhury A and Mishra N C *J Chem Phys* (to be published)
- Nanda K, Sarangi S N, Sahu S N, Deb S K and Behera S N 1999 *Physica* B262 31
- Norris D J and Bawendi M G 1996 *Phys Rev* B53 16338
- Ogawa S 1960 *J Phys Jap* 16 1488
- Pal A K 1999 *Bull Mater Sci* 22 341
- Qadri S B, Skelton E F, Dinsmore A D, Hu J Z, Kim W J, Nelson C and Ratna B R 2001 *J Appl Phys* 89 115
- Rao B S and Murthy M R 1987 *J Polym Sci Part B Polym Phys* 25 1897
- Schoos D, Mews A, Eychmuller A and Weller H 1999 *Phys Rev* B49 17072
- Shinde S R, Bhagwat A, Patil S I, Ogale S B, Mehta G K, Data S K and Marst G 1998 *J Magn Magn Mater* 186 342
- Tanaka A, Onari S and Arai T 1992 *Phys Rev* B45 6587
- Virk H S, Chandı P S and Srivastava A K 2001a *Bull Mater Sci* 24 529
- Virk H S, Chandı P S and Srivastava A K 2001b *Radiat Effects & Defects in Solids* (in press)
- Wang L W, Zunger A 1998 *J Phys Chem* B102 6449
- Wang Y, Suna A, Mahler W and Kasowski R 1987 *J Chem Phys* 87 7315
- Wang Y, Suna A, Meltugh J, Hilmiski E F, Lucas P A and Johnson R D 1990 *J Chem Phys* 92 6927
- Yan F and Parker J M 1989 *J Non-Cryst Solids* 112 277
- Yoffe A D 1993 *Adv Phys* 42 173
- Zeigler J F, SRIM-97 *The stopping range of ions in matter* (NY IBM Research) pp 1-28